Measurement of the $^{236}\mathrm{U}(\mathrm{n},\gamma)$ cross section for the thorium fuel cycle at the CERN n_TOF facility

Mark James Vermeulen

Doctor of Philosophy

University of York

Physics

March 2015

Abstract

This manuscript details the successful measurement, and subsequent analysis, of the ^{236}U(n, γ) radiative capture kernels in the resolved resonance region, of importance to the thorium fuel cycle.

The experiment took advantage of the convenient features of the CERN n_TOF facility. Features such as a fully digital DAQ, high instantaneous neutron flux, and the powerful background rejection capabilities offered by the BaF_2 Total Absorption Calorimeter (TAC) detector, owing to its near 4π solid angle coverage and high segmentation. These features, coupled with a high purity (99.85%) ^{236}U sample, resulted in the successful measurement of the radiative kernels to within 10%.

Having successfully extracted the radiative kernels up to 1500 eV with the R-matrix code SAMMY, and accounted for all sources of uncertainty, is was possible to quantify the total uncertainty for the radiative kernels. In this manner, the uncertainties were found to range from 2.3%, for resonances with little scattering and pile-up, to 5.3% for resonances with more significant scattering and pile-up effects. Hence not only was the goal of achieving the requested accuracy of 10% achieved, but even reaching the desired 5%.

Given the limited data available for this reaction, it is of value to be able to contribute the results of the current work to the nuclear data community to bolster the information currently available for the ^{236}U neutron capture cross section. Comparison with the latest versions of three of the major libraries, our cross section is in overall agreement with JEFF-3.2, 6% larger than JENDL-4.0 and 20% larger than ENDF/B-VII.1. These are sizeable differences considering our accuracy of just 2-5%, suggesting that some revision of the libraries may be in order.

Contents

List of Figures

List of Tables

Acknowledgements

There have been a great many people who have made the last four and half years of my Ph.D. one of the most enjoyable and fulfilling parts of my life to date. Many of these I would like to take the time here to thank.

Thank you to my supervisor, Prof. David Jenkins, for accepting me as his Ph.D. student and sending me off all around the world at the drop of a hat. By far one of the best aspects of the last four and a half years has been all the different countries I have had the opportunity to visit and all the people I have met as a result.

A huge thank you goes to Dr. Carlos Guerrero, my supervisor from the University of Sevilla, for his constant support and guidance throughout this Ph.D. Despite seemingly being on hand to give help to everyone in the n_TOF collaboration, he has always been able to make time to solve any problems that arose, and offer advice on all aspects of my analysis. For this, I am extremely grateful.

I would also like to say thank you to Dr. Nicola Colonna who also offered much valuable guidance and support, especially with discussions about theory and the use of the SAMMY code.

York has been my home for the last eight and a half years, and has given me a great many fond memories. Many people have contributed to these memories, far too many to mention here. However, Chris Kelley, Adam Nichols and Ed Martin have made forgetting the stresses of studying physics via the medium of beer an art form, as did many others in the physics department and beyond. But these same people also offered a great deal of help and support during my time at York, and for this I am very grateful.

Being a part of the n_TOF collaboration resulted in meeting many wonderful people who made trips to CERN, n_TOF analysis meetings and summer schools an incredible amount of fun. In particular Kevin Fraval, Massimo Barbagallo (U6 or you suck!) and Toby Wright, who ensured there was never a dull moment.

During my time at n_TOF, Eric Berthoumieux and Frank Gunsing have also been of great help in helping answer my many questions, and locating resources I otherwise would have been unable to find, for which I am very thankful.

I was also lucky to share an office with Nara Singh Bondili, who always made himself available for chats about physics, and was able to explain concepts that I could not grasp so simply.

And of course a huge thank you to my wonderful mother and sisters who have put up over the years with my constant droning about the highs and lows of university life, and allowing me to live rent free whilst wrestling with my thesis!

Last but not least, a big thank you to Dora for her continuous support, and putting up with me whilst I was working long hours and travelling all over the place. But most importantly of all for finally letting me have a document that did not end up with her drawing a bloody cat on it...

...Damn it.

Declaration

I declare that the work presented in this thesis, except where otherwise stated, is based on my own research, and has not been submitted previously for a degree at this or any other university.

Chapter 1

Nuclear Energy: The Thorium Fuel Cycle

This manuscript details the measurement and subsequent analysis of the ^{236}U neutron capture cross section. The study of this reaction was driven by the global need for accurate nuclear data relevant to alternative nuclear fuel cycles, in this case the thorium fuel cycle.

In this first chapter, an overview will be given of the current status of the worlds demand for energy, and the role nuclear has to play in the world energy mix. This will lead on to a discussion of what nuclear power is, the fuel cycles that generate this power, and the radioactive waste that is produced. Attention will then turn to a discussion of the need for accurate nuclear data and the libraries where this information is stored, readily accessible to the scientific community. This chapter will then end by focussing on the present situation with regards to the ^{236}U neutron capture cross section, of importance to the the thorium fuel cycle.

1.1 The Need For Nuclear Energy

With the world's population ever increasing and more and more countries undergoing rapid economic and industrial growth, the demand for energy to drive this expansion is continually increasing.

The primary modes of energy generation are shown in Figure 1.1 for the whole of the world [1]. Fossil fuels still dominate the energy market with gas, oil and coal being responsible for approximately 65% of all electricity generating capacity, large scale hydro 16%, wind 3%, nuclear energy providing about 13%.

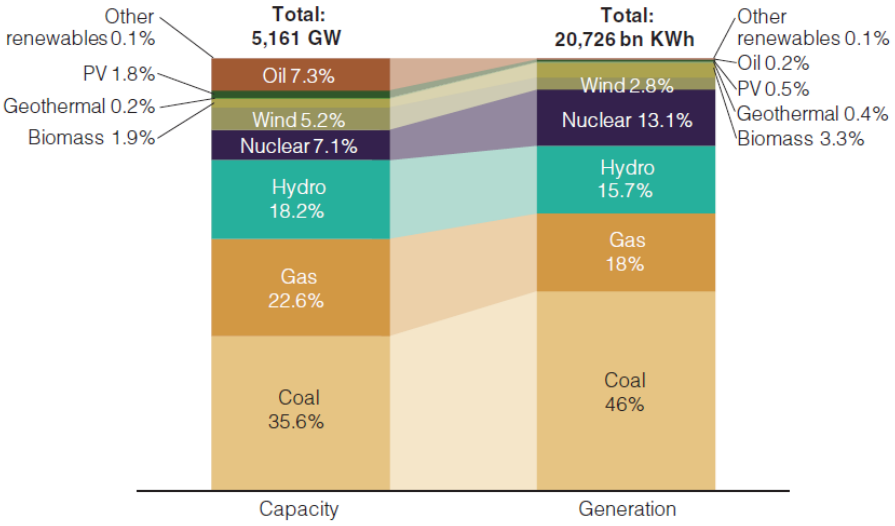

Figure 1.1: Plot showing the installed global electricity capacity versus the net energy generation for different energy sources. Used by permission of the World Energy Council, London, www.worldenergy.org.

Beginning with the industrial revolution in the 18th century, fossil fuels became the dominant energy source to drive industry. Over 250 years, the burning of these greenhouse gas (GHG) emitters has led to the irrefutable conclusion that mankind has had a detrimental impact on the environment in the form of global climate change [2]. With what is known today about the cause and effects of global climate change, the growing demand for energy from an increasing global population simply cannot be met by fossil fuels without irrevocably destroying the environment for future generations.

With the global average surface temperature of the Earth set to rise by 4°C by 2100 if large concentrations of GHG continue [2], the impact of rising sea levels, increased ocean acidity, species extinction, and an increased frequency of extreme weather, gives rise to the conclusion that prompt action to curb GHG emissions has to be taken now.

With the scientific consensus that global warming has been brought about by human activities [2], many developed nations are driving to reduce their carbon footprint by curtailing carbon emissions. This is realised in the Kyoto protocol whereby signatories who agreed to binding targets will aim to reduce GHG emissions by 20% by the year 2020. But this by no means constitutes an all encompassing solution. Many developed countries are unwilling to agree to cut carbon emissions, and many developing nations do not want to incur cost and restrictions for a situation which they did not bring about.

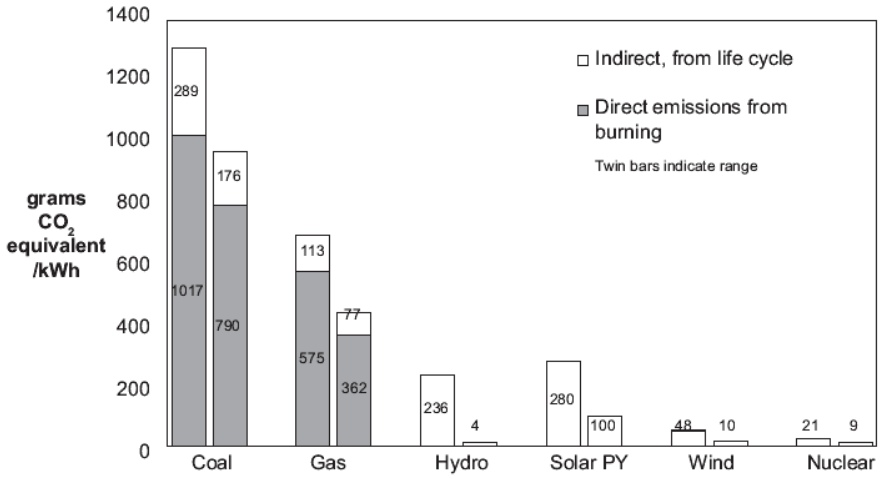

Figure 1.2: Carbon emissions from nuclear power and other forms of energy [3].

So how to reduce these emissions? An obvious answer is installing more capacity from renewables, and indeed there is a big push to do just this. Also the coal industry is proposing 'clean coal' whereby CO_2 is captured and stored underground, and the emissions of nitrous oxides, sulphur and heavy metals are reduced.

Figure 1.2 [3] shows another path to the reduction of carbon emissions. It can be seen that nuclear power has one of, if not the lowest, contributions to GHG emissions of all the alternatives. This coupled to the fact that nuclear energy is capable of providing the baseload power supply for a nation, and is able to respond to spikes in demand, make it a strong choice for energy security and the protection of the environment.

Trends show that due to clean energy initiatives driven by a need to reduce the world's carbon footprint in light of global warming, renewable energy sources are set to increase from approximately 23% to 34% by 2030. Fossil fuels themselves are expected to account for around 40-45% of all installed capacity by 2030, yet nuclear is anticipated to remain roughly the same at 6% [1].

Various bodies predict a continued short term reduction in new build and an acceleration of long term shut down in the wake of Fukushima. However, as the Earth's population continues to grow, so will the demand for electricity, and so will concerns for climate change and energy security. These factors all point to the need for nuclear to remain an important component of the energy mix in both the short and long term.

Indeed, the capacity of nuclear energy will continue to grow in absolute terms, particularly in Brazil, India, Korea and China, but the percentage contribution

to the world energy mix is predicted to decline through to 2030 and on to 2050. However, these predictions may well change once the Fukushima fear subsides and new regulations are in place.

Looking further into the future, although the estimated dates for peak oil, peak gas and peak coal get pushed back as better technology for extracting these energy sources are developed, estimates put all three of these fossil fuels to have reached peak by the 2050's [4]. Whether or not fusion becomes a commercial level energy provider remains to be seen, as there are many major technical difficulties to overcome. Renewables are not capable of providing a baseload power supply, nor of producing energy when there is no wind or sun. Due to an ageing electricity grid infrastructure in many countries, intermittent renewables can not be expected to provide more than about 20% of a countries power before instabilities become an issue.

Turning to nuclear energy, there are reportedly enough uranium reserves to last for around 200 years at todays consumption rate [5]. This is however a conservative estimate based on a once-through cycle. With a closed nuclear cycle, where spent fuel is reprocessed and used again, as is the case in Europe, this extends the ^{235}U fuel inventory. Sea water too contains substantial reserves of uranium and should sea water extraction become viable, resources would last for millennia. And with research into new, cleaner technologies, things improve even more.

Initiatives such as the Generation IV International Forum (GIF) and future technologies such as Accelerator Driven Systems (ADS) (see Section 1.2.1) seek to address the problems of waste reduction and waste elimination respectively. Further, an alternative fuel cycle based on the use of thorium provides ample supplies of fertile material from which to generate energy, and naturally results in the production of less long lived radioactive waste (LLRW) and addresses proliferation concerns. Given also that thorium is four times as abundant in the world as current uranium reserves, as shown in figure 1.3 [6], there are enough resources to power nuclear reactors until the Sun itself dies [7].

Electric vehicles (EV) and hybrids (HEV) are seen as a more environmentally friendly mode of transport. As more and more people turn to EVs and HEVs, so increases the demand for electricity. The problem here is that without the introduction of more environmentally friendly nuclear power, the widespread use of EVs and HEVs simply increases the demand for burning fossil fuels in power stations, in effect countering any environmental benefit driving an EV or HEV may have.

The hydrogen economy is widely seen as a future method of powering the econ-

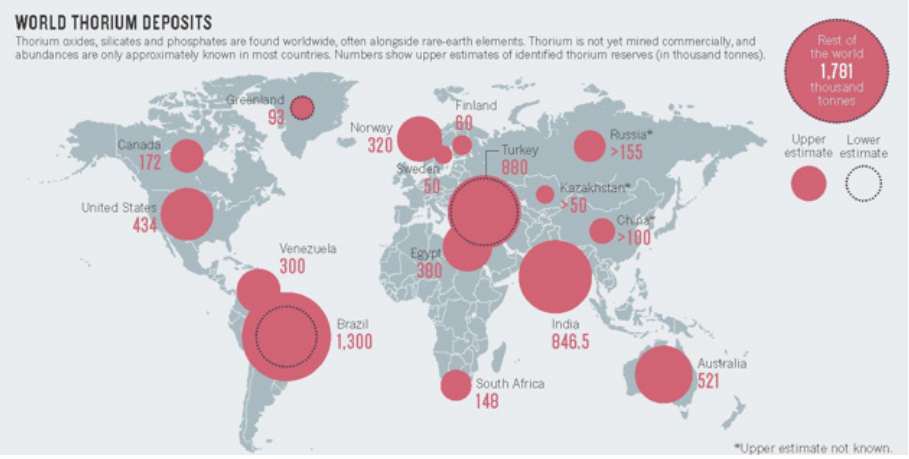

Figure 1.3: Thorium deposits world wide [6].

omy through the use of hydrogen as an energy source to power transport, homes and business. This hydrogen can be produced in future designs of high temperature nuclear reactors operating around 1000°C using thermochemical processes.

Given active research into the thorium cycle, and Generation IV and ADS, nuclear power is capable of supplying safe, clean, reliable and environmentally friendly energy, as well as the future option to create fuel for a hydrogen based economy.

Thus nuclear energy will continue to be an important part of the global energy mix now and in the future.

1.2 Energy From Thorium

There are many different designs of nuclear reactor in the world, some of which are in use today and many of which are currently being designed for the future. They operate at different neutron energies, use different fuel compositions and make use of different fuel cycles, all of which results in different quantities of nuclear waste. These topics will be looked at in the coming sections with a focus on where thorium fits into the picture in terms of the reactors which can utilise it, the difference between the conventional uranium and the proposed thorium fuel cycle, and the advantages of the latter. Finally the issue of nuclear waste will be looked at, where it will be seen that here, the thorium fuel cycle has the upper hand over its ubiquitous counterpart.

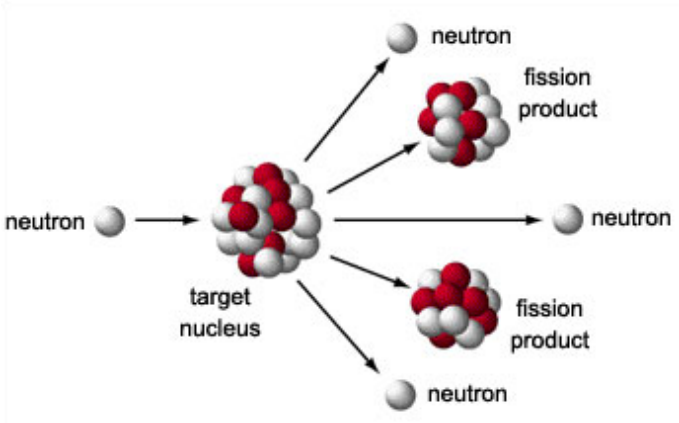

Figure 1.4: Graphic showing the neutron induced fission of a target nucleus resulting in the release of fission products and more neutrons [8].

1.2.1 Nuclear Power

Nuclear power refers to the nuclear processes that generate heat, and in turn electricity, in a nuclear power station or a nuclear submarine. These process are nuclear fission and nuclear decay.

Nuclear fission is where a high mass nuclei is split into smaller fission fragments accompanied by several neutrons. Fission can either occur spontaneously in high mass nuclei (e.g. ^{240}Cm, ^{242}Cf) or be induced by absorbing a neutron, and it is via this neutron induced fission that nuclear power stations generate electricity. A schematic of the induced fission process is shown in Figure 1.4 [8]. Following fission, the unstable fission fragments decay transforming into other isotopes by emitting ionising radiation and thus producing heat. All current nuclear reactors operating to produce energy for the electricity grid are based on uranium fuel, and it is the uranium isotope ^{235}U that fissions to produce energy.

Nuclear fusion is another nuclear process which involves two light nuclei being forced together to form a higher mass nucleus, releasing energy in the process. There are no fusion power plants in operation in the world today, only experimental reactors. ITER, being built in France, will be the world's largest experimental fusion reactor when its construction finishes in 2019 [9]. This is a stepping stone to building a demonstration commercial reactor called DEMO, before rolling out commercial fusion power worldwide. This can only occur if the technical challenges of fusion can be overcome, and commercial fusion power is unlikely to be available until 2040 at the earliest.

Civilian nuclear power traces its origins back to the discovery of the neutron in

1932 by James Chadwick. As the neutron lacks electric charge, its use as a means of nuclear experimentation was immediately apparent as it was capable of probing the nucleus and inducing radioactivity. Experiments with uranium led to the discovery in 1938 of induced fission, and the realisation that if a fissioning nucleus released more neutrons, a self sustaining chain reaction could occur. In 1942, under the supervision of Enrico Fermi, the worlds first ever man made chain reaction took place in the Chicago Pile-1 [8] as part of the Manhattan Project. Research during the 2^{nd} World War to make use of an uncontrolled chain reaction for use in nuclear weapons, culminating in the bombing of Hiroshima and Nagasaki in August 1945. In the aftermath, there was a push for the development of civilian nuclear power. The Obninsk reactor was the first nuclear power plant built in Russia, and was also the first to generate electricity in 1954, with the 5 MWe reactor being connected to the electricity grid. Shippingport Atomic Power Station in Pennsylvania, USA, achieved criticality 1957 and was the worlds first full scale nuclear power plant entirely for peacetime use. It began by using uranium fuel, but in 1977 generated 60 MWe by converting ^{232}Th to ^{233}U. From these early stages to the present day, where there are more than 430 operating operating worldwide, a vast amount of experience has been gathered in the safe operation of nuclear power stations and in the handling and disposal of their waste.

All current nuclear power stations operate on the same basic principle. Neutrons in the reactor core induce fission in the nuclear fuel, releasing heat and more neutrons. This heat is used to generate steam, which in turn drives a turbine, generating electricity. The neutrons produced induce further fissions in the fuel, driving a controlled, self sustaining chain reaction.

A typical nuclear power station is composed of, amongst other elements not listed here, some or all the following major components: a reactor core which contains the fuel and is where all the heat is generated; coolant which transfers heat away from the core to generate steam to drive a turbine; moderator to slow initially fast neutrons down to thermal energies via scattering, that they might induce further fission reactions; containment building which separates the reactor core from the environment; cooling towers to vent the steam that drives the turbine; turbine that is driven by steam to generate electricity; control room where all aspects of the power plant can be monitored and controlled; and a spent fuel pool to store used nuclear fuel assemblies until they have sufficiently cooled down to be stored in concrete containers called dry casks.

There are many designs of nuclear power stations, which despite operating on

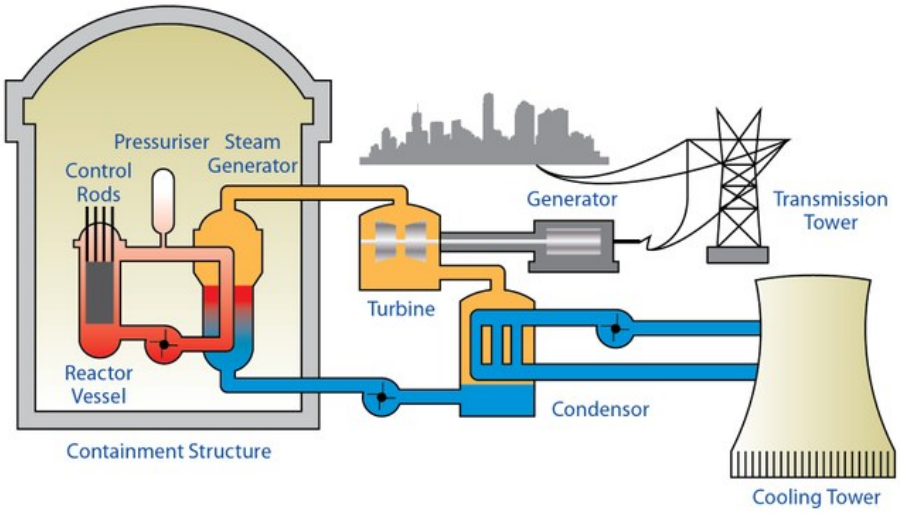

Figure 1.5: Schematic of a pressurised water reactor [10]

the same basic principle, differ in the specifics of the reactor design. The different reactors can be classified in many different ways from physical considerations such as coolant (H_2O, D_2O, CO_2, liquid metal, etc.), moderator (H_2O, D_2O, graphite, etc.) and neutron energy, to more artificial distinctions based on generation (discussed below). Figure 1.5 shows a schematic of a pressurised water reactor (PWR), the most common reactor in the world, often termed the 'workhorse' of the nuclear industry.

In the broadest sense, a reactor can be classified by whether it makes use of thermal or fast neutrons. Thermal reactors are driven by initially fast neutrons whose energies are moderated down to the ambient temperature of the reactor, at which point they are said to have been thermalised. Fast reactors have no moderator, and as the name implies use more energetic neutrons (>1 MeV) to drive fission.

The probability of whether a neutron is captured by a nucleus, elastically or inelastically scatters off it, or induces fission ($^{A}X(n,f)$) is known as the cross section. Cross sections will be discussed in detail in Section 2.1.1, so here it will just be pointed out that different reaction channels, e.g. scattering, fission and capture, all have an associated cross section, with the total cross section being given by the sum of these. The nucleus of a particular isotope may have a high cross section for fissioning with low energy neutrons and a low cross section for fissioning with high energy neutrons and vice versa.

The only naturally occurring fissile isotope is ^{235}U, and this is part of the reason it is the pre-eminent fuel used today in all current reactors, and forms the basis of

the uranium/plutonium fuel cycle that will be discussed in Section 1.2.2. It should be noted here that nuclei can be described as being fissionable, fissile or fertile. A fissionable nucleus is one that is capable of undergoing fission upon absorbing a neutron, whereas a fissile nucleus is one that is fissionable with thermal neutrons. A fertile nucleus is one that upon capturing a neutron, becomes fissile, but is otherwise unlikely to fission upon thermal neutron absorption. Natural uranium mined from the earth consists of 99.3% ^{238}U, 0.7% ^{235}U and a trace amount of ^{234}U coming from the α-decay of ^{238}U. To sustain a chain reaction in a conventional thermal reactor requires that natural uranium be enriched to 3-5% in ^{235}U. This fuel is a solid oxide referred to as UOX or UO_2. As it is predominantly fertile ^{238}U, neutron capture can convert this to fissile ^{239}Pufollowing two β-decays, and plutonium fission is responsible for one third of the energy output of a reactor. Recycled plutonium from Spent Nuclear Fuel (SNF) can be turned into PuO_2, or PuOX, which can be mixed with UOX to form a mixed oxide, or MOX fuel. Thorium fuel, ThO_2 or ThOX, is fertile and upon capturing a neutron becomes ^{233}U, following two β-decays, which is fissile and can drive a chain reaction. A typical reactor operates around 300°C and once thermalised, the probability of a neutron being captured by ^{233}U, ^{235}U or ^{239}Pu, and inducing fission is greatly enhanced. However, as ^{233}U, ^{235}U and ^{239}Pu have a lower fission cross section at higher energies, a Fast Neutron Reactor (FNR) needs uranium fuel to be enriched to as high as 20% to get an equivalent amount of energy out.

SNF removed from a conventional reactor will have less fissile material than the fresh fuel that was originally inserted into the core. In this respect, the reactor is called a 'burner'. Depending on the configuration of the reactor core/fuel assembly, it is possible to create a situation where a reactor generates more fuel than it consumes. If this is the case, the reactor is called a breeder and results in the possibility of a thermal breeder reactor or a fast breeder reactor (FBR).

Fast reactors are being actively researched for several reasons such as being up to 100 times more efficient at consuming uranium fuel than current reactors [11]. They are also capable of burning actinides, half of which are fissionable but not fissile and thus require fast neutrons to keep the chain reaction going. They are however more expensive to build and operate. Being more efficient, the reactors are smaller and have a higher power density than conventional reactors requiring more efficient coolants. To this end, liquid metals such as sodium and lead are considered. But they bring with them unique corrosive properties and, in the case of sodium, safety concerns regarding leakage due to its reactivity with water.

Conventional UOX fuel can be used in the construction of a fast breeder reactor, whereas thorium is unique in that it enables the building of a thermal breeder reactor, a situation that is simply not possible with conventional fuel due to its lower neutron economy.

The attractiveness of the thorium cycle lies in that it not only produces less actinides than current uranium based thermal reactors, due to the lower mass number of the fuel, but that it is possible to use thorium in current reactors without extensive modification. In the near term this could result in a greatly reduced stockpile of radioactive waste before the next generation of reactors are rolled out.

The future generation of reactors is being steered by the Generation IV International forum (GIF) [12]. Commencing in 2000, this consortium of the 13 nations most heavily invested in nuclear energy has proposed six reactor designs which it has concluded offer the best direction for research and development. The basis of this selection was that these six designs will offer the greatest fuel efficiency, minimise the production of transuranic waste (TRUW), offer increased proliferation resistance, enhanced safety features and are economically competitive with existing energy sources. The six Generation IV designs include three FNRs, a molten salt reactor (MSR), a very high temperature reactor (VHTR) and a supercritical water reactor (SCWR). Of these, the MSR and VHTR are very well suited for thorium fuel.

In naming the future fleet of reactors Generation IV, an arbitrary distinction was made between past and current technologies. Generation I were early prototype reactors such at the British Magnox and the French UNGG designs. Only one Generation I reactor is still in operation in the world, located in Wales. Generation II represents the vast majority of all current reactors and includes all reactors built up to around the end of the 1990s. And generation III reactors were taken be those built after 1996. As of today the only Generation III reactors that were built are in Japan. Each generation was to see an advancement in fuel economy, cost to build and run, and safely features.

The Generation II and III reactors includes pressurised water reactors (PWR) and boiling water reactors (BWR), collectively known as light water reactors (LWR) due to using ordinary water as both coolant and moderator. There are heavy water reactors utilizing deuterium as coolant and moderator (e.g. CANDU), Gas cooled reactors utilizing CO_2 and graphite moderators such as Magnox or advanced gas-cooled reactors (AGR). In terms of moderators approximately 75%, make use of ordinary water, 20% use graphite, and the remaining 5% use heavy water (D_2O).

India, with its vast thorium reserves has taken an alternative route and implemented a three stage program to go from using pressurised heavy water reactors (PHWR) using natural uranium as fuel to stockpile plutonium to be used in a FBR. The FBR will have a ^{238}U and ^{232}Th blanket from which ^{239}Pu and ^{233}U will be bred. The ^{233}U will then be used along with a ^{232}Th blanket in a thermal breeder reactor to supply all their energy needs.

The problem in adapting current technology to use thorium lies in whether or not the reactor core can utilise a heterogeneous fuel arrangement. For a thorium reactor to be viable it needs a core of fissile material called a seed (^{233}U, ^{235}U or ^{239}Pu), surrounded by a 'blanket' of fertile thorium. This separation, or heterogeneous arrangement, is necessary to ensure enough neutrons reach the fertile thorium to breed enough ^{233}U that it can sustain fission, once the seed has been consumed.

The point to emphasize here is that many different reactors are, with some modification, capable of utilizing thorium fuel. PWR are perhaps the least flexible with regards to this, although as a Norwegian study [13] aims to show, it may be feasible, making PWR a viable first step into a global thorium fuel market. BWR would be very well suited to thorium due to greater flexibility in the fuel assemblies they can accept. PHWRs, such as India is developing, Gen IV VHTR and MSR provide future options to utilize thorium.

Should the economic, environmental and political wind shift in this direction, thorium power offers excellent neutron economy, waste reduction and extends the existing nuclear fuel inventory. To this end, large unilateral and multilateral research is under way.

1.2.2 The Thorium Fuel Cycle

An entire nuclear fuel cycle entails everything from mining the ore containing the desired fuel element to disposal of SNF. Mining, milling and fabrication of the fuel before it can be used in a reactor is known at the front end of the nuclear fuel cycle. The back end constitutes everything from removing the spent nuclear fuel, placing it in a spent fuel pool to cool down, to reprocessing the waste to extract usable fissile isotopes that were not fissioned that they can be used again in a new fuel cycle, to ultimately disposing of the waste in a geological repository. This complete cycle is shown schematically in Figure 1.6.

Figure 1.6 details what is called the uranium fuel cycle, and a key difference between the thorium and uranium cycles is the lack of an enrichment process in

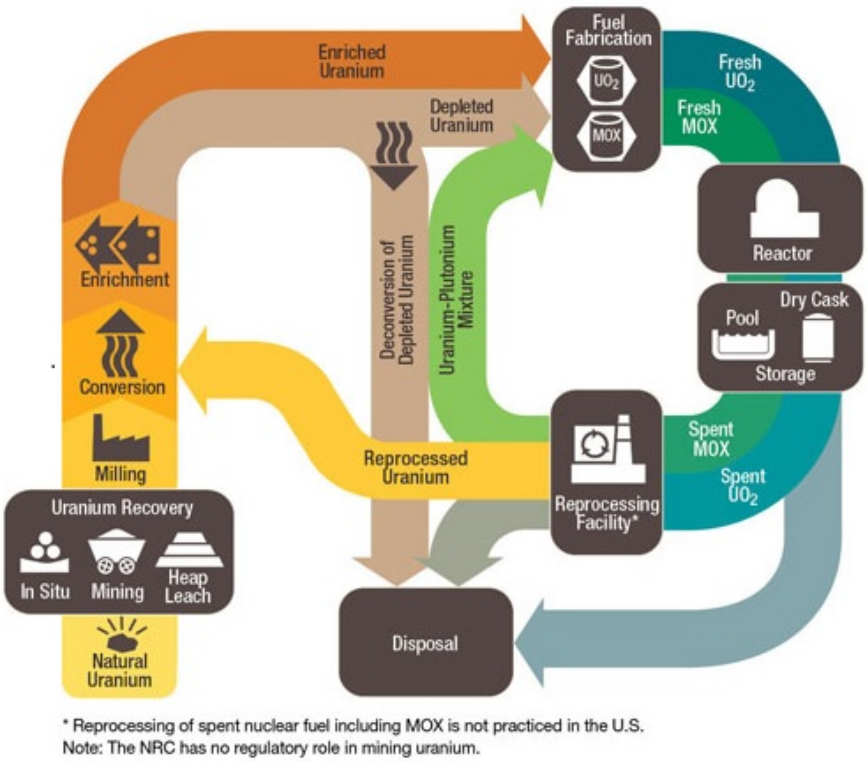

Figure 1.6: The nuclear fuel cycle [14].

the front end of the cycle. Enrichment entails processing the natural uranium in such a way as to increase the percentage of ^{235}U. This is an expensive process, and by not requiring enrichment, thorium, which is essentially mono-isotopic in nature, has a distinct advantage. It should be noted that not all reactors operating on a uranium fuel cycle make use of enriched uranium, some reactors such as the Canadian CANDU reactor and the Indian PHWR use natural uranium, although this has implications for waste as will be discussed in Section 1.2.3.

Contrary to the name, thorium is not strictly the fuel in the thorium cycle due to having a low probability of fissioning after capturing a thermal neutron. Rather, by capturing neutrons and undergoing two β–decays, it becomes an isotope of uranium which has a relatively far higher probability of fissioning after absorbing a neutron. So thorium is not a fissile element, being instead what is termed fertile.

The isotopes ^{233}U, ^{235}U and ^{239}Pu are all fissile nuclei and as such are suitable for use in thermal reactors, whilst ^{232}Th and ^{238}U are fertile, breeding ^{233}U and ^{239}Pu respectively upon neutron capture. ^{238}U is also fissionable with fast neutrons, as are all actinides.

The thorium fuel cycle can also simply refer to just the series of nuclear reactions

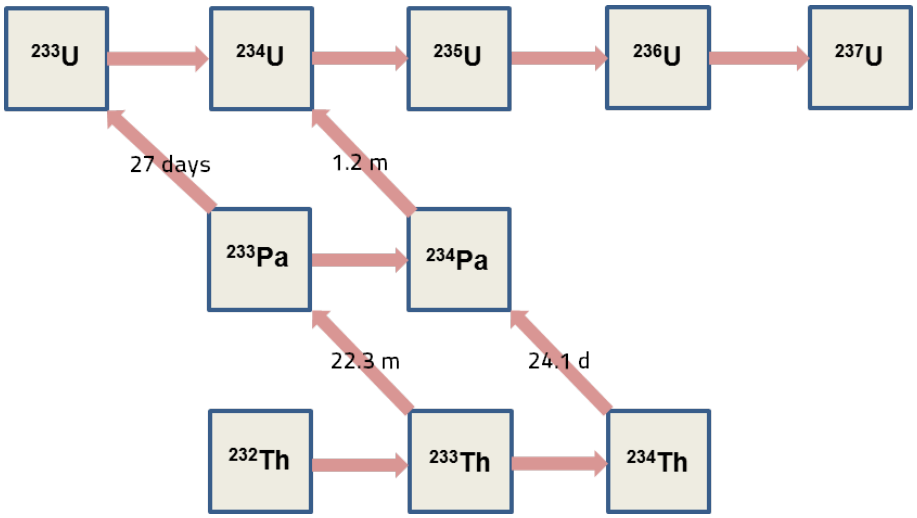

Figure 1.7: The reactions involved in the thorium fuel cycle. The horizontal arrows show neutron capture and the diagonal lines denote β-decay. Half-lives for the β-decays are also shown.

that take place in a nuclear reactor that result in the production of energy from thorium fuel pellets. This is shown in Figure 1.7 where the successive captures and decays show the progression from ^{232}Th to ^{233}U, and the β^--decay half lives.
This is also summarized in the equation below:

$$^{232}\mathrm{Th} \xrightarrow{\mathrm{n},\gamma} {}^{233}\mathrm{Th} \xrightarrow[21.8\mathrm{m}]{\beta^-} {}^{233}\mathrm{Pa} \xrightarrow[27.0\mathrm{d}]{\beta^-} {}^{233}\mathrm{U} \xrightarrow{\mathrm{n,f}} \mathrm{FP} + \mathrm{neutrons} + \mathrm{energy} \qquad (1.1)$$

Where FP denotes fission products. This is in contrast to the conventional uranium fuel cycle that is the basis of nearly all operating civilian nuclear reactors around the world (with the notable exception of Russia's FBRs). Energy is released in the conventional cycle simply as:

$$^{235}\mathrm{U} \xrightarrow{\mathrm{n,f}} \mathrm{FP} + \mathrm{neutrons} + \mathrm{energy} \qquad (1.2)$$

However, due to the majority of the fresh fuel being ^{238}U, as discussed above, a significant amount of ^{239}Pu can form inside the reactor. This releases energy via:

$$^{238}\mathrm{U} \xrightarrow{\mathrm{n},\gamma} {}^{239}\mathrm{U} \xrightarrow[23.5\mathrm{m}]{\beta^-} {}^{239}\mathrm{Np} \xrightarrow[2.4\mathrm{d}]{\beta^-} {}^{239}\mathrm{Pu} \xrightarrow{\mathrm{n,f}} \mathrm{FP} + \mathrm{neutrons} + \mathrm{energy} \qquad (1.3)$$

Table 1.1: After absorbing a neutron, ^{233}U, ^{235}U *and* ^{239}Pu *can fission releasing significant amounts of radiation and neutrons that can go on to induce further fission. These are detailed below. Values from [15].*

	^{233}U	^{235}U	^{239}Pu
Average neutrons per fission, $\bar{\nu}$	2.50	2.43	2.88
Energy Source	Energy Released (MeV)		
Instantaneously released energy			
Kinetic energy of fission fragments	168.2	169.1	175.8
Kinetic energy of prompt neutrons	4.9	4.8	5.9
Energy carried by prompt γ-rays	7.7	7.0	7.8
Energy from decaying fission products			
Energy of β^--particles	5.2	6.5	5.3
Energy of anti-neutrinos	6.9	8.8	7.1
Energy of delayed γ-rays	5.0	6.3	5.2
Total Energy	197.9	202.5	207.1

Which is also the exact same series of reactions used to create ^{239}Pu fuel in FBRs.

Having detailed the three main reactions that release energy in current and future reactors it is instructive to look to some of their properties, and these are summarised in Table 1.1 [15].

While ^{235}U(n,f) releases slightly more energy than ^{233}U(n,f), ^{233}U(n,f) results in a higher average number of neutrons per fission. This is denoted by $\bar{\nu}$ and is referred to as 'nubar'. This is of practical importance for a breeder reactor as there needs to be enough neutrons left over, after one has gone on to cause another fission, to go on to capture on a non-fuel element, namely a fertile element, so more fuel can be bred. For a thermal breeder, thorium is the only candidate where this is the case.

Although ^{239}Pu has a higher $\bar{\nu}$, considering the ratio of the capture to fission cross section at the thermal energy of an operating nuclear reactor (around 300°C for a PWR), another advantage of using ^{233}U as a fuel becomes apparent. As can be seen in Figure 1.8, these ratios are around 9% for ^{233}U(n,γ), 15% for ^{235}U(n,γ) and over 45% for ^{239}Pu(n,γ).
This means that as more neutrons incident on a ^{233}U nucleus will result fissions instead of captures, less TRUW will build up. This fact coupled with a lower atomic mass gives rise to the thorium fuel cycle having a lower environmental impact (see Section 1.2.3 for details).

Whilst using ^{239}Pu as a fuel may seem to be the clear winner from Table 1.1 as

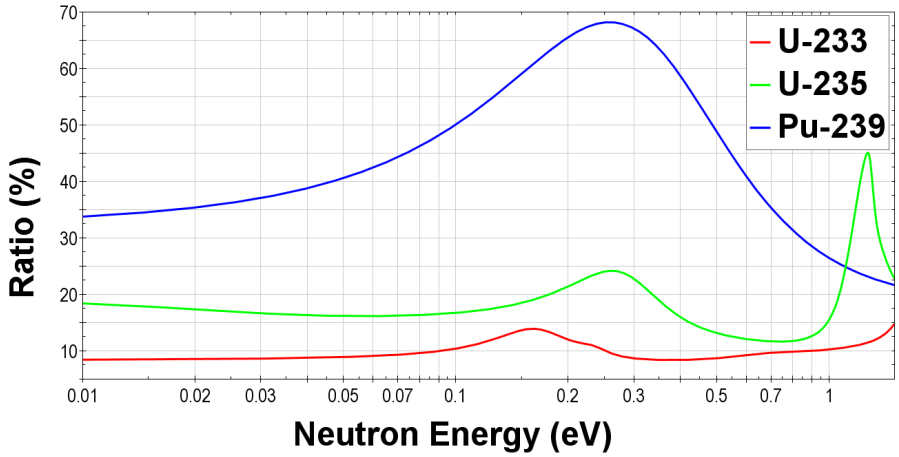

Figure 1.8: Capture to fission cross section ratios for the three main fissile isotopes. Plot produced using JANIS [16].

it has released the highest energy per fission and has the highest nubar, it also has the lowest capture to fission ratio and is an excellent material for weapons. To use plutonium entails reprocessing SNF from a conventional reactor or breeding it in a FBR, this gives rise to proliferation risks that are protected against naturally in the thorium cycle, embodied in the production of ^{232}U. During the thorium fuel cycle ^{232}U can build up via one of two main pathways:

$$^{232}\mathrm{Th} \xrightarrow{\mathrm{n},\gamma} {}^{233}\mathrm{Th} \xrightarrow[21.8\mathrm{m}]{\beta^-} {}^{233}\mathrm{Pa} \xrightarrow[27.0\mathrm{d}]{\beta^-} {}^{233}\mathrm{U} \xrightarrow{\mathrm{n},2\mathrm{n}} {}^{232}\mathrm{U} \tag{1.4}$$

$$^{232}\mathrm{Th} \xrightarrow{\mathrm{n},\gamma} {}^{233}\mathrm{Th} \xrightarrow[21.8\mathrm{m}]{\beta^-} {}^{233}\mathrm{Pa} \xrightarrow{\mathrm{n},2\mathrm{n}} {}^{232}\mathrm{Pa} \xrightarrow[1.31\mathrm{d}]{\beta^-} {}^{232}\mathrm{U} \tag{1.5}$$

The decay chain of ^{232}U contains several strong γ-emitters whose presence makes handling SNF from the thorium fuel cycle extremely hazardous, and also very easy to detect, should anybody attempt to divert SNF for the purposes of making weapons. The half-lives of the isotopes in the decay chain are all relatively short, the highest being 72 years, and thus although they are very active, they will decay to safe levels within a few hundred years.

In summary, the use of thorium has numerous advantages over uranium in a nuclear reactor: it produces less waste; higher nubar; more favourable capture to fission ratio; and is four times as abundant as uranium. All of these factors render it an attractive prospect for current and future energy demands.

1.2.3 Nuclear Waste

Nuclear waste consists of everything that needs to be disposed of in the course of reactor operation. It is categorised as either low, intermediate or high level waste (LLW, ILW and HLW respectively) based on its radiotoxicity. The majority, some 90% by volume [5] is LLW which consists of clothing and tools that become slightly contaminated during reactor operation, and is safely disposed of in effectively the same way as household waste is in a landfill. Around 7% is ILW which comes from components within the reactor that become activated, and effluent from the reprocessing of nuclear waste. The final 3% is HLW, which is also responsible for 95% of the radioactivity, and it is this that is comprised of FPs and TRUW and requires very careful treatment and disposal. This is briefly outlined shortly.

It was mentioned above that the thorium cycle produces less TRUW than the conventional uranium cycle. Why is this the case? The conventional uranium cycle utilises fuel that contains around 97% ^{238}U. Whilst having a low fission and capture cross section at thermal energy relative to ^{235}U, due to the large volume in the reactor, a significant number of ^{238}U nuclei will capture a neutron and result in a build up of ^{239}Pu, as shown in equation 1.3, and from here build up other transuranics such as neptunium and curium.

The half-life of ^{239}Pu is 24,110 years meaning it remains in the reactor long enough that they are able to undergo further captures to higher mass isotopes. These TRU are a source of long lived radioactive waste (LLRW) with half-lives ranging from 24,000 to 80 million years, thus adding to a radiotoxic inventory that needs storing for millennia.

In the thorium cycle, it is when ^{236}U is formed that the build up of TRU can begin, and this is why it is an important isotope to accurately measure for nuclear data needs. Successive captures on ^{233}U will lead to ^{234}U and then ^{235}U, which is itself fissile so will be consumed in fission reactions. Following captures on ^{235}U to create ^{236}U, it is only now, after some hard work, that TRUW can begin to build up, and as a first step would be as follows:

$$^{236}\mathrm{U} \xrightarrow{\mathrm{n},\gamma} {}^{237}\mathrm{U} \xrightarrow[6.75\mathrm{d}]{\beta^-} {}^{237}\mathrm{Np} \tag{1.6}$$

However, as outlined above, due to the nature of ^{233}U having a lower mass number it is naturally more difficult to produce TRUW which, in terms of environmental impact, and the economics of treating and storing waste, is a large advantage of the

thorium cycle.

All fuel cycles result in a build up of FPs, which have a wide range of half-lives, and are grouped in to short lived (SLFP), medium lived (MLFP) and long lived (LLFP). SLFPs have half lives of at most a few years and quickly decay away. Activity from MLFPs, and in SNF as a whole, are dominated by ^{137}Cs and ^{90}Sr for several hundred years, with both isotopes having approximately 30 year half-lives. LLFPs have half-lives in excess of 200,000 years and are a more long term problem [5].

Processing the SNF involves storing fuel assemblies in a spent fuel pool, where it may remain for up to 40 years, but typically 10 to 20 years, to enable it to cool down as the SLFPs decay away. It is then removed for reprocessing or dry cask storage. Reprocessing entails liquefying the SNF before extracting useful isotopes. This liquid waste is then vitrified in glass and locked away in steel containers before being stored. If the SNF is not to be reprocessed, it goes to dry cask storage which entails sealing it in steel casks which are then welded shut and surrounded by concrete or more steel to shield it from the environment.

After 40 to 50 years, both the radioactivity and the heat of the SNF have reduced to one thousandth that of its level when it was removed from the reactor. It is now ready for permanent disposal in a geological repository. Geological disposal currently is the best option available and the most likely to be adopted [17].

Future reactors may be able to incinerate TRUW, and partitioning and transmutation (P&T) may allow the reduction of the FP inventory, but these are solutions not yet available. In the mean time, the thorium cycle offers a way to reduce humanities radiotoxic inventory in the both the near term and in future reactor systems.

1.3 Nuclear Data

In the context of the design of nuclear plants, nuclear data is a compilation of experimental and evaluated data that describes nuclear properties. These properties include, amongst others, spin, parity, energy and angular distributions of reaction products, reaction cross sections and partial widths, and level densities.

It is of vital importance not only to nuclear energy, but also to many fields outside of this. The following sections will look at where nuclear data plays a role, how and where it is stored for use by the relevant communities, and finish with a review of the current state of ^{236}U - the isotope that forms the subject of the current work.

1.3.1 The Need For Accurate Nuclear Cross Sections

In the current work, the interest in nuclear data is with regard to the thorium fuel cycle and the build up of TRUW. Precise measurements of neutron capture and induced fission cross sections allow for more accurate determination of reaction rates in a reactor. This enables the optimisation of reactor design and has implications for transmutation, waste disposal, operation safety and radiation shielding, which in turn has obvious cost reduction factors. Abandonment of thorium in favour of the uranium fuel cycle in the 1970s means that not enough reaction data are currently available for many relevant isotopes, and what does exist shows large discrepancies, as is discussed in Section 1.3.3.

Obtaining accurate neutron reaction cross section data is not the sole pursuit of the nuclear data community. Charged particle data, angular distribution, photo-nuclear, and fission yield data are amongst the myriad information that is obtained through measurement to then be evaluated and disseminated. This data is stored in freely accessible data libraries, which will be discussed in Section 1.3.2.

This nuclear data is vital in a wide variety of fields: nuclear medicine for the production of radioisotopes and dose calculation; astrophysics to determine the origins and abundances of the elements we see in the universe; basic physics to enable testing of theoretical models and designing experiments; and national security for nuclear forensics, emergency response and the detection of diverted nuclear material. Thus even outside the domain of nuclear energy, there is a strong need for accurate nuclear data.

Whilst it is true that a large effort is under way to study reactions of interest for many of the isotopes involved in the various fields, it remains a fact that, for many them, nuclear data are either not known to sufficient accuracy or are absent entirely.

1.3.2 Nuclear Data Libraries

In the past, individual laboratories created cross section evaluations for their own reactor calculation needs. In this way, they not only determined for themselves what materials to study, but also the energy ranges to investigate and what data to extract. In doing this, they also developed their own bespoke methods for storing and retrieving this data.

A data library consists of a collection of data files, which are defined as complete set of evaluated cross section data for a single material. Single material meaning

a specific isotope, metastable state, compound or natural element. Further, an evaluation is a combination of experimental data with nuclear model calculations for the purpose of extracting complete cross sections. Where data for a full energy range is not available, the data is interpolated to enable values for whole energy regions to be determined. Were the data not complete, transport calculations would be impossible due to missing data.

Detailed data libraries were accessible by 1963, however, performing identical reactor calculations with data from different libraries gave different answers. That the different libraries were all stored in different formats made understanding the differences problematic.

It was clear that a standard format needed to be developed and in 1964 the evaluated nuclear data file (ENDF [18]) format was settled upon in the United States. ENDF stands for not only the format, but for the name of the American data library. Many other data libraries exist, and all have adopted the ENDF format. The other major libraries are JEFF [19], JENDL [20], BROND [21] and CENDL [22] which are the European, Japanese, Russian and Chinese libraries respectively.

The data files in libraries are organised using MAT, MF and MT numbers. The MAT number indicates the material, (i.e. isotope such as ^{236}U, ^{232}Th, etc.), MF is a file number from 1 to 36, where for example MF=3 is cross section data. MT is the section number designating the reaction type, e.g. MT=1 is the total cross section, MT=2 is elastic scattering, MT=18 is fission, and MT=102 is radiative capture.

As more data becomes available, only after undergoing rigorous benchmarking and testing is it possible for this data to be used in a new evaluation for use by the nuclear data community. All of the evaluations are made available by the IAEA Nuclear Data Services [23].

1.3.3 Current Status Of The ^{236}U Capture Cross Section

For many materials in the different data libraries, the data from different experiments may cover different energy regions. And in the case where they cover the same energy region, discrepancies may exist. Also, different libraries have made use of different sets of data according to their preferences and may have access to data not widely available. This situation serves to bring about differences in various evaluations. Where the discrepancies are large, there is a clear need for new, more accurate experimental data. Indeed, this is the situation for the ^{236}U neutron capture cross section.

As stated above, ^{236}U is where the build up of TRUW occurs in the thorium cycle, and as such accurate nuclear data on the capture cross section is necessary for reactor calculations.

Looking to the evaluations, it is instructive to divide the cross section into three separate energy ranges. These are termed the 1/v region, the resolved resonance region (RRR), and the unresolved resonance region (URR). These will be looked at in turn, where use will be made of the ENDF, JEFF and JENDL evaluations for comparison.

The 1/v region, shown in Figure 1.9, shows a smooth trend where the three evaluations are in good agreement with one another. For example, the thermal cross section of ENDF/B-VII.1 and JENDL-4.0 agree within 0.2%, and both agreeing with JEFF-3.2 around 3%. The only set of data covering the energy range from thermal to the start of the RRR was performed by Carlson [24] in 1970, and would appear to be the basis of all the evaluations in this region. All other data correspond to 0.0253 eV where good agreement is shown in general with the Carlson data.

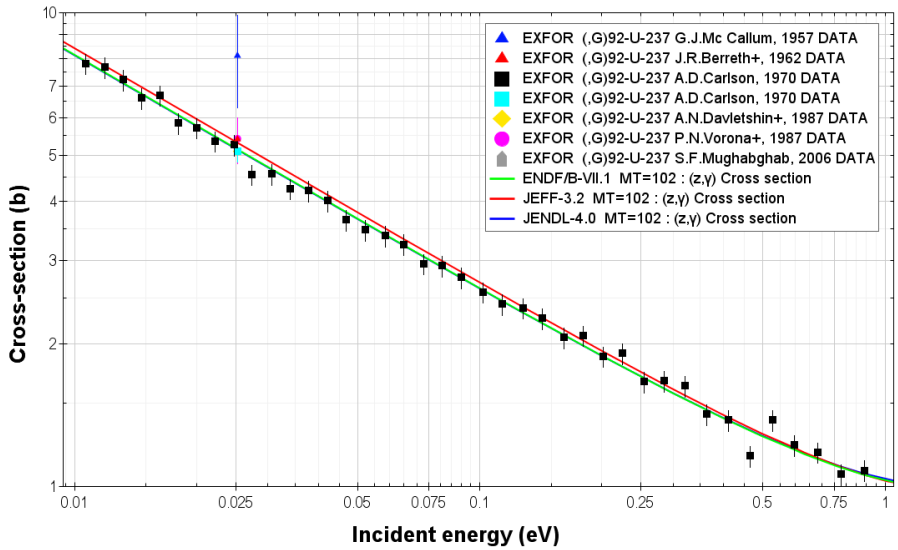

Figure 1.9: Plot showing the 1/v region for three of the major evaluations. Also plotted is the majority of the experimental data available in the EXFOR database for this region.

The RRR extends from a few eV to 1.5 keV for most evaluations, and 4 keV in the JENDL-4.0 evaluation. There is no point-wise data available for the whole energy region. What data are available are stored in the EXFOR database [23] mainly in the form of average cross sections covering small energy regions as can be seen in Figure 1.10, which shows various experimental data plotted over the evaluations.

Only a few measurements are available in the RRR for the evaluators [25] [26] [27]

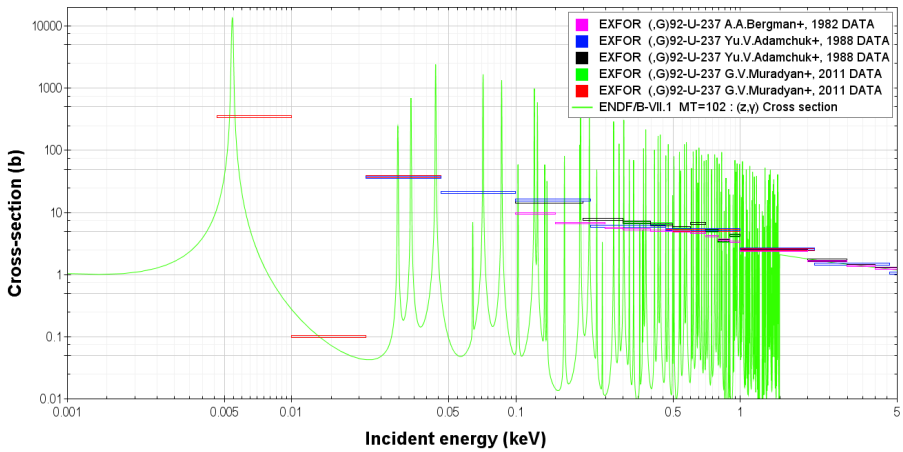

Figure 1.10: Plot showing the resolved resonance region from the ENDF/B-VII.1 database. Also plotted is the only data available in the EXFOR database which consists of average cross sections.

[28] [29], and the different evaluations make use of different combinations of these measurements, the evaluations show differences in both resonance height and energy, in some cases, quite markedly so. Figures 1.12 and 1.13 highlight some of these discrepancies. Figure 1.12 shows that slight differences exist in resonance energy about 34.1 eV and differences of up to 40% are seen in cross section. Figure 1.13 shows the situation about 416 eV where the JEFF 3.2 evaluation shows a marked difference in resonance energy from the other evaluations. These situations highlight what is typical of the RRR, and is shown in Figure 1.11, where the average difference between resonance areas, known as kernels, for the different libraries ranges from 7-15%. A fuller discussion of this is presented in the context of the results in Section 5.2.

The situation in the URR is shown in Figure 1.14. Depending on the evaluation, this extends from 1.5 keV or 4 keV onwards, where the distance between resonances is less their intrinsic widths, thus making it impossible to distinguish individual resonances. The majority of the available data in the URR below 200 keV are average cross sections. There is reasonable agreement amongst the evaluations but not amongst the data. Above 200 keV, the evaluations show discrepancies and the data show large variation.

Thus the present situation is that the majority of the data available are from the 1970's and 1980's, and which cover incomplete energy ranges coupled with poor resolution and accuracy. The present situation is therefore unacceptable for nuclear data needs where accurate data are necessary for reliable calculations pertaining

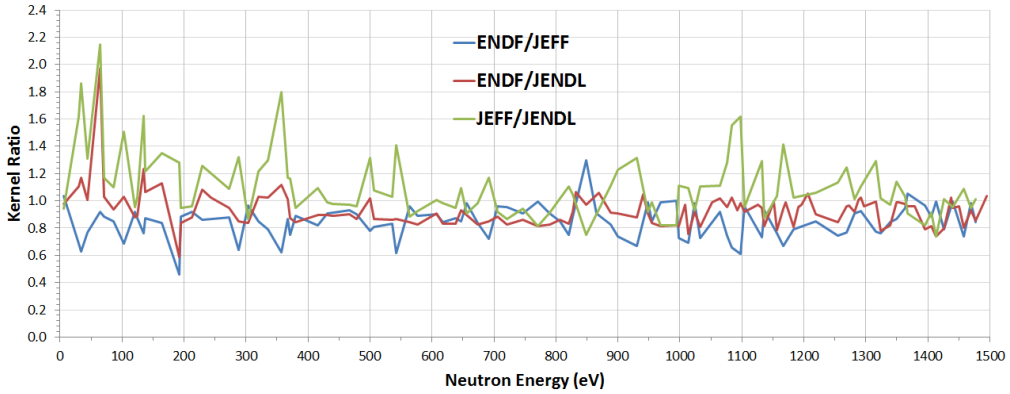

Figure 1.11: Kernel ratios of the ENDF, JEFF and JENDL libraries. The average kernel difference between the ENDF and JEFF libraries is 15%, between the JEFF and JENDL libraries is 7%, and between ENDF and JENDL is 11%.

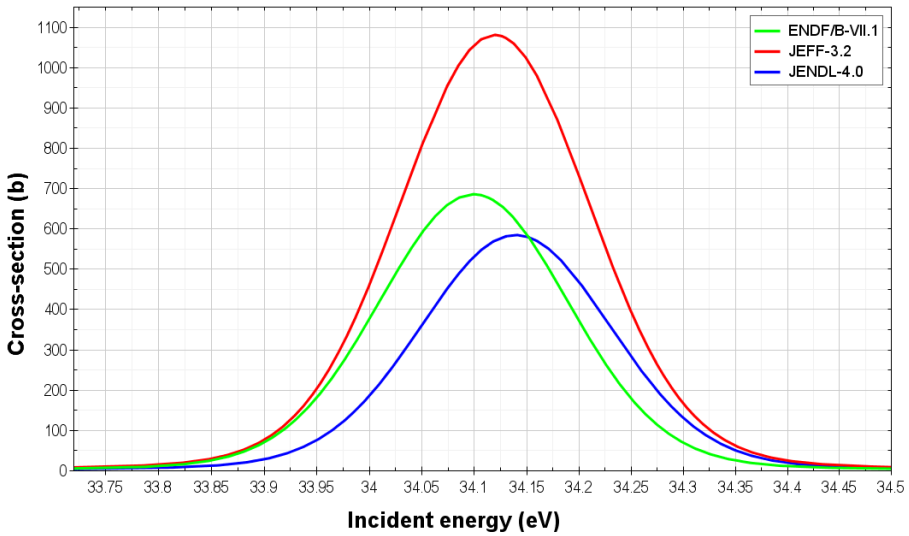

Figure 1.12: Plot from three of the major evaluations in the RRR, highlighting differences in the 34.1 eV resonance strength and energy.

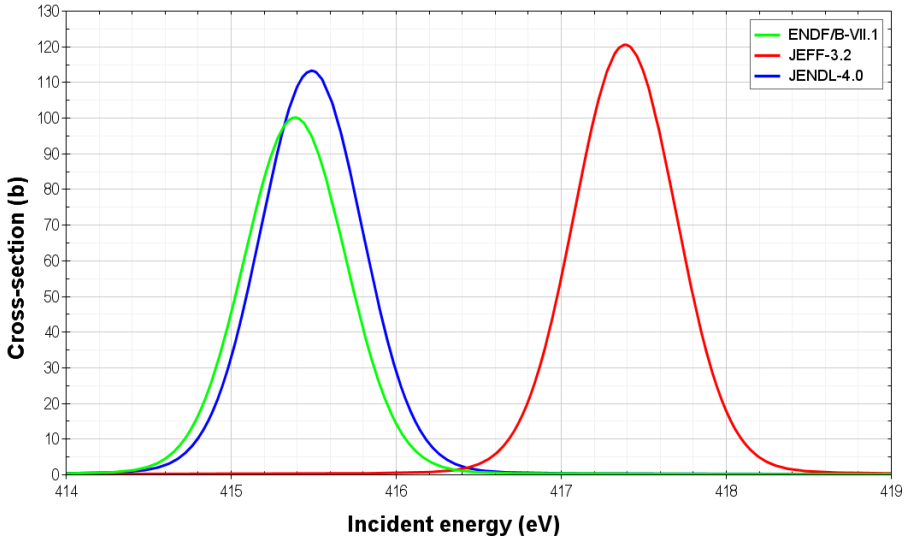

Figure 1.13: Plot from three of the major evaluations in the RRR, highlighting differences in the 416 eV resonance strength and energy.

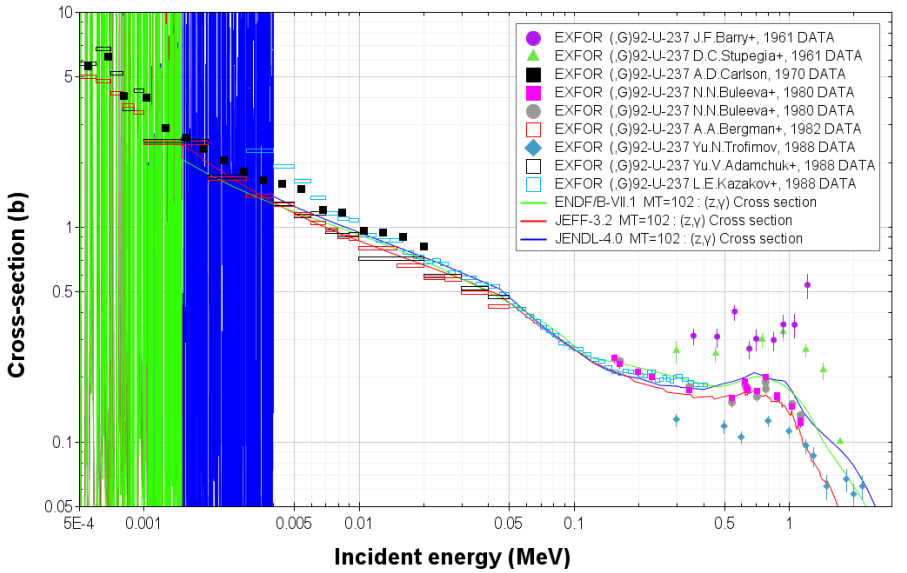

Figure 1.14: Plots from three of the major evaluations in the URR. The majority of the available data in the RRR below 200 keV are average cross sections. There is reasonable agreement amongst the evaluations but not amongst the data. Above 200 keV, the evaluations show discrepancies and the EXFOR data show large variation.

to future reactors and fuel cycles. This prompted a proposal for a new accurate measurement, covering the RRR with an accuracy better than 10%, aiming for 5%. This forms the basis of the current work.

Chapter 2

Particulars Of Neutron Capture Reactions

This chapter will first introduce the concepts and theory behind neutron induced reactions, before going on to discuss one particular method of performing neutron capture cross section measurements - the time-of-flight (TOF) technique. Relevant experimental effects affecting the measurements are then considered before turning to a brief discussion of the R-matrix code SAMMY, which is used in this work to analyse the resonances observed in the capture yield, allowing to reconstruct the cross section that is the final goal of this work.

2.1 Concerning The Theory Of Cross Sections

In order to understand what is observed in an experiment, it is necessary to understand the principles and mechanisms that govern the nuclear reactions being studied. This section will therefore introduce the basics of reaction cross sections and the theory of compound nucleus (CN) and the resonance structure that typifies CN formation. Potential scattering will be looked at, and an equation derived for the scattered wave function that introduces the elements of the collision matrix - an important ingredient of R-matrix theory. R-matrix theory itself will then be considered, looking at how it is used to describe the resonance data and extract resonance parameters.

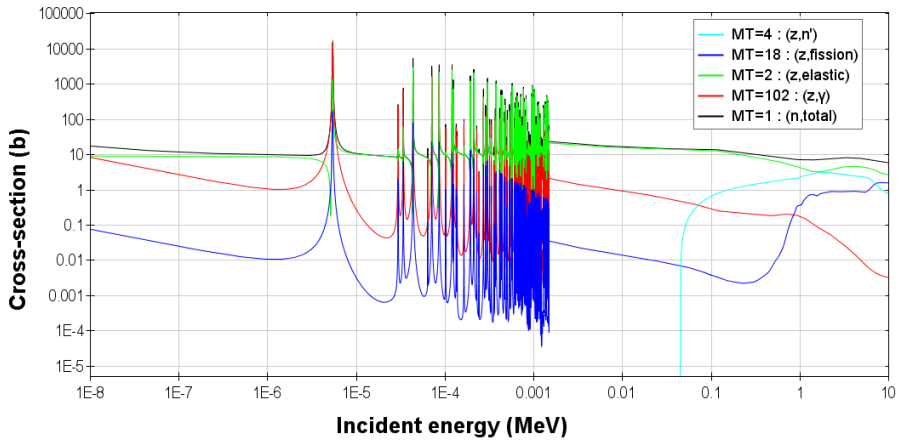

Figure 2.1: Plot of all the relevant incident neutron induced reaction cross sections on ^{236}U*. This plot was made in JANIS [16] using the ENDF/B-VII.1 library [18]. Below the fission threshold (≈ 1 MeV) capture dominates over fission, up to two orders of magnitude below 300 keV,and thus in this range, fission can be neglected.*

2.1.1 Basics Of Neutron Induced Reactions

When a neutron is incident upon some nucleus, various reaction channels are accessible, such as elastic scattering, inelastic scattering, fission, capture, alpha emission, and so on. Associated with each of these channels is a probability that a given reaction channel proceeds. The probability of one or another reaction taking place is quantified via a parameter called the cross section, and is measured in units of barns (10^{-24} cm^2), with the total cross section σ_t being the sum of the partial cross sections:

$$\sigma_t = \sigma_{n,n} + \sigma_{n,n'} + \sigma_{n,\gamma} + \sigma_{n,f} + \sigma_{n,\alpha} + \dots \tag{2.1}$$

At the energies used in current work (<20 keV), only the elastic and capture channels contribute significantly to the total cross section. Figure 2.1 highlights this situation where it can be seen that the fission cross section is always at least two orders of magnitude below the capture cross section, and only becomes important around 1 MeV. The inelastic scattering channel only opens up at 45 keV, corresponding to the first excited state in ^{236}U.

Classically, the cross section is simply the geometrical area that a target, considered as a solid sphere, offers to an incident point particle, given by πR^2, where R is the radius of the target nucleus. Experimentally, the cross section can be understood as follows. The reaction rate, $R\,(\text{reactions}\,\text{s}^{-1})$, for a beam of intensity $I\,(\text{particles}\,\text{cm}^{-2}\,\text{s}^{-1})$, incident on a target with area $A\,(\text{cm}^2)$, thickness $\Delta x\,(\text{cm})$

with a particle density N (particles cm^{-3}), are related by the proportionality:

$$R \propto I \cdot N \cdot A \cdot \Delta x \tag{2.2}$$

The proportionality constant necessary to turn this into an equality is the cross section, σ, with units of area (cm^2), which are so small they are usually expressed in terms of barn, where 1 barn = 10^{-24} cm^2.

$$R = \sigma \cdot I \cdot N \cdot A \cdot \Delta x \tag{2.3}$$

It is clear from Figure 2.1 that the cross section can vary wildly with energy, rapidly increasing by many orders of magnitude over relatively short energy intervals. This resonant structure arises through the formation of a compound nucleus, which is considered next.

2.1.2 Compound Nuclear Reactions

When an incident neutron approaches a target nucleus, there is a certain probability that they will interact with one another. Depending on the energy of the neutron, either a compound or direct nuclear reaction will be most probable. For a neutron energies above 10 MeV, the de Broglie wavelength of the particle is similar to that of individual nucleons in the target nucleus, and thus is most likely to interact with a surface nucleon in a direct reaction which entails the direct population of bound states. As they are stable against particle emission, the populated states have relatively long lifetimes of the order of picoseconds.

At lower energies, the de Broglie wavelength of the particle is of the same order as that of the target nucleus, and compound nuclear reactions become more probable than direct reactions. In this situation, when the incident neutron interacts with a nucleon, the recoiling nucleon and the incident particle may then make successive collisions with other nucleons in, distributing the energy of the incident particle amongst all the nucleons. The average increase in energy of any given nucleon is not enough for it to be ejected from the nucleus, but as many random collisions give a statistical distribution of energies, this leads to a small probability that a given nucleon may gain enough energy to free itself from the nucleus [30]. This gives rise to a clear, quasi-bound, intermediate state that exists following the absorption of an incident neutron, and before the emission of any particles [30]. This is illustrated in the following reaction equation, where instead of the reaction proceeding directly

via:

$$\mathrm{a} + \mathrm{X} \rightarrow \mathrm{Y} + \mathrm{b} \tag{2.4}$$

it instead proceeds by:

$$\mathrm{a} + \mathrm{X} \rightarrow \mathrm{C}^* \rightarrow \mathrm{Y} + \mathrm{b} \tag{2.5}$$

Where a, X, Y and b are the projectile, target, daughter and ejectile particles respectively. C^* denotes the intermediate state called the CN, and the asterisk denotes an excited state of the CN, which, after absorbing a neutron with kinetic energy E_n, has an excitation energy, E^*, given by:

$$E^* = S_n + \frac{A}{A+1} \cdot E_n \tag{2.6}$$

Where S_n is the neutron separation energy of the CN, and A is the mass number of the target nucleus. The $A/(A+1)$ term accounts for the fact that not all of the neutrons kinetic energy goes into the excitation energy of the CN, but a small fraction goes into the recoil of the nucleus to conserve momentum. Figure 2.2 illustrates this situation.

The CN may then, after some 10^{-16} to 10^{-18} seconds, decay by any exit channel open to it. This time frame is some four to six orders of magnitude longer than the time it takes for direct reactions to occur (which are of the order of 10^{-22} seconds), and this excess time is due to the redistribution of energy within the nucleus.

The theory of the CN was introduced by Niels Bohr in 1939 [32] to explain features observed in low energy neutron-nucleus reactions, namely resonances. Resonances are explained as the capture of neutrons into discrete, excited, unbound, states of a CN. At low neutron energies there is usually only two exit channels available in non-fissile nuclei as studied in the present work - elastic scattering and radiative capture, which may be written thus:

$$\mathrm{n} + {}^{\mathrm{A}}\mathrm{X} \rightarrow {}^{\mathrm{A+1}}\mathrm{X}^* \rightarrow {}^{\mathrm{A}}\mathrm{X} + \mathrm{n} \tag{2.7}$$

$$\mathrm{n} + {}^{\mathrm{A}}\mathrm{X} \rightarrow {}^{\mathrm{A+1}}\mathrm{X}^* \rightarrow {}^{\mathrm{A+1}}\mathrm{X} + \gamma \tag{2.8}$$

The fission channel is open at all energies, but is so low below the fission threshold that it can be effectively ignored. Due to being in a highly excited state, the CN, if it undergoes a capture reaction, emits a gamma cascade to reduce its energy to the

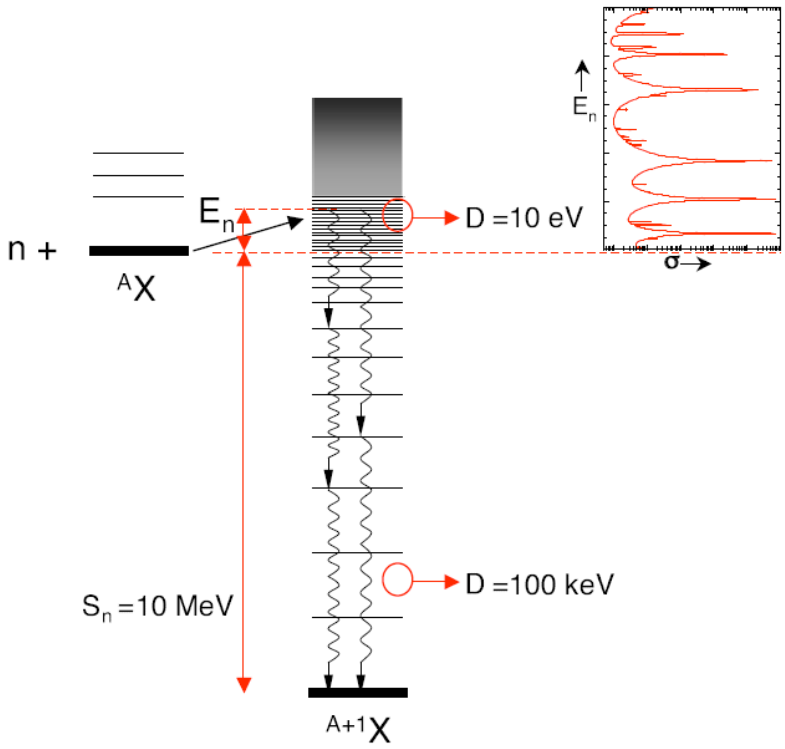

Figure 2.2: Illustration of neutron capture resulting in the formation of a CN. The neutron is captured in to an unbound state above the neutron separation energy, S_n. The probability that a CN is formed depends on how close then energy of the incoming neutron is to a state in the CN. Image from [31].

ground state. Figure 2.2 shows that the neutron is captured into an unbound state, above the neutron separation energy in the CN.

At low neutron energies, the width of the resonances is smaller than the space between them and thus they can be resolved. This is called the resolved resonance region (RRR) (discussed in 1.3.3). These resonance widths are related, via Heisenberg's uncertainty principle, to the half-life of the corresponding unbound state:

$$\tau \approx \frac{\hbar}{\Gamma} \tag{2.9}$$

Where the total width of the state is the sum of all the partial widths from all possible reaction channels.

$$\Gamma = \Gamma_n + \Gamma_\gamma + \dots \tag{2.10}$$

At higher neutron energies, due to the limits of experimental resolution, it is not possible to resolve individual resonances even though they may be well separated, and this region is referred to as the URR (see 1.3.3). At higher energies still, the density of states is such that the spacing of individual states is less than the widths of the states, and the individual resonances overlap, in what is termed the high energy region.

Due to the complex structure of the resonances, it is impossible to predict with theory what the individual resonance cross sections will be. These are only accessible through experiment and the subsequent analysis of the data. Attention will now turn to the formalism of scattering, before turning to the R-matrix formalism which provides the framework for describing neutron-nucleus compound nuclear reactions.

2.1.3 Potential Scattering

The scattering of particles from a nuclear potential is considered for the case of spinless, neutral particles interacting with a spherically symmetric potential. Potential scattering is the only reaction that can take place in isolation. If the conditions permit other reactions to occur, potential scatter will still always be present. Further, it does not feature resonances and is not followed by the formation of a CN.

To look at potential scattering, partial wave analysis is invoked. This entails expressing the incoming plane wave representing the neutron e^{ikz}, as a linear superposition of eigenfunctions of the scattering potential. Incoming plane waves are expressed as a sum of an incoming and outgoing spherical waves, which are respec-

tively converging and emerging from the target nucleus.

The derivation of potential scattering is useful as it leads to the introduction of a complex coefficient that modifies the outgoing wave after a reaction. This complex coefficient turns out to be an element of the collision matrix (aka scattering matrix), which is a key component of R-matrix theory. Thus the discussion of potential scattering will then lead to a discussion of R-matrix formalism.

Separation of variables means the Schrödinger wave equation in three dimensions can be written:

$$\psi(r,\theta,\phi) = R(r)Y(\theta,\phi) \tag{2.11}$$

Where $R(r)$ is the radial part of the Schrödinger equation and $Y(\theta,\phi)$ are the spherical harmonics. The spherical harmonics can be separated further as $Y(\theta,\phi) = \Theta(\theta)\Phi(\phi)$, and the solution to the $\Theta(\theta)$ part can be expressed in terms of Legendre polynomials. $Y(\theta,\phi)$ are eigenfunctions of $\hat{L}^2$, where $\hat{L}$ is the angular momentum operator. Solving for $Y(\theta,\phi)$ using the angular part of the Laplacian yields:

$$\hat{L}^2 Y_{\ell,m}(\theta,\phi) = \hbar^2 \ell(\ell+1) Y_{\ell,m}(\theta,\phi) \tag{2.12}$$

Where we have the centrifugal barrier or centrifugal potential. When $\ell > 0$ this term acts to keep the interacting particles apart due to centrifugal force.

It is common when dealing with the radial equation to use $R(r) = r\chi(r)$ to simplify the maths:

$$-\frac{\hbar^2}{2\mu}\left(\frac{d^2}{dr^2} - \frac{\hbar^2}{2\mu}\frac{\ell(\ell+1)}{r^2}\right)\chi_\ell(r) + V(r)\chi_\ell(r) = E\chi_\ell(r) \tag{2.13}$$

Where E is the eigen energy and μ is the reduced mass of the neutron-nucleon system. Solutions to the radial part of the Schroedinger equation far from the potential, where $V(r)$ can be taken as zero, give rise to the spherical Bessel functions. These are expressed in dimensionless form as:

$$\chi_\ell(r) = krj_\ell(kr) \tag{2.14}$$

It is convenient to express the incoming wave as a linear combination of spherical waves, with one wave converging on the target nucleus and an outgoing wave that originated at the target nucleus. This combination of in incoming and outgoing spherical wave is simply a plane wave, which is what is expected:

$$\psi_{inc} = Ae^{ikz} = A\sum_{\ell=0}^{\infty} i^{\ell}(2\ell+1)j_{\ell}(kr)P_{\ell}(cos\ \theta) \tag{2.15}$$

Far from the nucleus, a standard expression for the $j_\ell(kr)$ is:

$$j_{\ell}(kr) \approx \frac{sin(kr - \frac{1}{2}\ell\pi)}{kr} = i \cdot \frac{e^{-i(kr-\ell\pi/2)} - e^{i(kr-\ell\pi/2)}}{2kr} \tag{2.16}$$

Substituting 2.16 into 2.15 therefore gives:

$$\psi_{inc} = \frac{A}{2kr}\sum_{\ell=0}^{\infty} i^{\ell+1}(2\ell+1)[e^{-i(kr-\ell\pi/2)} - e^{i(kr-\ell\pi/2)}]P_{\ell}(cos\ \theta) \tag{2.17}$$

This linear combination of incoming and outgoing spherical waves to form a plane wave are, for a given value of ℓ, called partial waves. Any change in the ℓ^{th} outgoing partial wave are accounted for by introducing a complex coefficent U_ℓ in the following manner:

$$\psi = \frac{A}{2kr}\sum_{\ell=0}^{\infty} i^{\ell+1}(2\ell+1)[e^{-i(kr-\ell\pi/2)} - U_{\ell}e^{i(kr-\ell\pi/2)}]P_{\ell}(cos\ \theta) \tag{2.18}$$

Which is the superposition of the incoming and scattered waves. Thus to obtain the scattered wave, 2.17 must be subtracted from 2.18:

$$\psi_{sc} = \frac{A}{2kr}\sum_{\ell=0}^{\infty} i^{\ell+1}(2\ell+1)(1-U_{\ell})e^{i(kr-\ell\pi/2)}P_{\ell}(cos\ \theta) \tag{2.19}$$

By bringing the e^{ikr} term out of the summation, it can be seen that there is a spherical wave of the form e^{ikr}/r multiplied by a group of other terms:

$$\psi_{sc} = \frac{e^{ikr}}{r}\frac{A}{2k}\sum_{\ell=0}^{\infty} i^{\ell+1}(2\ell+1)(1-U_{\ell})e^{-i\ell\pi/2}P_{\ell}(cos\ \theta) = \frac{e^{ikr}}{r}\cdot f(\theta) \tag{2.20}$$

where $f(\theta)$ is known as the scattering amplitude. The differential cross section is given by:

$$\frac{d\sigma}{d\Omega} = |f(\theta)|^2 \tag{2.21}$$

which emerges from consideration of the incoming and scattered particle current densities. Taking 2.21 and integrating the modulus squared of $f(\theta)$ over all solid angles, taking into account the orthogonality of the Legendre polynomials, thus gives

the cross section for elastic scattering as:

$$\sigma_{sc} = \sum_{\ell=0}^{\infty} \frac{\pi}{k^2}(2\ell+1)|1-U_\ell|^2 \tag{2.22}$$

Elastic scattering will always occur,even in the absence of other reactions, but other reactions cannot occur in isolation. Thus there will always be at least elastic scattering accompanying any other reaction.

When dealing with elastic scattering with a real potential, the collision matrix is diagonal in angular momentum ℓ, where the matrix elements are complex with unit modulus $|U_\ell| = 1$, and only the phase of the outgoing wave can change.

In the presence of absorptive effects, a complex potential can be used to describe elastic scattering, where now $|U_\ell| < 1$, and 2.22 no longer applies. A change in the modulus of U_ℓ is a change in amplitude of the outgoing wave, and a change in the argument of U_ℓ means there is a change in phase. The reaction cross section is expressed as:

$$\sigma_r = \sum_{\ell=0}^{\infty} \frac{\pi}{k^2}(2\ell+1)(1-|U_\ell|^2) \tag{2.23}$$

The collision matrix which details different reaction channels, $|U_{cc'}| < 1$, is not a diagonal matrix. The diagonal elements still represent the elastic scattering channel, but now the off diagonal elements represent the non-elastic processes, i.e. reactions.

2.1.4 Description of the R-matrix Formalism

The previous section showed how cross sections can be described in terms of the collision matrix, U_ℓ. If the wave functions and the potential that describe the nuclear system before and after a reaction were known, it would be straight forward to determine U_ℓ: the solution to the Schrödinger equation with the appropriate potential would yield the form of the wave function of the nuclear system, this would enable a determination of U_ℓ, and thus a determination of the theoretical cross section.

However, the strong nuclear force is not very well understood and the nuclear potential for a CN is extremely complex. This being the case, it is not possible to know the exact form of the potential for the CN system and therefore not possible to know the exact wave-function.

This is where R-matrix (aka scattering or collision theory) theory comes in. R-matrix theory was first introduced in 1957 by Wigner and Eisenbud [33], and was

put in its standard form with the 1965 review article by Lane and Thomas [34]. This section will simply provide a description of the main features of the theory, for a full treatment see [34] and [35].

What R-matrix theory does is to provide the relation between the collision matrix and the R-matrix, which contains the properties of the eigenstates of the CN, that is, the levels resonances. The resonance structure that is seen in CN formation is itself complex. Theory can not be turned to determine at what energies resonances will form, nor any other information about the resonances. It is therefore necessary to perform an experiment from which resonance parameters can be extracted from the resulting data. This can be achieved with an R-matrix code such as SAMMY, which is discussed in Section 2.2.4. Having extracted the resonance parameters, in effect the R-matrix, it is then possible to obtain values for the collision matrix, and therefore obtain a cross section.

There are four key assumptions to the theory:

1. Non-relativistic quantum mechanics is applicable

2. All processes that result in the formation of more then two reaction products are considered absent or unimportant

3. Processes that involve creation or destruction are considered absent or unimportant

4. For any pair of nuclei, there exists a radial distance called the channel radius, beyond which, for neutrons, neither of the particles experience an interaction potential

From the second assumption, what is considered is an ingoing wave function which describes the two incident particles and an outgoing wave function describing the two reaction products. For example, in the current work this means an incoming neutron and a ^{236}U target nucleus, and an outgoing γ-ray and a ^{237}U nucleus for a capture reaction, or outgoing ^{236}U nucleus and an elastically scattered neutron. The initial configuration of a neutron and ^{236}U nucleus, and a the final configuration of a ^{237}U nucleus and a γ-ray are referred to as channels. These are respectively termed the entrance channel c, and the exit channel c'. These channels are described as follows:

$$c = \{\alpha, \ell, j, J, m_J\} \tag{2.24}$$

$$c' = \{\alpha', \ell', j', J', m'_J\} \tag{2.25}$$

Where α is the internal excitation energy of the binary pair, ℓ is their relative angular momentum, j is the channel spin, J is the total angular momentum, and m_J is the projection of J. What channels are available to form a CN is constrained by the conservation of angular momentum and parity.

From the fourth assumption, as the nuclear potential and the CN wave function is not known, to deal with the CN, the idea is to break the configuration space into two regions: and internal and external region (see Figure 2.3).

In the external region, there is no nuclear potential with which the incident and outgoing particles interact. In the case of an incident neutron there is no coulomb potential to be considered and thus they can be treated as free particles for which the wave functions are known.

In the internal region the nuclear force is present, and the wave function representing the compound nucleus is extremely complicated, yet it it can however be expanded in terms of its eigenstates without explicitly solving the Schrödinger equation for the system. The point in space where these two regions meet is called the channel radius, a_c, which is expressed as:

$$a_c = 0.8 + 1.23 \cdot A^{1/3}\ fm \tag{2.26}$$

Thus the incoming wave function is comprised of a neutron and target nucleus treated as free particles, the CN is treated as a single system that has discrete energy levels, and the outgoing wave function is again comprised of a two particles. From above, it is not necessary to have the exact wave function in the internal region. But from the basic tenets of quantum mechanics, the wave functions of the incoming and outgoing particles, and their derivatives, in the external region must match those of the wave function of the compound nucleus, in the internal region, at the channel radius. The result of this is that it is then possible to parametrize the reaction cross section in terms of the properties of the eigenstates of the compound nucleus.

The description of a cross section solely in terms of the properties of the excitation levels of the CN also serves as the biggest limitation of R-matrix theory: the

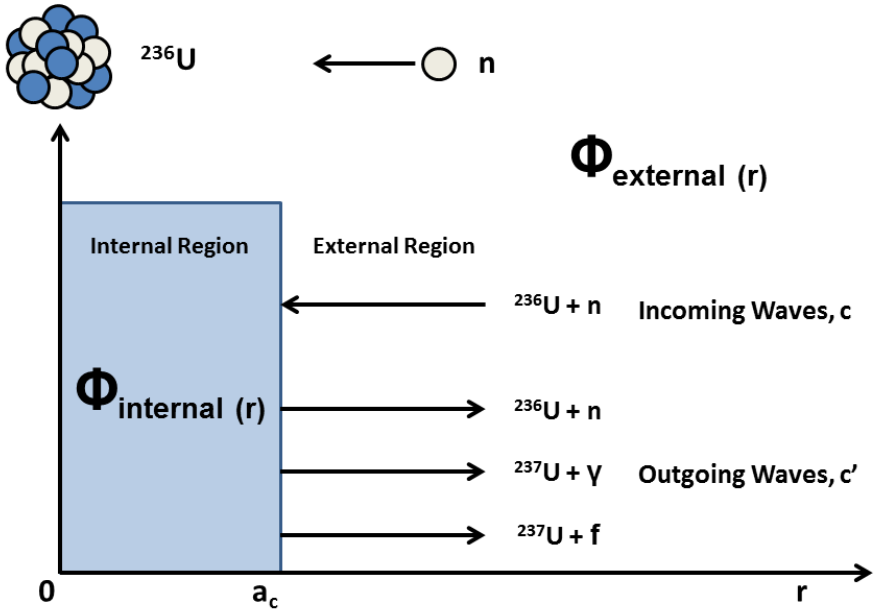

Figure 2.3: A depiction of the configuration space in terms of an internal and external region. Outside the channel radius a_c the potential is zero and the neutron and target are treated as free particles. Inside the channel radius the wave function of the CN system is not known. At a_c the boundary conditions mean the wave functions of the external region match that of the internal region, which can be expressed in terms of its eigenstates.

compound nucleus is treated as if it were a black box, and in obtaining the reaction cross sections, no information about the forces inside the nucleus can be determined.

Similar to Section 2.1.3, the cross section for a given reaction is expressed as:

$$\sigma_{cc'} = \pi\lambda^2 g_J |\delta_{cc'} - U_{cc'}|^2 \tag{2.27}$$

Where $|U_{cc'}|^2$ represents the probability of a transition from c to c', g_J is the statistical spin factor, which describes the probability of reaching a final spin J in the CN given the initial spins i and I of the neutron and target nucleus respectively, and is expressed as:

$$g_J = \frac{2J+1}{(2i+1)(2I+1)} \tag{2.28}$$

Elastic scattering is described if $c = c'$, resulting, for a given value of J, the cross section as:

$$\sigma_{cc} = \pi\lambda^2 g_J |1 - U_{cc}|^2 \tag{2.29}$$

Where for any other reaction a sum over all exit channels except c gives the reaction cross section:

$$\sigma_{cr} = \pi \lambda\!\!\!^{-2} g_J (1 - |U_{cc}|^2) \tag{2.30}$$

This can be generalised for capture reactions to include all possible channels and all possible J:

$$\sigma_{capture} = \pi \lambda\!\!\!^{-2} \sum_J g_J \sum_c \left(1 - \sum_{c'} |U_{cc}|^2 \right) \tag{2.31}$$

where c' represents all channels except capture.

R-matrix theory expresses the collision matrix in terms of the R-matrix in the following manner:

$$U_{cc'} = e^{-i(\phi_c + \phi_{c'})} \{ \delta_{cc'} + 2iP_c^{1/2} [(1 - R_{cc'} L^o_{cc'})^{-1} R_{cc'}] P_{c'}^{1/2} \} \tag{2.32}$$

This equation contains the R-matrix $R_{cc'}$ and a matrix $L^o_{cc'}$, where

$$R_{cc'} = \sum_r \frac{\gamma_{rc} \gamma_{rc'}}{E_r - E} \tag{2.33}$$

$$L^o_{cc'} = (S_c + iP_c - B_c) \delta_{cc'} \tag{2.34}$$

There are many terms in these equation which are defined as follows, where the indice r corresponds to a given energy level or resonance:

- ϕ_c are the potential scattering phase shifts
- γ_{rc} and $\gamma_{rc'}$ are the reduced width amplitudes at the resonance energy, E_R
- S_c and P_c are the shift and penetrability factors, which are defined as the real and imaginary parts of the outgoing wave function at the channel radii
- B_c represents the boundary conditions at the channel radii

2.1.4.1 Approximations To The R-Matrix

The formalism of R-Matrix theory is mathematically rigorous and well understood, but in practice it is difficult to solve the equations exactly, due to the large size of

the matrices discussed above, and thus approximations are necessary. The main approximations are the Single-Level Breit-Wigner (SLBW), Multi-Level Breit-Wigner (MLBW), and the Reich-Moore approximation.

Section 2.1.2 described resonances in terms of unbound levels in the compound nucleus. The shape of isolated resonances are well approximated by the Breit-Wigner formula, proposed in 1936 in describing slow neutron capture [36]. This has the basic form:

$$\sigma_{cc'} = \pi\lambda\!\!\!^{-2} g_J \frac{\Gamma_{rc}\Gamma_{rc'}}{(E-E_r)^2 - \frac{\Gamma_r^2}{4}} \tag{2.35}$$

Where $\lambda\!\!\!^{-}$ is the reduced de Broglie wavelength, Γ_{rc} and $\Gamma_{rc'}$ partial widths, and Γ_r is the total width.

In the SLBW, the assumption is made that there is no interference between different resonances or channels, and thus only one level need be considered, simplifying Equation 2.32, reducing it to the form below.

$$U_{cc'} = e^{-i(\phi_c+\phi_{c'})}\left(\delta_{cc'} + \frac{i\sqrt{\Gamma_{rc}\Gamma_{rc'}}}{E_r - E - i\Gamma_r/2}\right) \tag{2.36}$$

The expression for a neutron induced cross section for a single, isolated resonances in the SLBW is given as:

$$\sigma_c(E) = \pi\lambda\!\!\!^{-2} g_J \left(4\cdot sin^2(\delta) + \frac{\Gamma_{rc}\Gamma_r}{(E_r-E)^2 + \frac{\Gamma_r^2}{4}} + 4\frac{\Gamma_{rc}(E_r-E)}{(E_r-E)^2+\frac{\Gamma_r^2}{4}}\right) \tag{2.37}$$

Which shows the total cross section to be a sum of three terms: the potential scattering term (seen in Section 2.1.3), a resonant term, and a term describing the interference between potential and resonant scattering. When the last term is negative, just below the resonance, the resonant scattering cross section has a "destructive" term which gives scattering resonances their usual asymmetric shape.

The MLBW accounts for interference between energy levels, but not channels, which is is achieved by summing over the individual levels:

$$U_c = e^{-i(\phi_c+\phi_{c'})}\left(\delta_{cc'} + \sum_r \left(\frac{i\sqrt{\Gamma_{rc}\Gamma_{rc'}}}{E_r - E - i\Gamma_r/2}\right)\right) \tag{2.38}$$

Of particular difficulty is the inversion of the $(1-R_{cc'}L^o_{cc'})$ term in 2.32. In heavy nuclei there are a huge number of photon channels, running into the hundreds of

thousands. The Reich-Moore approximation excluded these photon channels, hugely reducing the number to be considered resulting in a reduced R-matrix. This then allows for the matrix inversion above to be achieved and the collision matrix to be calculated. This approximation is the most accurate in use, and is the one used in SAMMY (see Section 2.2.4).

2.2 Cross Sections Measurements

This section will discuss the nature of the time-of-flight technique for cross section measurements, specifically for transmission and capture. The current work deals only with the measurement of the capture reaction, however to completely characterise the neutron capture cross section, it would be necessary to combine data from a capture measurement with that of a transmission, i.e. total cross section, experiment. To that end, transmission experiments are briefly discussed in the relevant sections below. Doppler and resolution broadening which affect the experimentally measured resonances are then described before finally looking to resonance kernels, which the current work aims to determine.

2.2.1 Time Of Flight

A direct relation exists between the time it takes a neutron to traverse a given distance (corresponding to a flight path), and its kinetic energy. This relation is the basis of the TOF technique. Figure 2.4 shows a typical situation. A pulsed neutron source produces neutrons at a time t_0 which then travel along a flight path of length L, before undergoing reactions which are detected at a time t_{det}.

It is known from relativity theory that the total energy E_{tot} possessed by a body is given by $E_{total} = mc^2$, where m is the effective mass of a particle and c is the speed of light. This expression is the sum of the kinetic and the mass energy. Considering a neutron with kinetic energy E_n and rest mass m_0, this becomes:

$$mc^2 = E_n + m_0c^2 \tag{2.39}$$

Introducing the Lorentz factor γ, where $\gamma = (1 - v^2/c^2)^{1/2}$ this expression can be rearranged for E_n as:

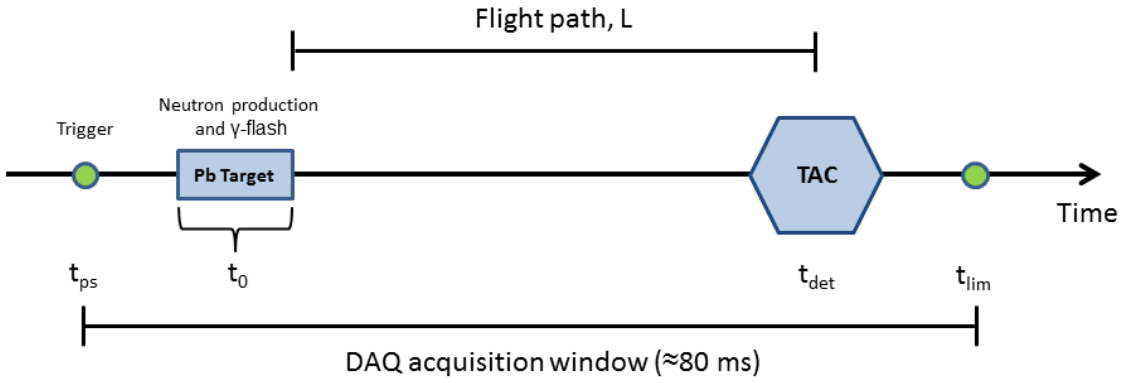

Figure 2.4: A typical set up for a time of flight experiment. The figure shows the neutron production time at some point in the spallation target at t_0, and the detection time of the secondary particles at time t_{det} after the the neutrons have travelled along a flight path of length L. A signal from the PS is sent which triggers the DAQ which records events until a time t_{lim}. This occurs every time the PS sends a proton pulse to the n_TOF facility.

$$E_n = m_0 \cdot c^2 \left(\frac{1}{\sqrt{1 - \frac{v^2}{c^2}}} - 1 \right) \tag{2.40}$$

Performing a binomial expansion on γ gives us the series:

$$1 + \frac{1}{2}\frac{v^2}{c^2} + \frac{3}{8}\frac{v^4}{c^4} + \frac{5}{16}\frac{v^6}{c^6} + \dots \tag{2.41}$$

Which upon substituting into Equation 2.40 gives:

$$E_n = \frac{1}{2}m_0 v^2 + \frac{3}{8}m_0\frac{v^4}{c^2} + \frac{5}{16}m_0\frac{v^6}{c^4} \tag{2.42}$$

Where the first term in the series is the classical expression for kinetic energy. The energies in the current work are below that which requires a relativistic treatment, and the first order expansion suffices. Writing the velocity in terms of distance over time, this yields:

$$E_n = \frac{1}{2}m_0 \left(\frac{L}{t}\right)^2 \tag{2.43}$$

Then expressing m_0 in MeV/c^2, L, the length of the flight path L in m, and the neutron time of flight t in μs, the non-relativistic expression is arrived at:

$$E_n(eV) = \left(\frac{72.29 \cdot L(m)}{t_{det}(\mu s) - t_0(\mu s)} \right)^2 \tag{2.44}$$

In the denominator, the time of flight is shown as $t_{det}(\mu s) - t_0(\mu s)$, where t_{det} is the time the γ cascade is detected, and t_0 is the time the neutron spends in the spallation target before emerging

The uncertainty in the measurement of the neutron energy depends of the uncertainty in the flight path, the time resolution of the detector, and the resolution function, which is related to the neutron production mechanism and is characteristic of the set-up of the experimental facility. The resolution function is discussed in Section 3.1.5.

2.2.2 Cross Section Measurements

In determining either the total cross section or one of the partial cross sections, different experimental techniques are employed. These are discussed briefly below with how the theoretical and experimental values are determined.

2.2.2.1 Total Cross Sections

The total cross section is related to the probability that any reaction will occur. This can be determined by measuring how much incident flux is lost after a beam passes through a target, which is known as a transmission experiment. A neutron detector is placed at the end of a neutron beam line and measurements are made with the target in the beam path and removed from the beam path.

A neutron beam with flux ϕ passing through a target with particle density N $(particles\,cm^{-3})$, total cross section $\sigma_t\,(cm^2)$ and thickness $\mathrm{d}x\,(cm)$ will experience a reduction in flux, $\mathrm{d}\phi$ $(particles\,m^{-2}s^{-1})$, of:

$$-\mathrm{d}\phi = \phi \cdot N \cdot \sigma_t \cdot \mathrm{d}x \tag{2.45}$$

Integrating over the target thickness and rearranging gives:

$$\frac{\phi_{out}}{\phi_{in}} = e^{-N\sigma_t \cdot dx} = e^{-n\sigma_t} = T(E_n) \tag{2.46}$$

Where $N \cdot dx$ has been written as the areal or surface density n $(particles\,m^{-2})$. The proportion that undergoes no reaction is said to have been transmitted through the sample and thus the ratio of the flux before and after the target is the neutron transmission coefficient, $T(E_n)$. Experimentally this is determined as:

$$T(E_n) = N \cdot \frac{C_{In}(E_n) - B_{In}(E_n)}{C_{Out}(E_n) - B_{Out}(E_n)} \tag{2.47}$$

Where $C_{In}(E_n)$ is the number of detected neutrons when the sample is in and $B_{In}(E_n)$ is the number of background counts, and $C_{Out}(E_n)$ and $B_{Out}(E_n)$ are the same for the case where the sample is removed from the beam line. N is a normalisation factor that accounts for different beam intensities used for in and out measurements.

2.2.2.2 Partial Cross Sections

It is via the detection of secondary particles, i.e. the reaction products, that are emitted following a neutron induced reaction that allows the determination of a partial cross section. From the previous section, it is clear that if $e^{-n\sigma_t}$ is the fraction of neutrons passing though the sample, then the fraction of neutrons undergoing a reaction is just $1 - e^{-n\sigma_t}$. Then the proportion of events related to the reaction of interest is given by the ratio of the partial cross section σ_x (for a capture reaction $x = \gamma$), to the total cross section. This gives rise to the yield, $Y(E_n)$, defined as the proportion of neutrons undergoing the reaction of interest. The link between these quantities is expressed by the theoretical reaction yield as:

$$Y_x(E_n) = \left(1 - e^{-n \cdot \sigma_t(E_n)}\right) \cdot \frac{\sigma_x(E_n)}{\sigma_t(E_n)} \tag{2.48}$$

An approximation to Equation 2.48 arises for thin targets where $n\sigma_t$ is very small. In this case $e^{-n \cdot \sigma_t}$ approaches zero and can be expanded about zero to give $1 - n\sigma_t$ giving:

$$Y_x \approx n\sigma_x \tag{2.49}$$

For thicker targets there is a non-negligible probability that a neutron will scatter one or more times, and be captured at a later time. Thus the yield will then be a sum of contributions higher order terms, where Equation 2.48 gives the zeroth order term, Y_0. In this case the yield will be:

$$Y_x = Y_0 + Y_1 + Y_2 + \ldots + Y_n \tag{2.50}$$

where the Y_1 and higher terms are due to capture after multiple scattering.

The experimental yield is obtained by measuring the count rate of neutron induced reactions and the associated background. Formally it it given by:

$$Y_x(E_n) = \frac{C(E_n) - B(E_n)}{N_{BIF} \cdot \varepsilon \cdot \phi(E_n)} \tag{2.51}$$

Where $C(E_n)$ and $B(E_n)$ are the overall and background count rate respectively, ε is the detector efficiency, $\phi(E_n)$ is the neutron flux, and N_{BIF} is the fraction of the beam intercepted by the sample (=1 when the sample is larger than the beam). The current work is concerned with the determination of the yield via this expression.

2.2.3 Capture Kernels

The resonance parameters of the R-Matrix formalism for describing each resonance can be extracted from analysis of observable quantities in cross section measurements. To achieve this, it is very important to understand the relation between experimental observables, such as σ, $Y(E_n)$ and $T(E_n)$, and the resonance parameters, which are the energy (E_R) and spin (J) of the corresponding unbound state of the CN, and the widths (Γ_x) corresponding to each open reaction channel. One method for achieving this is the area analysis technique. While the value of the resonance parameters are highly effected by the broadening effects, the integral of the resonances is unaffected and thus is a very accurate measure of the cross section. Further details are available in [37]. For transmission and partial cross section measurements, the area for each isolated resonance is expressed as:

$$A_t = \int (1 - T(E_n))\,\mathrm{d}E_n \tag{2.52}$$

$$A_x = \int \sigma_x(E_n)\,\mathrm{d}E_n \tag{2.53}$$

Where A_t and A_x are the resonance areas obtained from transmission and partial cross section measurements respectively. Performing the necessary integrals after substituting the earlier expressions for $Y(E_n)$ and $T(E_n)$, and using the SLBW cross section formula for the peak cross section at $E = E_R$, and further assuming that potential scattering and broadening effects can be ignored gives rise to the expressions:

$$A_t = 2\pi^2 \lambda_R^2 g_J \Gamma_n \tag{2.54}$$

$$A_x = 2\pi^2 \lambda_R^2 g_J \frac{\Gamma_n \Gamma_\gamma}{\Gamma_n + \Gamma_\gamma} \tag{2.55}$$

Where λ_R is the reduced de Broglie wavelength at the resonance energy E_R.

Looking to partial cross section measurements, knowing the area A_x and λ_R allows a calculation of the radiative kernel RK where:

$$RK = g_J \frac{\Gamma_n \Gamma_\gamma}{\Gamma_n + \Gamma_\gamma} \tag{2.56}$$

For the particular case in which scattering strongly dominates over capture ($\Gamma_n \gg \Gamma_\gamma$) and vice versa ($\Gamma_\gamma \gg \Gamma_n$), then $\Gamma \approx \Gamma_n$ or $\Gamma \approx \Gamma_\gamma$ respectively. Equation 2.56 can thus be approximated by:

$$RK \approx g_J \Gamma_x \qquad \text{For when } \Gamma_\mathrm{x} \gg \Gamma_\mathrm{n} \tag{2.57}$$

$$RK \approx g_J \Gamma_\gamma \qquad \text{For when } \Gamma_\mathrm{n} \gg \Gamma_\gamma \tag{2.58}$$

For actinides, it is usually the case for most resonances that $\Gamma_\gamma \gg \Gamma_n$, however the current work, being a capture experiment, will be reporting on the RK values as it not always the case that the partial widths can be confidently reported. As Equation 2.56 is one equation consisting of two unknowns, and thus infinite solutions, to extract all the resonance parameters needed for a cross section determination, a complimentary transmission experiment would need to be performed as this gives the information on the value of Γ_n. The combination of the data from these two experiments allows the determination of both Γ_γ and Γ_n.

Another method for determining resonance parameters is resonance shape analysis (RSA). For an experiment with high statistics and good resolution, calculating the resonance parameters (E_R, J, Γ_γ, etc) using fitting procedures is more accurate. This can be achieved with an R-matrix code such as SAMMY which uses the Bayesian approach to fit the best resonance parameters that allows the reproduction of the measured shape of each resonance. As one needs to reproduce the shape of the resonances, SAMMY takes into account all the experiment effects that affect the resonance shape such as multiple scattering, as well as the Doppler and resolution broadening.

2.2.4 R-Matrix Code SAMMY

The SAMMY code was developed by N. Larson at the Oak Ridge National Laboratory ORNL (USA) [38] in order to use R-matrix theory to analyse time of flight data, in both the RRR and URR, for both neutrons and charged particles. It allows for a choice of R-matrix approximations, can account for multiple scattering and

self-shielding in the sample, and can deal with Doppler broadening with either the free gas model (FGM), which was used in the current work, or the crystal lattice model (CLM). Impurities in the sample can also be accounted for.

A comprehensive guide to both the R-matrix theory and the full details of the SAMMY code itself can be found in [39], thus this section will only briefly outline the main features of the SAMMY code.

SAMMY makes use of Bayes' Theorem in order to find the best fit values for the parameters that define a resonance. In the RRR, SAMMY uses the chosen R-Matrix approximation in order to achieve this, whereas the URR is handled in SAMMY through use of the FITACS module to calculate and fit average cross sections. However, the current work only deals with the RRR.

To run SAMMY requires three files: an input file, a parameter file, and a data file. The input file contains all the information regarding the sample, temperature, flight path, form of Doppler broadening correction (e.g. FGM or CLM), resolution function, and R-matrix approximation to be used, etc. The parameter file contains the initial values for the resonances, possible taken from an existing library, namely the resonance energy, capture width, neutron width, fission width. Values for the normalisation and background can also be set here, along with their associated uncertainties. All of these parameters can be left free to vary or fixed in order to obtain the best fit. In the case of the current work, the normalisation and background are determined and then fixed before the analysis proper proceeds, the details of these being found in Sections 4.6 and 4.6.1 respectively. Finally the data file contains the experimental data which SAMMY is to fit. This is composed of a list of the energy, yield or cross section, and statistical error for every point. The current work performed fits on yield data.

After running the SAMMY code, SAMMY outputs a new parameter file containing the new best fit values. This new parameter file can then be used as input for a subsequent run. The results are also outputted in ENDF format allowing for their inclusion in evaluated nuclear data files.

Chapter 3

Experimental Set-Up

This chapter will describe all the relevant features of the neutron time-of-flight facility (n_TOF) at CERN where the current work was carried out. Beginning with a description of the source of the proton beam that drives the n_TOF experiment, this chapter will then discuss the features of the n_TOF facility itself, from the characteristics of the neutron beam to the data acquisition system (DAQ). Following this will be a discussion of the detectors used in both the current work, and that of a complementary experiment also performed at n_TOF with the same sample, but a different detector and analysis technique. The discussion will end with a description of the ^{236}U and auxiliary samples used in the current work to enable a successful experimental run.

3.1 The n_TOF Facility At CERN

The n_TOF project began operation in 2002 following the proposal by Carlos Rubbia *et al* [40]. In its twelve year history it has seen the completion of two experimental campaigns (named Phase-1 and Phase-2), a four year shut down to replace the lead spallation target, and the construction of a second experimental area - Experimental ARea 2 (EAR-2) which began operation in July of 2014, in what marked the beginning of the third experimental campaign (Phase-3). Phase-1 and 2 have resulted in a large number of successful measurements on myriad nuclei for a wide range of applications, making a wealth of nuclear data available for evaluators.

In the subsections that follow, an outline will be given of all the major features of the facility: from the source of the neutrons, the beam line they follow to the experimental area where the target is housed, the detector that records the signals

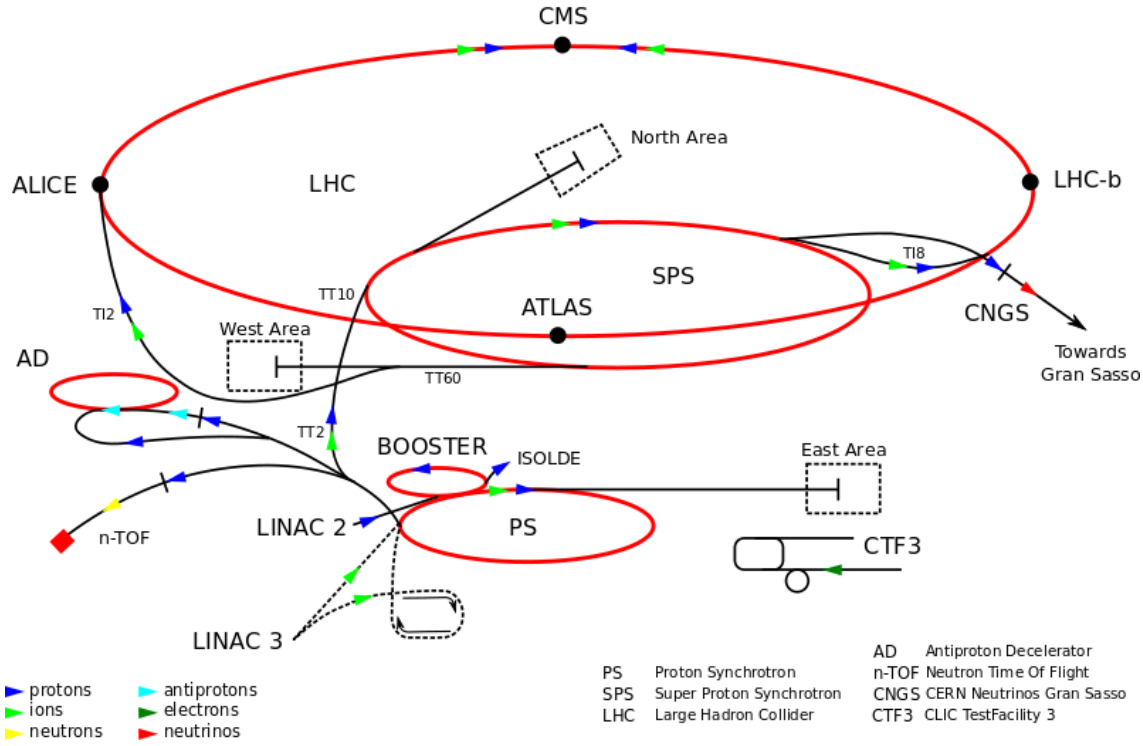

Figure 3.1: The accelerator complex at CERN.

generated by the reactions under investigation, to the data acquisition system (DAQ) that records these signals. First however, it is prudent to start at the beginning, and look at where the protons that drive all the experiments at CERN come from.

3.1.1 The CERN Accelerator Complex

The accelerator complex at CERN is a combination of LINear ACcelerators (LINACs) [41] and ever more powerful synchrotrons, as can be seen in Figure 3.1. Protons are accelerated up to an energy of 50 MeV in LINAC2 before being injected into the proton-synchrotron booster (PSB). Here they are accelerated up to an energy of 1.4 GeV before being passed into the proton synchrotron (PS), where protons are accelerated up to a maximum of energy 25 GeV. It is from the PS that n_TOF takes beam, with an energy of 20 GeV. Rather then being a continuous beam, the protons are injected into the accelerator complex where the accelerators bunch the beam making it a pulsed proton source.

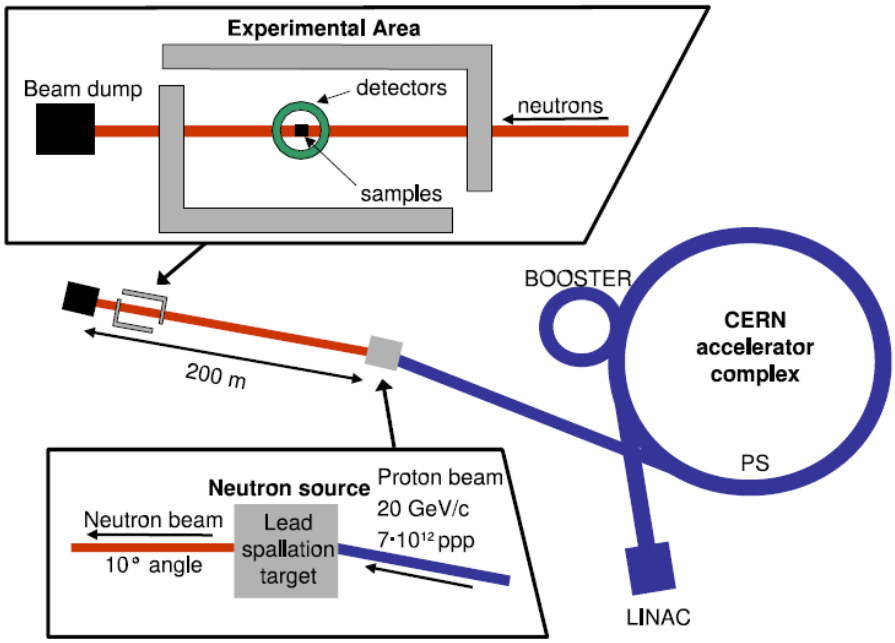

Figure 3.2: The CERN n_TOF facility.

3.1.2 The n_TOF Facility

The proton bunches, having been accelerated to 20 GeV in the PS, are then sent off to the n_TOF facility. An important part of the operation of the n_TOF facility is the low duty factor, with the proton pulses arriving on average once every 2.4 seconds. Compared to other facilities which provide a similar average flux in terms of neutrons/s, the relatively low duty factor means the n_TOF facility provides a much higher flux per pulse. The n_TOF facility receives just a fraction of all the bunches in the PS, with the rest being sent on to the SPS and beyond, within the chain of accelerators. Figure 3.2 shows a schematic of the n_TOF facility, and full description is provided in [42].

Travelling towards the n_TOF beam line, a proton pulse will first come into contact with the PKUP (PicK UP) detector, which is simply a wall current monitor which registers the intensity of the proton pulse. The proton pulse will then hit the lead spallation target. Upon striking the lead target, the proton pulse, with an average intensity of 7×10^{12} protons per pulse (ppp), induces spallation, fission-evaporation and knock-out reactions. On average, every incident proton results in ≈ 400 neutrons being produced.

The proton pulse strikes the spallation target at an angle of 10° to the beam line to reduce the highly energetic particles produced mainly in the forward (0°) direction.

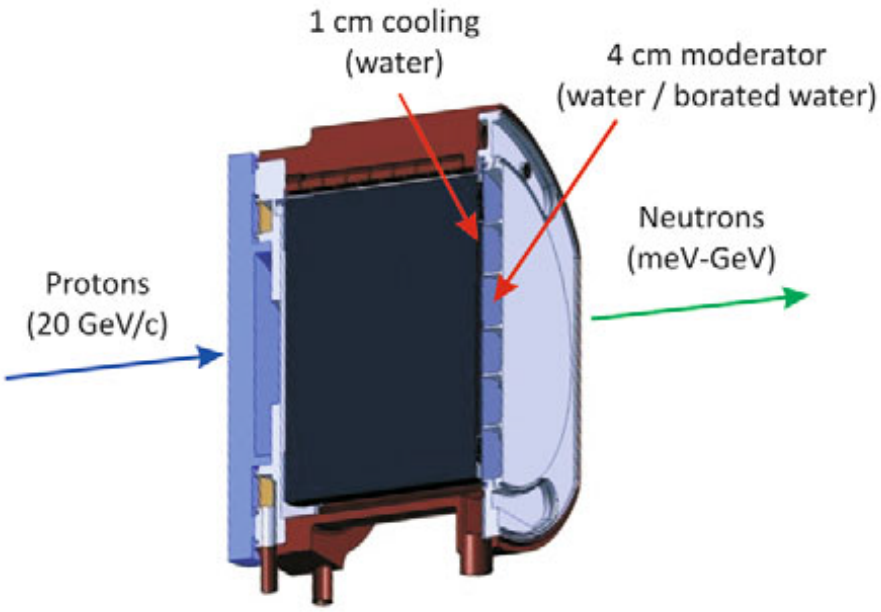

Figure 3.3: The n_TOF lead spallation target, showing also the coolant and moderator circuits.

Part of these still arrive in the experimental area and compose the so-called γ-flash, which is discussed in Section 3.2.2. The cylindrical spallation target itself has a diameter of 60 cm and a 40 cm length and weighs 1.3 tonnes. It is surrounded by 1 cm of water, which acts as a coolant and moderator for the target, and then in the front face by 4 cm of either water or borated water ($H_2O + 1.28\%$ H_3BO_3) which serves as a further moderator for the initially fast neutron spectrum that is produced. The target, along with the coolant and moderator circuits, is shown in Figure 3.3.

The choice of moderator affects the flux in the thermal region (see Section 3.1.4) and also the intensity and energy distribution of the beam of photons that travels along with the neutron beam. For the current work, borated water was used as the $^{10}B(n, \alpha)$ reaction helps suppress the $^{1}H(n, \gamma)$ reaction, which results in the production of 2.2 MeV γ-rays, a significant source of background.

Following neutron moderation through scattering reactions in lead and, mainly, water and borated water, what emerges from the spallation target is a pulsed white neutron spectrum with energies from meV to GeV, having an isolethargic flux dependence in the epithermal (eV-keV) region [42]. This neutron beam then proceeds 185 meters down a horizontal evacuated beam line, which is shown in Figure 3.4, through to the experimental area, where the samples and detectors are located.

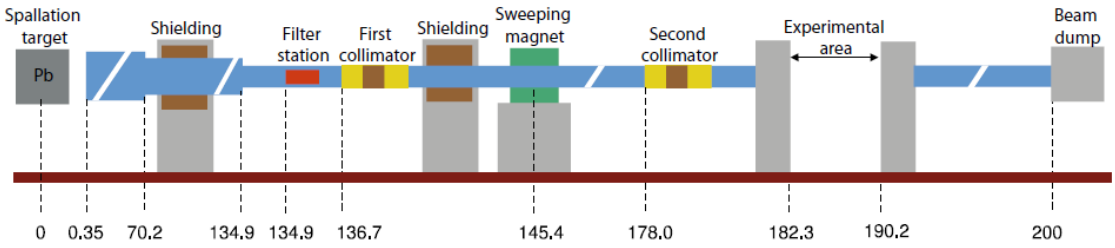

Figure 3.4: The n_TOF beamline. The numbers show the distance from the spallation target in metres.

Along the neutron beam line, a combination of iron shielding and a 3.6 Tesla sweeping magnet eliminates the background due to charged particles, and two collimators help shape the neutron beam. The first collimator has a diameter of 11 cm, and the second collimator, located just before the experimental area, may have one of two diameters: 1.8 cm for capture experiments and 8 cm for fission experiments.

At a distance of 182.3 m from the spallation target is the experimental area. Here the neutron beam encounters a Silicon Monitor detector (SiMon) [43], which serves as a neutron flux monitor, and is active throughout all experiments. SiMon is composed of four silicon detectors placed outside of the beam with a thin ^{6}Li target placed in the beam path. The combination of a 1.5 μm Mylar foil with a thin 200 μg/cm^2 ^{6}Li deposit, results in only a small perturbative effect on the neutron beam. SiMon measures the flux, up to 1 MeV, by detecting the alphas and tritons resulting from the ^{6}Li(n, α)^{3}H reaction. This reaction is considered a standard as the cross section is known to a very high accuracy from thermal to 1 MeV [44].

Also within the experimental area there are various detectors available depending on what experiment is to be performed. For capture measurements, there are the Total Absorption Calorimeter (TAC) (see Section 3.2) and the C_6D_6 deuterated benzene detectors (see Section 3.3). For fission measurements the available detectors are a parallel plate avalanche counter (PPAC) [45] and a micromesh gas detector (MGAS) [46] [47]. Finally, the beam line extends 12 m beyond the experimental area and ends at the beam dump.

For future chapters, it is necessary here to briefly discuss the proton pulses received by the n_TOF facility. For the current experiment, two different intensity pulses were received over the course of a PS super-cycle: a pulse dedicated to the n_TOF facility, with an average intensity of 7×10^{12} ppp and named the TOF pulse, and a parasitic proton pulse called the EAST pulse, with a lower average intensity of 3×10^{12} ppp.

Although of lower intensity, aside from increasing the overall statistics, EAST pulses serve another useful purpose. The high instantaneous flux of neutrons in TOF pulses leads to a high counting rate (and thus pile-up in very strong resonances) and also results in a higher γ-flash, which affects the detector's behaviour at low TOF (i.e. high neutron energy). In cases where pile-up is a problem in the TOF data, and for which corrections to account for these losses may introduce significant uncertainty, it may be possible to use the EAST data in these energy regions, as such pile-up corrections will be smaller and not introduce as much uncertainty.

3.1.3 Neutron Beam Profile

It is not always the case that the dimensions of the neutron beam and those of the sample geometry coincide. Thus it is necessary to know how much of the neutron beam intercepts the target in question. The parameter that defines this is known as the beam interception factor (N_{BIF}), which varies slowly and slightly as a function of neutron energy, and is vital to be able to properly normalise the cross section.

The beam profile was studied over a three year period, with a 2D pixelated micromegas detector with a 5 cm diameter, developed between CERN and CEA [48]. Simulations with the FLUKA code [49] were also performed to determine the beam profile. This detector was located at a position of 183.2 m from the spallation target.

The beam profile is largely determined by the second collimator, which, as mentioned above, has a diameter of 18 mm when in capture mode. It was determined that the shape of the neutron beam is approximately Gaussian, with a FWHM of 3 cm and a standard deviation of 0.7 cm when the 2nd collimator is in capture mode. This is shown for the beam profile in the vertical direction in Figure 3.5, where the points correspond to the measurement and the solid lines to the corresponding FLUKA simulations.

At the position of the TAC, the beam diameter is 4 cm, whereas the diameter of the encapsulated uranium sample is 1 cm. This results in the target seeing approximately 20% of the beam.

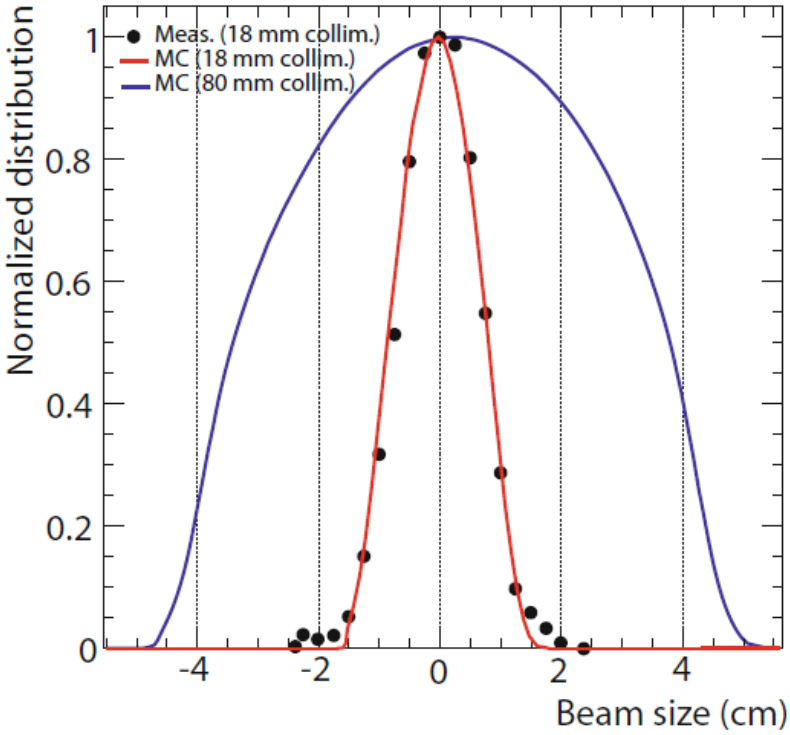

Figure 3.5: Profile of the n_TOF beam, as determined with the pixel-MGAS, for the 2nd collimator in capture mode and fission mode. This is the beam profile in the vertical direction for neutron energies between 0.1 and 1 eV. Image from [42].

3.1.4 Neutron Flux

An accurately determined flux is vital as the error in the flux is often the dominating source of uncertainty in a cross section measurement, and thus the accuracy of cross sections are often related to a precisely known flux. Further, as cross sections are typically determined relative to some well known quantity in a certain energy range, such as a saturated resonance in the case of the current work (see Section 4.6), it is vital to know the neutron energy dependence of the flux. In what follows, the neutron flux is defined as the number of neutrons per proton pulse integrated over the spacial beam profile arriving with a given energy in the experimental area. Full details of the n_TOF flux measurement can be found in [50].

The flux is determined by a comparison between the experimentally determined reaction yield $Y^{ex}_{n,x}$ and the expected theoretical value $Y^{th}_{n,x}$ in measurements where the involved cross sections are considered standard [44] (i.e. known better than 1%) The experimental and theoretical yields are expressed in Equations 3.1 and 3.2 respectively:

$$Y_{n,x}^{ex}(E_n) = \frac{C(E_n) - B(E_n)}{\epsilon(E_n) \cdot \phi(E_n)} \tag{3.1}$$

$$Y_{n,x}^{th}(E_n) = \left(1 - e^{-n \cdot \sigma_t(E_n)}\right) \cdot \frac{\sigma_{n,x}(E_n)}{\sigma_t(E_n)} \tag{3.2}$$

where $C(E)$ and $B(E)$ are respectively the total and background counts received in the detector, and $\epsilon(E_n)$ and $\phi(E_n)$ are the efficiency and the flux, and where n is the areal density and $\sigma_t(E_n)$ and $\sigma_{n,x}(E_n)$ are respectively the total and reaction cross sections. For a thin sample with negligible self-shielding and multiple scattering, Equation 3.2 can be approximated by $Y_{n,x}^{th} = n\sigma_{n,x}$, and equating this with the experimental yield and rearranging for the flux gives:

$$\phi(E_n) = \frac{C(E_n) - B(E_n)}{n \cdot \epsilon(E_n) \cdot \sigma_{n,x}(E_n)} \tag{3.3}$$

At n_TOF, the flux was measured with four different detection systems, namely the SiMON, MGAS, PTB and PPAC detectors, using ^{235}U(n,f), ^{10}B(n, α) and ^{6}Li(n, α) samples in the energy regions where the corresponding cross sections are considered standards [44], and the results from the different measurements combined. Figure 3.6 shows the result of these combined measurements.

Two different moderators were used. As mentioned above these are H_2O and H_2O + 1.28% H_3BO_3, resulting in the two different spectra. In both spectra, clearly visible is the neutron-evaporation peak around 1 MeV, and moving to the lower energies are partially thermalised neutron spectrum. At low energy the spectra show substantial differences. With the H_2O moderator, once thermalised, the neutrons can not lose more energy and so build up at the thermal peak. The ^{10}B in the borated water moderator acts as a strong neutron poison via the ^{10}B(n, α) reactions, substantially reducing the neutron flux in this thermal region.

For the current work, a range of 1 eV to 1.5 keV was covered with use of the borated water moderator. In this energy range, the experimental area received a neutron flux of around 10^5 neutrons per pulse with the collimator in capture mode. In this energy region, it can be seen from Figure 3.6 that the uncertainty ranged from 1-2%.

For radioactive samples where the major source of background comes from the sample itself, a good capture to background ratio can be obtained by having a high instantaneous neutron flux, as offered by the n_TOF facility.

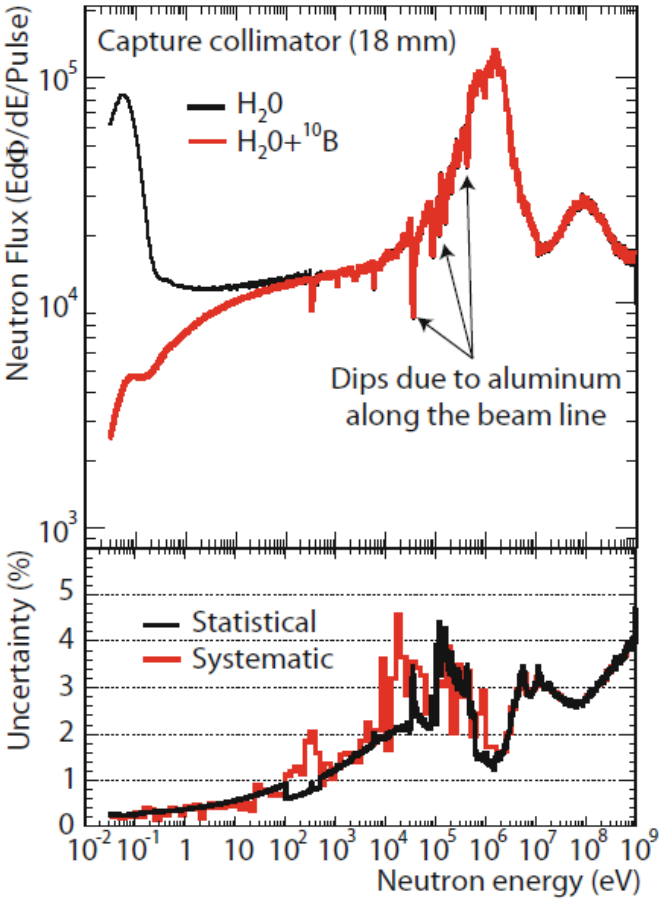

Figure 3.6: The neutron flux at the CERN n_TOF facility.

3.1.5 Energy Resolution

The experimental resolution, $\Delta E/E$ that is observed for resolved resonances is affected by different sources. These are the related to the finite width (7 ns) of the proton pulse from the PS, the uncertainty in the flight path the neutrons traverse (i.e. the energy calibration), the path the neutrons travel through the spallation target (resolution function) and Doppler broadening due to temperature of the sample.

Target nuclei are not static but are instead engaged in thermal motion related to the temperature of the sample. From the point of view of these nuclei, the apparent energy of the neutron will change, as they take relatively more or less time to reach the nucleus, giving a distribution of neutron energies about the true value and reducing the resonance strength. A good approximation to the Doppler broadening is provided by the free gas model (FGM) in which resonances are broadened with a

standard deviation, σ_D, given by:

$$\sigma_D = \sqrt{\frac{2k_BT}{M/m}E_n} \tag{3.4}$$

Where k_b is the Boltzmann constant, T is the temperature, and M and m are the mass of the target and incident particles respectively. This is the dominant source of broadening for neutrons with kinetic energies close to that of the thermal energy of the target nuclei. The current work was undertaken at room temperature, and thus Doppler broadening dominates at low energies.

When the proton pulse enters the spallation target and neutrons are produced, they are moderated as they traverse the target and moderator assembly. Neutrons emerging from this assembly with the same energy will have followed different moderation paths which will affect the observed TOF for one neutron relative to another, making them appear to have greater or lesser neutron energies, or alternatively to have followed longer or shorter flightpaths. This results in the TOF, neutron energy or flightpath having a distribution about a particular energy.

Due to the relationship between neutron energy, TOF and flightpath, as seen in Equation 2.44, this distribution, R, can be expressed in terms of either of these variables and is known as the resolution function:

$$R_E(E_n)\ \mathrm{d}E_n = R_t(t)\ \mathrm{d}t = R_L(L)\ \mathrm{d}L \tag{3.5}$$

Resolution functions are typically determined by Monte Carlo simulations which can then be checked against measurements of well known resonances. The resolution function is usually asymmetric which has the effect of altering the shape of the resonance as well as the time-energy calibration resulting in a shift of the peak energy, as is seen in Figure 3.7.

Thinking of the resolution function as an equivalent moderation length [51], this length can be added to the actual physical length of the flightpath in Equation 2.44 to determine the correct time-energy conversion.

Resolution functions can be parametrised, or more accurately expressed numerically, for use in R-matrix codes such as SAMMY (see section 2.2.4), along with an appropriate Doppler broadening model, to correctly fit resonances. Neither Doppler nor resolution broadening affect the area of the resonance, thus providing the resolution function can be accurately determined, allowing for proper fit to the resonance, the radiative kernel can be calculated.

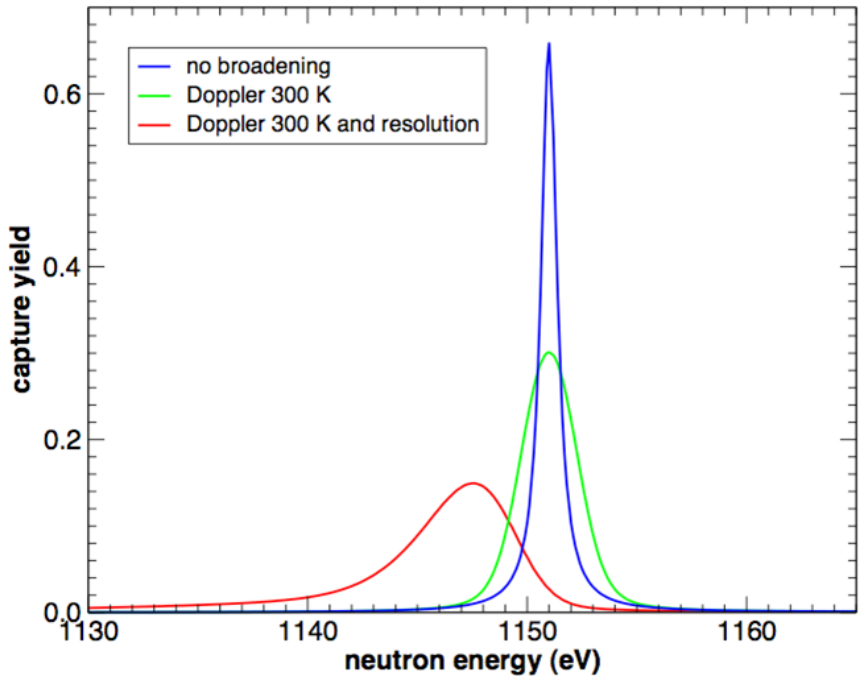

Figure 3.7: Shown is the plot of the true shape of a resonance without any broadening effects. Doppler broadening results in a reduction of the height of the peak whilst maintaining the same area (aka kernel). The effect of the resolution function is it not only broaden the peak further, reducing its strength, it also skews the peak, shifting the erergy at which the resonance appears. Again, the kernel is left unchanged.

The form of the resolution function is directly affected by the physical geometry of the facility, with different facilities having different resolution functions. For the n_TOF facility, resonances can be resolved up to an energy of 20 keV before the broadening is of the order of the level spacing between resonances.

3.2 The Total Absorption Calorimeter (TAC)

As mentioned above, there are two detectors available at the n_TOF facility for undertaking neutron capture experiments. These are the TAC [52] and the C_6D_6 [53] (see Section 3.3). The TAC is a segmented array of 40 BaF_2 crystals, arranged in a spherical geometry, covering 95 % of 4π. The TAC can be seen in Figure 3.8 where the aluminium honeycomb structure housing the crystals is visible. This honeycomb structure is divided into two hemispheres to allow access.

Many of the individual crystals, each of which is coupled to a photomultiplier to form an individual detector module, are visible in the figure. The individual crystals are placed inside 1mm thick ^{10}B (16 % by mass) loaded carbon fibre capsules to

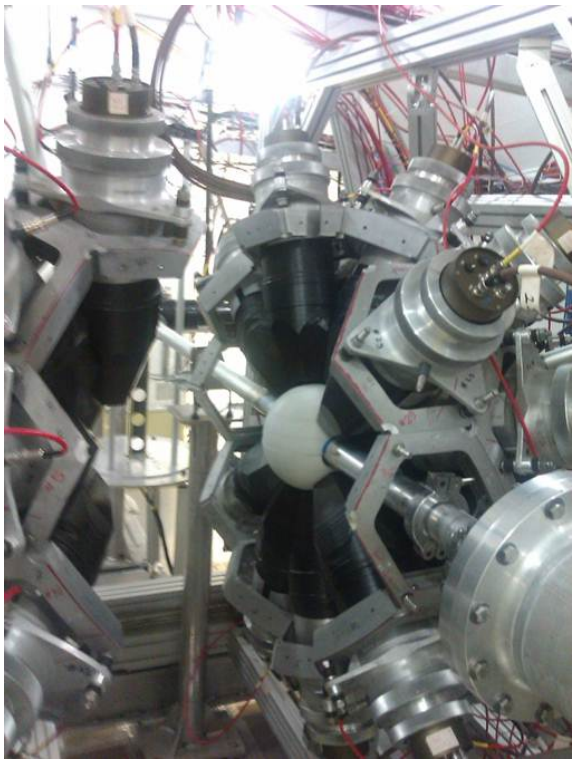

Figure 3.8: The TAC detector with the hemispheres opened to allow access. The white neutron absorber visible at the centre.

reduce neutron sensitivity (the neutrons scattered in the sample are captured in these capsules instead of in the crystals themselves).

Barium has non-negligible capture cross sections for many of its eight naturally occurring isotopes, and neutrons which scatter from the sample and capture on the barium may be mistaken for capture on ^{236}U. This background component is known as the neutron sensitivity and it is desirable to reduce its magnitude as these capture events follow the same energy dependence as the capture events that are under investigation. This is looked at in more detail in section 4.2.2.

The neutron sensitivity is also reduced by the neutron absorber that is visible in the figure as the white sphere at the centre of the TAC. Monte Carlo simulations [54] had shown ^{6}LiH to be the best material for a neutron absorber, not only due to strong neutron capture by the lithium and hydrogen, but also as the material has low Z, it possesses a low γ-ray sensitivity. However, owing to its highly flammable and toxic nature, this is prohibited by CERN's safety regulations. Thus an alternative was necessary, and borated polyethylene was selected.

Signals from the TAC are composed of two parts: a fast component ($\tau_{fast} = 0.7$) ns which is responsible for the good timing characteristics of the TAC, and a slow

component ($\tau_{slow} = 630$) ns due to phosphorescence and delayed fluorescence. The slow component results in one of the limitations of the TAC. When a neutron capture event is registered in the TAC, it is possible that a second event occurs and this signal is sitting on the tail of the slow component of the previous event. This slow component is fitted with a decaying exponential by the PSA routine, which may be unable to discriminate this second signal, giving rise to pile-up.

Another limitation of the TAC is due to radium impurities (^{226}Ra) existing within the BaF_2 crystals, and these are responsible for a large α-background within the TAC. However due to this background not possessing a fast component, it can be identified in the PSA routine.

Having a large solid angle coverage and high efficiency enables the detection of the whole γ-ray cascade. This feature, combined with high segmentation, gives rise to impressive background rejection capabilities, which are discussed in Section 4.

In conclusion, the TAC, possessing a large solid angle coverage, segmented design, high intrinsic efficiency, fast timing, provides the ideal conditions for neutron capture cross section measurements to be performed with high accuracy.

3.2.1 Energy Calibrations And Resolution

Three sources were employed to calibrate the TAC. These calibration sources were ^{137}Cs (661.7 keV), ^{88}Y (898 keV & 1836 keV) and Am/Be (4440 keV), giving four calibration points. Figure 3.9 shows the spectra for each of the three sources for one of the 40 crystals. Also plotted are the fitted backgrounds and the background subtracted spectra. The background subtracted spectra then had Gaussian fits applied to determine the channel number at which the peak occurs.

For each of the 40 crystals the four calibration points are plotted against the energy at which they occur and a polynomial fitted. Figure 3.10 shows first and second order polynomial fits for one crystal. The second order fits were selected and the fit parameters entered into a calibration file.

As a check, the calibrated DST files were processed once more with the calibration file, and the energy calibration checked. The result of this is shown in Figure 3.11. The polynomials were initially fitted with the condition that they were forced through zero, and all the DST's processed as such. A few runs were processed at a later time with the condition that the polynomial was not forced though zero, and this resulted in a better energy calibration for all the sources. However, a change made at CERN to CASTOR resulted in an unforeseen problem that prevented the

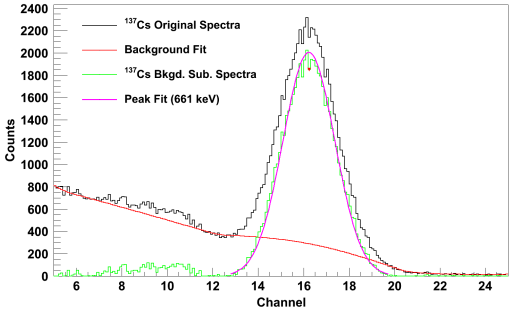

(a) ^{137}Cs spectra.

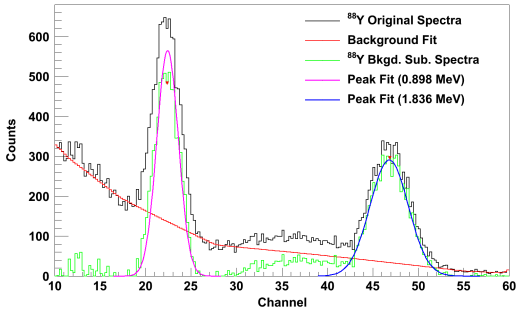

(b) ^{88}Y spectra.

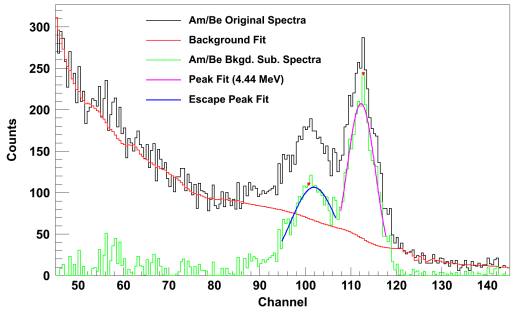

(c) Am/Be spectra. Also shown is a fit to the single escape peak.

Figure 3.9: Original spectra for the three calibration sources used, showing also the fitted background and the background subtracted spectra. Gaussian fits are seen on the background subtracted spectra, the centroids of which gives the channel number at which the peak occurs.

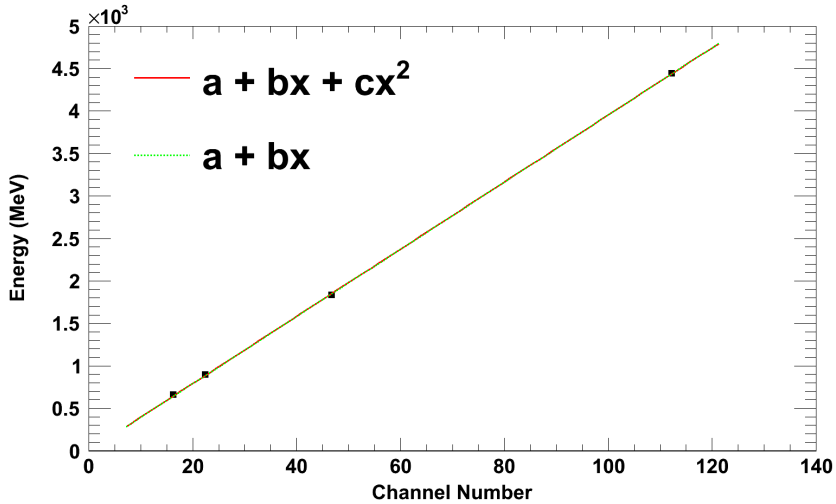

Figure 3.10: A linear and a quadratic fit to the four calibration points from the three calibration samples shown in figures 3.9a to 3.9c.

reprocessing of all data with the better calibration.

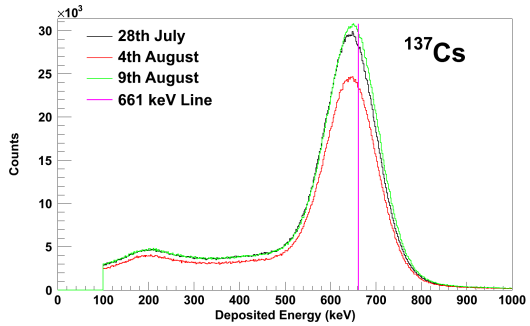

(a) ^{137}Cs calibration.

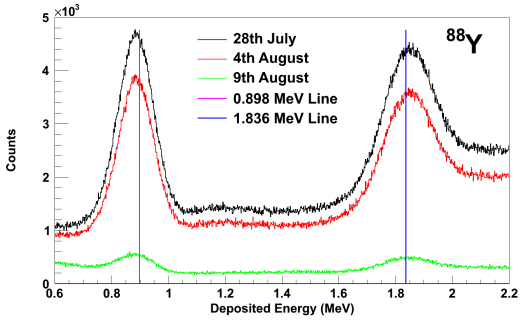

(b) ^{88}Y calibration.

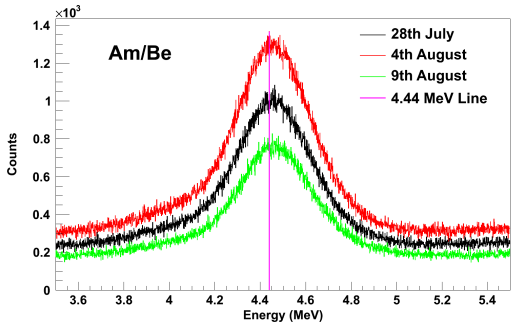

(c) Am/Be calibration.

Figure 3.11: Plots of the three calibration runs performed for each of the calibration sources on different dates throughout the the experimental run. The vertical line shows where the peaks should lie. An offset from the true value is shown (see text for details).

During the current experiment, calibration runs with the three sources were performed at approximately one week intervals in order to account for detector drift. The spectra for all three calibration runs were overlain to highlight, if any, the drift that occurred. Figure 3.12 shows the situation in a single crystal, where no significant drift was observed. Indeed, this was the case for all crystals for each of the calibration sources.

The resolution of the individual TAC modules is shown in Figure 3.13. Here it is seen that the average crystal resolutions are 17% (661.7 eV), 14.2% (898 keV) and 11.6% (1836 keV). Several of the crystals display a resolution considerable worse than the others, in particular crystals 25 and 40. Whereas these may have an impact on the average crystal resolution, the effect on the overall resolution is not significant.

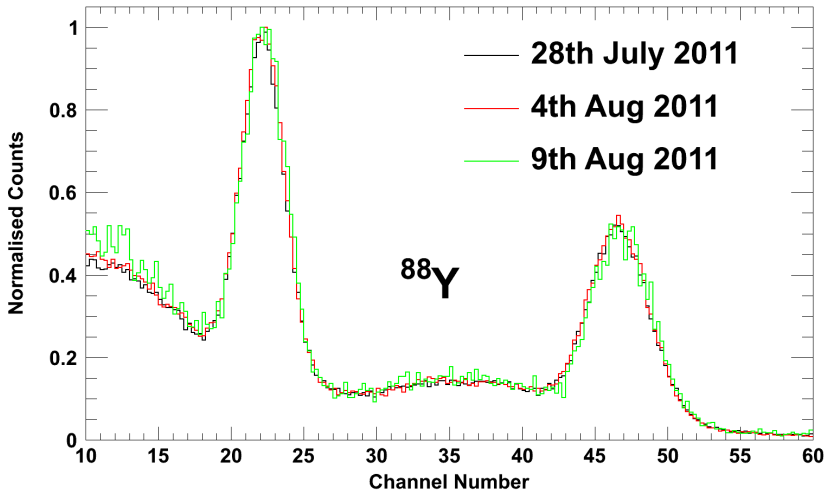

Figure 3.12: Plot of the ^{88}Y spectra for each of the three calibration runs. All spectra were normalised to one for a clearer comparison.

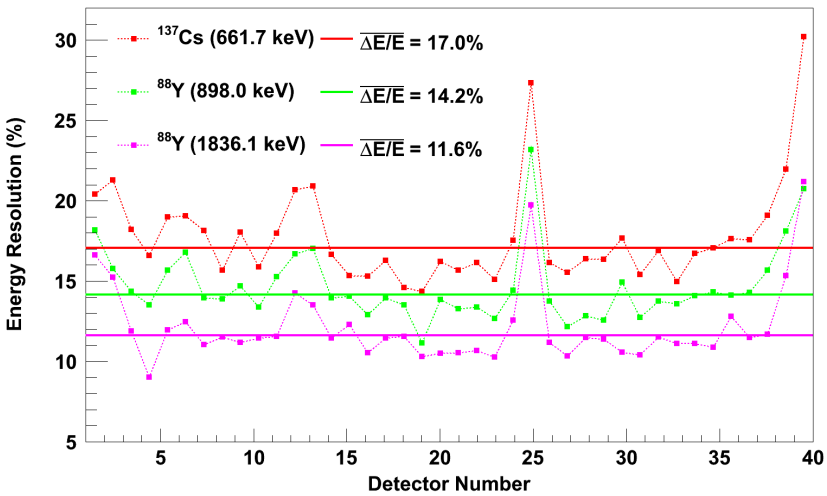

Figure 3.13: The detector resolution, in percentage, plotted for each individual crystal for three calibration peaks. Also shown is the average crystal resolution for each of the peaks.

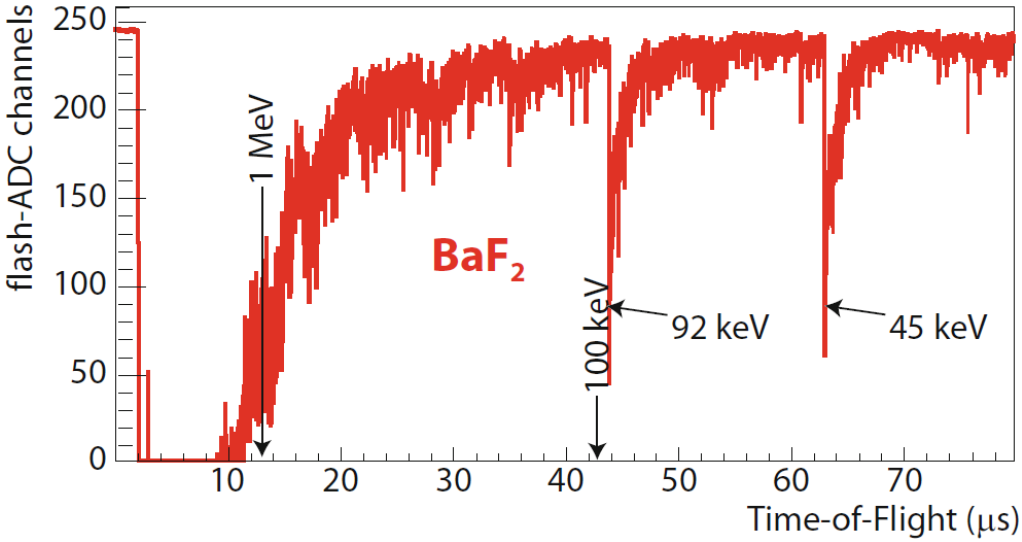

Figure 3.14: The effect of the gamma flash on the TAC. Image from [42].

3.2.2 Effects Of The γ-Flash

The γ-flash refers to not only γ-rays, but also to relativistic charged particles that are created when the proton pulse from the PS interacts with the spallation target. The size of this flash depends on the intensity of the proton pulse. After its creation, the γ-flash takes of the order of 600 ns to traverse the flight path to the experimental area where it interacts with a detector. Upon doing so, it floods the electronics and different detectors respond in different ways in the time they need to recover to the baseline and signals of interest can be recorded.

In the case of the TAC, being a large scintillator detector, it is very sensitive to the γ-flash. As seen in Figure 3.14, the first neutrons to be seen appear around 40 μs corresponding to a upper energy limit of 100 keV.

Beyond 10 keV, the effects of the γ-flash are evident from the way the TOF and EAST pulses deviate from one another. After this point, the TOF data would suffer from more uncertainty due to the γ-flash due to having a higher intensity pulse. This does not mean that where the TOF and EAST data deviate they are free from the effects of the γ-flash, and so care has to be taken when analysing the data. Over the range of interest in the current work, from 1-1500 eV, the γ-flash poses no problem, and the main concern comes from the dead-time and pile-up loses due to the count rate (see Chapter 4).

3.3 The C_6D_6 Detectors

As mentioned above, the C_6D_6 system is one of the two detection systems available to study capture reactions. The C_6D_6 detection system [53] is composed of two deuterated benzene liquid scintillator detectors, characterised by low neutron efficiency. The detectors are situated opposite each other at 135° relative to the beam direction and sample. Being placed behind the sample reduces the instances of sample scattered neutrons and γ-rays entering the detector volume.

The two detectors are not identical, having different volumes, photomultiplier tubes, etc, but having the same scintillation liquid. This allows systematic uncertainties in the individual detectors to be revealed.

The low neutron sensitivity is a particular advantage as it reduces the background resulting from scattered neutrons capturing on the detector material. By replacing the hydrogen with deuterium, and given the low capture cross section of carbon, the neutron sensitivity is reduced to a low level. In fact the neutron sensitivity is 1:10000 meaning that for every 10000 capture reactions, one scattered neutron is detected.

The C_6D_6 detectors are also characterised by low γ-ray detection efficiency which is proportional to γ-ray energy. This is required for the utilisation of the Pulse Height Weighting Technique (PHWT), which requires that one γ-ray be detected per capture event.

Having a low γ detection efficiency also means the C_6D_6 detectors are less effected by the γ-flash than the TAC, and are thus cross sections measurements are able to reach the MeV energy range.

The detectors cover only about 8% of 4π, and have a detection efficiency around 20%, as determined by GEANT4 simulations.

Having two detection systems allows complimentary experiments to be performed. This allows direct comparison of the results of the experiments which are analysed not only with different detector set ups, but also analysis techniques.

3.4 The n_TOF Data Acquisition System

The n_TOF data acquisition system (DAQ) [55] is based on flash ADC (analog to digital converters) digitisers, comprising 40 channels of high performance digitizers each with 8 bit resolution, where each of the TAC modules is one channel. The benefit of this fully digitised set-up is that the raw signals can be digitally converted

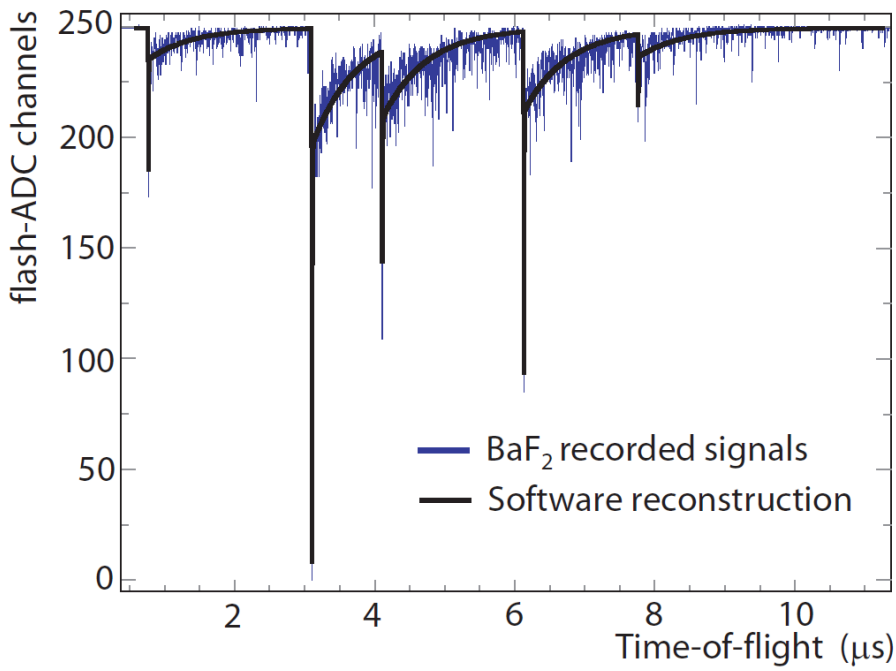

Figure 3.15: The fast and slow scintillation signals stored in a digitised data buffer. Visible are 5 signals that the pulse shape analysis routine has identified and fitted.

and stored, enabling later offline analysis to take place. Issues related to thresholds and pile up can then be dealt with directly by dedicated pulse shape analysis routines (PSA) to optimise the treatment of recorded signals.

When a proton pulse is sent by the PS, it triggers a 16 ms recording window in the DAQ, sampling the received signals at a rate of 500 MHz, corresponding to one point being sampled every 2 ns, and a lower neutron energy limit of 0.3 eV being attained. Recording the entire raw signal results in a huge amount of data. Thus a threshold is applied to the signal and a zero suppression algorithm applied.

The digitized electronic response then has a dedicated PSA routine applied. This fits the fast and slow components of the scintillation light with $\tau_{slow} = 630$ ns and $\tau_{fast} = 0.7$ ns, respectively. Figure 3.15 shows an example of signals in the TAC and the fit applied by the PSA routine. The PSA individually fits the two scintillation light components. The fast component is fitted with a Lorentzian and the slow component with an exponentially decaying fit.

The PSA extracts the essential information determined by the fits, comprising the time-of-flight, signal integral and the module number of the TAC. This information is stored in data summary tape (DST) format in list mode. Both the DST data and the zero suppressed raw data are stored on CERN's Advanced STORage

Table 3.1: The properties of the ^{236}U and auxiliary samples used in the current work are listed here. The ^{236}U sample is composed of 399 mg of U_3O_8, containing 338 mg of uranium in the proportions listed.

Sample	**Thickness (mm)**	**Diameter (mm)**	**Mass (mg)**	**Density (atoms/barn)**	**Isotopic Composition**
Gold	0.1	9.9	185.4	$7.4 \cdot 10^{-4}$	^{nat}Au
Carbon	6	12.0 ± 0.5	1190.7	10^{-3}	^{nat}C
U_3O_8	0.25	10	338	10^{-3}	0.05 % ^{235}U 99.85 % ^{236}U 0.1 % ^{238}U
Dummy	0.25	17.7	462		^{nat}Al

manager (CASTOR) [56]. A routine called dst2root is then later applied to the DST files to convert them into ROOT format [57] for later analysis.

A coincidence window of 20 ns, after the first signal, is used to group all signals in all crystals within this window into a single event. This event is described by information on the total energy deposited in the TAC, the number of crystals used in the detecting the event (crystal multiplicity), and the time of flight corresponding to the first signal appearing in an event.

3.5 The ^{236}U And Auxiliary Samples

In a cross section measurement, the characteristics of the sample under investigation are crucial. The characteristics include not only the sample size, but its chemical and isotopic composition, and if present, the sample encapsulation. These characteristics play a key role in the measurements and in the accuracy that can be reached. For the current work, an existing ^{236}U sample was borrowed from GELINA [58] for the measurement. The characteristics of this sample, and of the auxiliary samples necessary for the measurement are summarized in Table 3.1.

The ^{236}U sample, manufactured at the Institute of Physics and Power Engineering (IPPE) in Obninsk, is composed of 399 mg of U_3O_8 powder (yellow cake), enriched to 99.85% ^{236}U, compressed into a pellet of diameter 10 mm and thickness 1 mm. This compressed pellet is encapsulated inside an aluminium canning composed of two outer disks 17.3 mm in diameter and 0.25 mm thick, and four rings with outer diameter of 17.3 mm and inner diameter 10 mm and thickness 0.25 mm each, with a total mass of 740 mg. Figure 3.16 illustrates the sample dimensions.

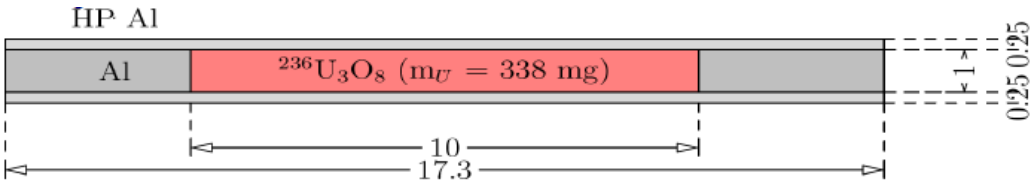

Figure 3.16: Dimensions of the ^{236}U sample and the encapsulating aluminium.

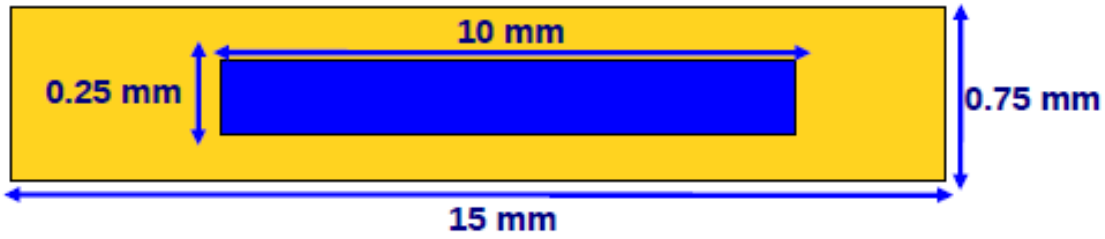

Figure 3.17: Original dimensions of the encapsulated ^{236}U sample as reported by the manufacturer.

To account for the background generated by capture and scattering on the ^{236}U canning, a dummy canning was built at CERN. The dummy sample is made of one disk and one ring of natural aluminium. The disk being 0.5 mm thick and 17.7 mm in diameter and the ring being 0.2 mm thick. Issues arose concerning the dimensions of the ^{236}U sample and encapsulating aluminium as reported by the manufacturer, resulting in the dummy being built to incorrect specifications. The dimensions are reported by the manufacturer as shown in Figure 3.17 where the mass was stated to be 462 mg.

As it was not possible to open the encapsulated sample to determine the mass of the either the sample or the encapsulation, an experimental method was utilized which is outlined in 4.3. Furthermore, the diameter of the ^{236}U sample was determined by x-ray analysis, as shown in Figure 3.18.

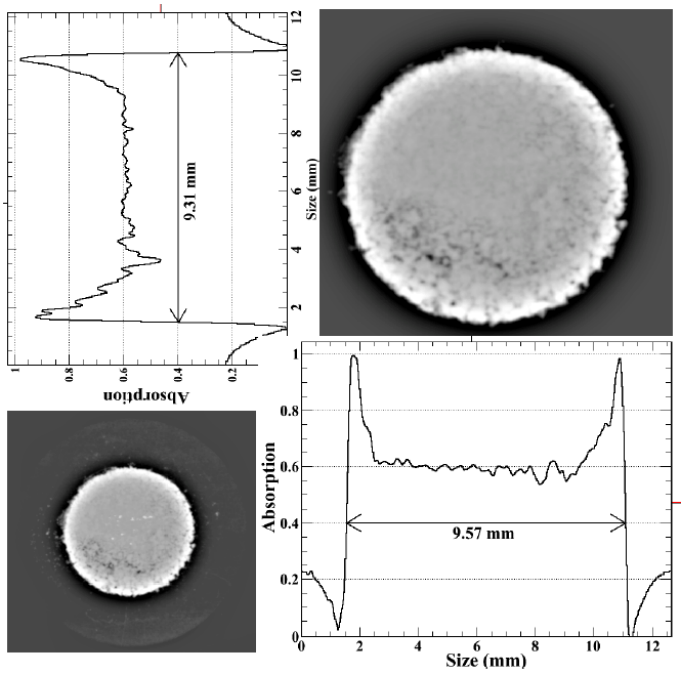

Figure 3.18: Details of the X-ray imaging of the ^{236}U sample.

Further samples used were a disk of natural carbon used to determine the scattering background, and a gold sample for calibrating the neutron energy. The ^{236}U , dummy, gold and carbon samples are all housed in frames comprised of two 25 μm kapton foils glued to a PCB ring 55 mm in diameter.

Chapter 4

Data Analysis: From Raw Data To Yield

This chapter deals with all aspects of the analysis of the experimental data obtained during the ^{236}U(n, γ) experiment. The following sections discuss all the steps in the analysis involved in the calculation of the yield from the raw data coming out of the detector: quality checks, analysis conditions in terms of E_{sum} and m_{cr}, background subtraction, dead-time correction and normalization. Last, the uncertainty associated to each of these steps is discussed in detail.

4.1 Quality checks for data acceptance

After processing all the DST files into ROOT format, it is then necessary to sum together all the individual data runs to get the total statistics which will then undergo data reduction. Before this is done, a series of quality checks were performed on all run files to reject those that do not meet certain criteria, thus ensuring a consistent set of data.

All the detectors in place during the measurements (PKUP, SiMon and TAC) are measuring neutron induced reactions and thus the counting rates recorded should be proportional among each pair of chosen detectors and proportional also to the incident number of protons, which is given to us by the PS. In order to check this a set of ratios between these quantities was taken:

1. (Number of entries in the TAC) / (Number of entries in SiMon)
2. (Number of entries in the TAC) / (Area of signal in the PKUP)

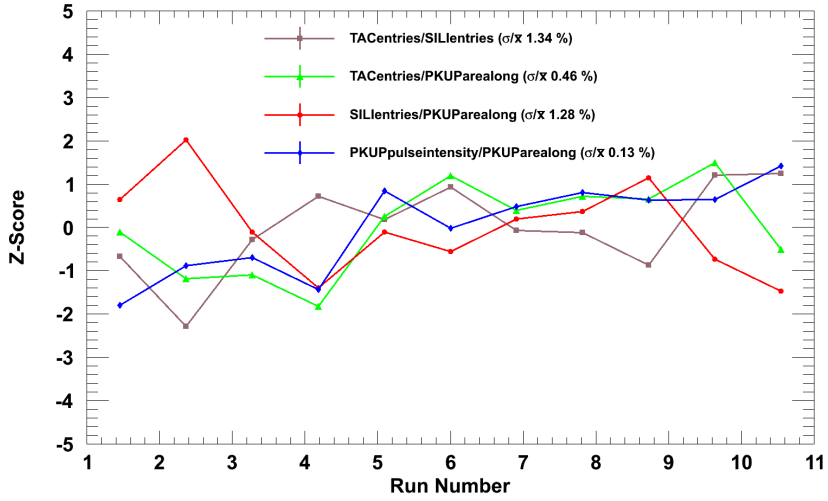

Figure 4.1: Plot showing the use of the z-score to quality check the data for each run. This example shows the quality checked dummy canning data. The z-score was determined for four different quantities (see text for details).

3. (Number of entries in SiMon) / (Area of signal in the PKUP)

4. (Pulse intensity from the PS) / (Area of signal in the PKUP)

This was checked by calculating the z-score and the coefficient of variance. The z-score, z, is calculated as:

$$z = \frac{x - \bar{x}}{\sigma} \tag{4.1}$$

where $\bar{x}$ is the mean and σ is the standard deviation. This quantity is the signed number of standard deviations that a data point is from the mean. A range of ± 3 was chosen with runs outside this range being rejected. The z-score is then determined again for the reduced data set and once more, any runs with values outside the chosen range are rejected. This process is repeated until a final, consistent set of data is arrived at. A total of 1.65×10^{18} protons were taken to complete the current work, which after quality checks was reduced to 1.40×10^{18}, resulting in a rejection of 15% of the initial data. Figure 4.1 shows an example of the output for the dummy canning runs after outliers had been rejected.
The coefficient of variation, $c_v = \frac{\sigma}{\bar{x}}$, is displayed for each of the four quantities in the legend. This value describes the relative variability about the mean, or, alternatively, the relative magnitude of σ. As seen in Figure 4.1, the low values of c_v indicates that there is a very tight spread of values about the mean. This was the case for

all the final quality checked data sets, hence, as expected, for what constitutes the valid data set, all detectors's counting rates are proportional to each other and thus the overall data set is consistent.

A last check was made by comparing the data sets taken in different periods to see whether all of them were compatible. There were three distinct $^{236}\mathrm{U}(\mathrm{n},\gamma)$ and two distinct sample-out data taking periods, all separated by runs with different samples. The data from the different periods have been compared and found to be fully consistent, and thus all the data for a given sample was summed together.

4.2 Analysis Conditions and Background

This section will consider the rationale for the cuts on deposited energy and crystal multiplicity that were used to improve the capture to background ratio, and the subsequent method used to account for, and subtract, the different sources of background. Finally, a problem is detailed relating to the dummy sample mass and how this was studied and rectified.

4.2.1 Analysis Condition On E_{sum} And m_{cr}

The high total absorption efficiency of the TAC allows to distinguish different types of reactions according to the amount of energy that is deposited in the TAC (E_{sum}). This is also true but less straightforward with the number of crystals (m_{cr}) that, out of the 40 available, fire simultaneously in a registered event. In the following we discuss how we can apply conditions on these variables to enhance the capture to background ratio.

Analysis conditions are applied to the data to reduce the experimental background in the TAC. However, these conditions need to be selected carefully as these cuts also reduce the statistics and therefore the detection efficiency. An investigation as to what the optimum conditions on multiplicity and deposited energy was therefore conducted.

When a neutron is captured on $^{236}\mathrm{U}$ into an excited state of $^{237}\mathrm{U}$, this excited state is close to the neutron separation energy of $^{237}\mathrm{U}$. Thus an upper energy cut for deposited energy about 5.1 MeV seems reasonable, as is evident in Figure 4.2. But to account for effects such as the detector resolution and cases where small signals pile up with the signal from the cascade of the excited $^{237}\mathrm{U}$ nucleus, this energy range was extended to 6 MeV. Energy deposited in the TAC more than 6 MeV is

due to neutron scattering and pile up events.

Neutron capture reactions on barium isotopes and fluorine typically have Q-values around 6.5 MeV and above (with the exception of ^{138}Ba where $Q = 4.7$ MeV), and neutron capture reactions on aluminium in the canning and beam line has a Q-value of 7.7 MeV. However, γ-rays from a cascade that are lost or only deposit a fraction of their energy in the TAC means that counts from scattering events can occur within the optimum capture range.

At lower deposited energies, there is a small contribution to the background from radiative capture on hydrogen (2.2 MeV) and a large contribution from the de-excitation of ^{6}Li nucleus following an (n, α) capture on boron in the moderator (478 keV). However, the dominant background between approximately 1-3 MeV comes from the beam-off background, as is evident in Figure 4.2. Thus a lower energy cut on the deposited energy of 2.5 MeV was selected.

One drawback of applying conditions in both E_{sum} and m_{cr} is that real capture events are lost, and thus efficiency is reduced. For instance, it was seen by comparing data in strong capture resonances that, for the selected energy conditions, changing the multiplicity condition from $m_{cr} > 1$ to $m_{cr} > 2$ reduced the detector efficiency by 20%. With the above cuts for energy and a multiplicity cut of $m_{cr} > 2$, the efficiency of the TAC for detecting gamma cascades was approximately 57%. With the same energy cuts and a $m_{cr} > 1$, an efficiency of approximately 72% was obtained. A plot of the distribution of different multiplicity events is shown in Figure 4.3, where it can be seen that the majority of events, without conditions, correspond to multiplicity 1.

Thus the choice of cuts of $2.5 < E_{sum}\,(MeV) < 6.0$ and $m_{cr} > 1$ were chosen for the final analysis as they allowed the best trade off between background reduction and efficiency.

4.2.2 Background Subtraction

There are various sources of background that need to be subtracted from the experimental data to obtain a data set including only the capture reactions of interest. In the current work, these background sources were the environmental background (so-called beam-off), the background due to the aluminium canning containing the ^{236}U sample (so-called dummy), the background related to the beam but not related to the sample (so-called sample-out), and the neutron sensitivity background arising from neutrons scattered at the sample and captured somewhere else, and giving

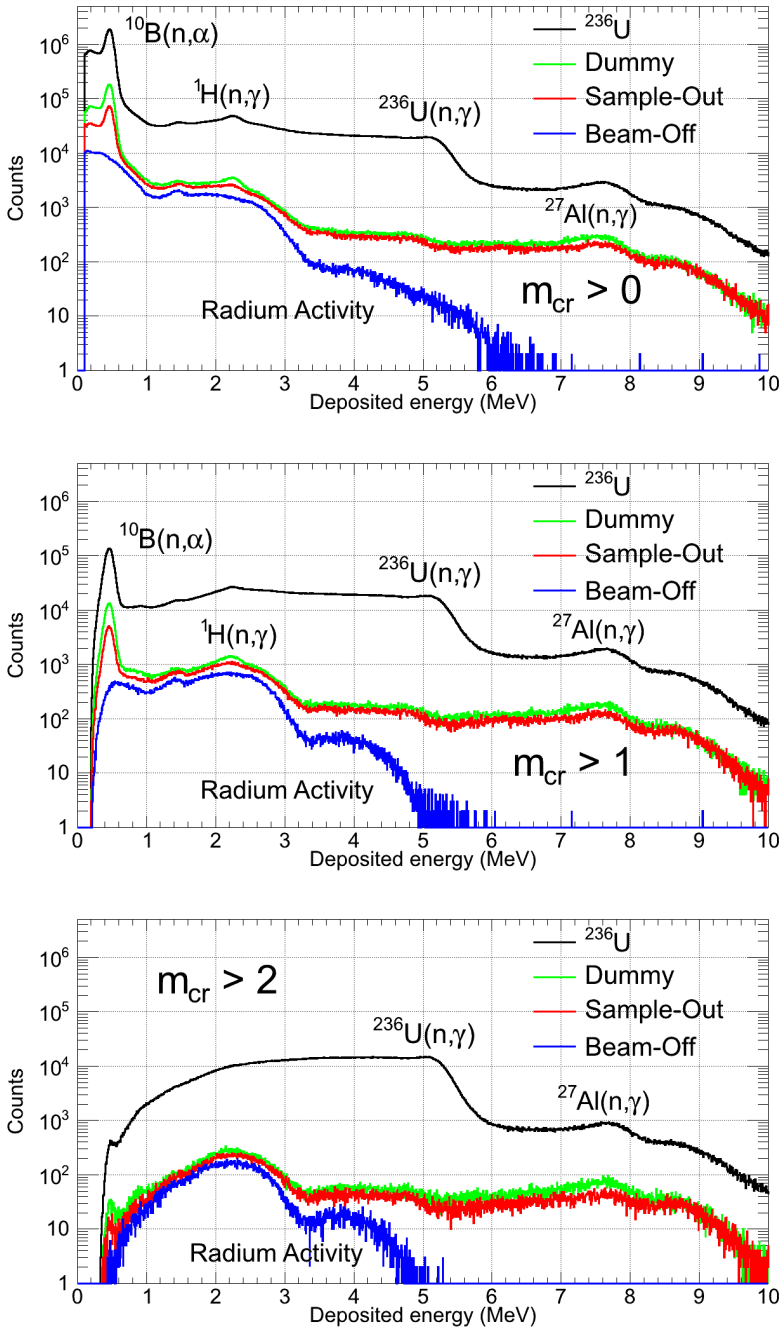

Figure 4.2: Deposited energy spectra for three different multiplicity cuts, $m_{cr} > 1, 2, 3$, for the ^{236}U, dummy, sample-out and beam-off samples. The effect of increasing the multiplicity is to reduce the background, and the effect on the various contributions is seen.

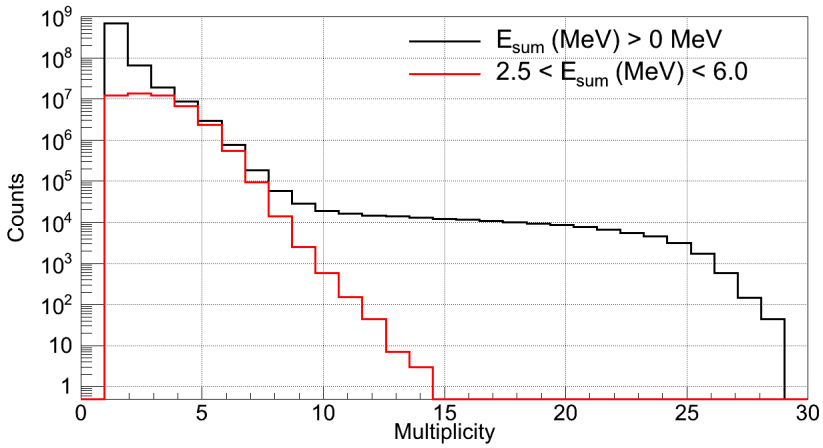

Figure 4.3: Plot of the multiplicity for all events recorded in the TAC, and for all events with conditions on deposited energy.

rise to signals in the TAC. Separate runs were dedicated to all of the background sources to allow for background subtractions. The beam-off background was performed without the sample in place. To determine the sample activity background, a beam-off run was performed with the sample in place, but was found to be indistinguishable from the background with no sample. ^{236}U decays by pure α-emission and has very low intensity associated γ-ray emission (49 and 112 keV), which is below the detection threshold.

The neutron sensitivity background is more difficult to determine. Before quantifying this, the other sources of background were subtracted from the ^{236}U data. As different samples received beam for different periods of time or received no beam at all, as in the case of the beam-off run, the different backgrounds need to be scaled to each other before subtraction can be done. The beam-off was scaled to measuring time (equivalent to DAQ events) and other backgrounds were scaled to incident proton beam intensity. This subtraction procedure is illustrated in Equation 4.2.

$$\begin{aligned} U_{capture} = & \left[C_U - C_B \cdot \frac{E_U}{E_B}\right] - \left[C_S - C_B \cdot \frac{E_S}{E_B}\right] \cdot \frac{P_U}{P_S} \\ & - \left[\left(C_D - C_B \cdot \frac{E_D}{E_B}\right) - \left(C_S - C_B \cdot \frac{E_S}{E_B}\right) \cdot \frac{P_D}{P_S}\right] \cdot \frac{P_U}{P_D} \end{aligned} \tag{4.2}$$

where C_x, E_x and P_x are Counts, Events and Protons respectively, and the subscript x is replaced by U, D, S or B for Uranium, Dummy, Sample-out or Beam-off. Figure 4.4 shows the neutron energy spectra for ^{236}U and the different contributions before

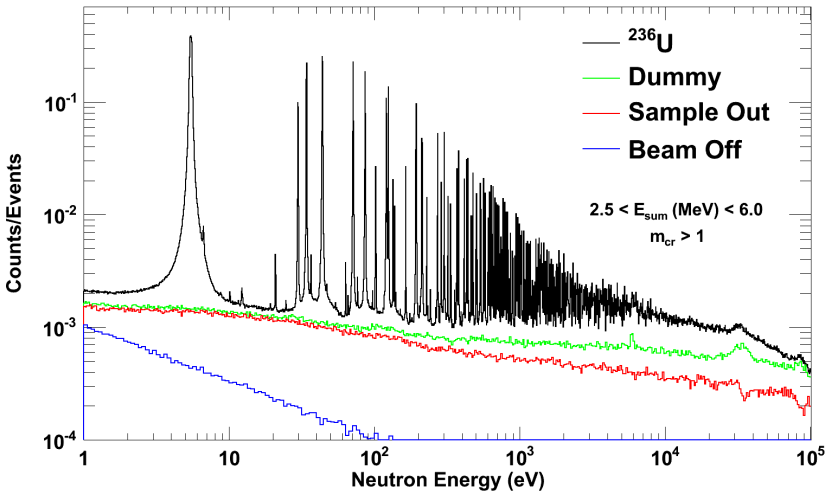

Figure 4.4: Neutron energy spectra of the ^{236}U, dummy, sample-out and beam-off data scaled to events. The good signal-to-background in the resonances is clearly visible.

background subtraction.

To investigate the neutron sensitivity background required a more in-depth investigation. Dedicated runs were performed with a pure carbon sample which behaves as a pure neutron scatterer. After subtracting the beam-off and sample-out contributions from the carbon, the 'clean' background subtracted deposited energy spectra of the ^{237}U and carbon are then compared. In the region from 7 to 10 MeV, where neutron capture on ^{236}U does not contribute and all events recorded in the TAC are from scattered neutrons (or pile up - discussed in Section 4.5), the integral of the carbon data is scaled to the integral of the ^{236}U data to obtain a scaling factor which is applied to the carbon spectra. Assuming that the response of the TAC to sample scattered neutrons is independent on the type of sample (Carbon or Uranium), this scaled carbon data gives the expected neutron scattering contribution from ^{236}U. This result of this procedure is shown in Figure 4.5.

The fraction of the uranium "clean" spectra corresponding to neutron scattering is calculated in each neutron energy bin following the above described method. Looking at the results, it was observed that the scattering contribution varies significantly from resonance to resonance, as expected, and is negligible for most resonances and ranges up to a maximum of 4% for TOF data and 8% for EAST data (see figure 4.9). Figures 4.6, 4.7 and 4.8 illustrate the scattering contribution for the resonances at 5.45 eV, 102 eV and 967 eV.

Due to the limited statistics involved, rather than subtract this small background

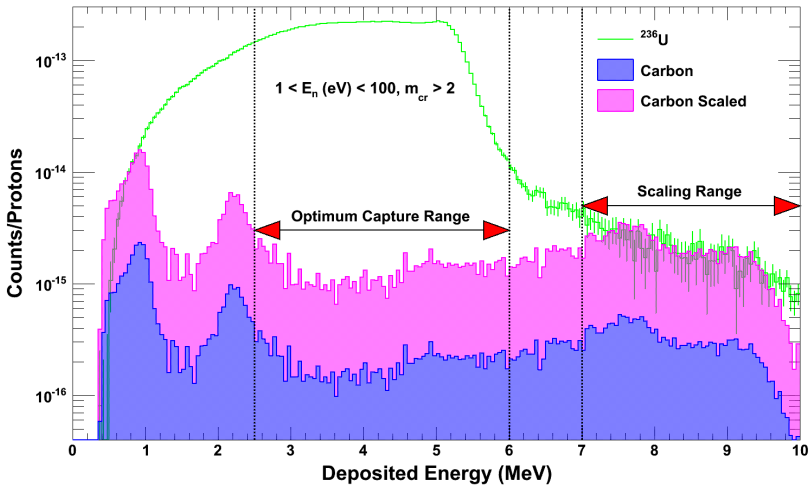

Figure 4.5: Plot showing the scaling of the carbon data to the ^{236}U data in the 7 - 10 MeV range. In the optimum capture range, which corresponds to the cut on deposited energy, the scaled carbon data now corresponds to the scattering contribution to ^{237}U.

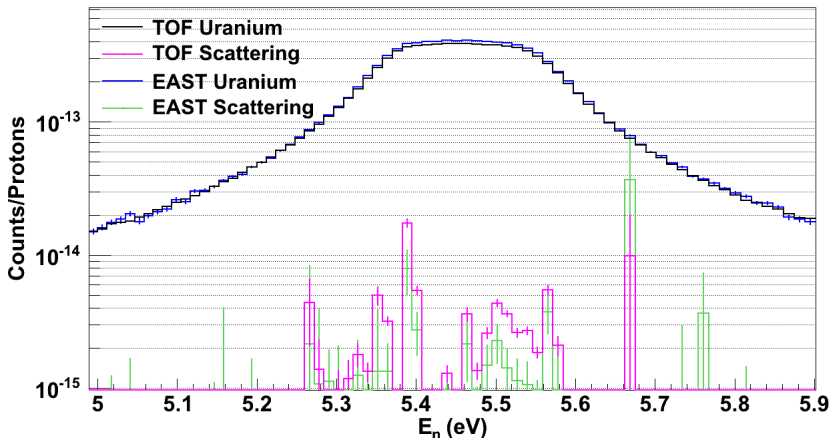

Figure 4.6: Plot of the background subtracted 5.45 eV resonance and the associated scattering spectra.

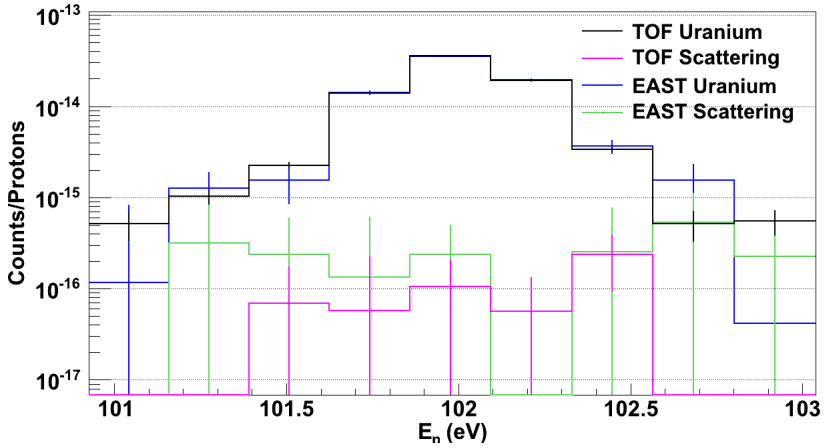

Figure 4.7: Contribution of scattering to the 102 eV resonance.

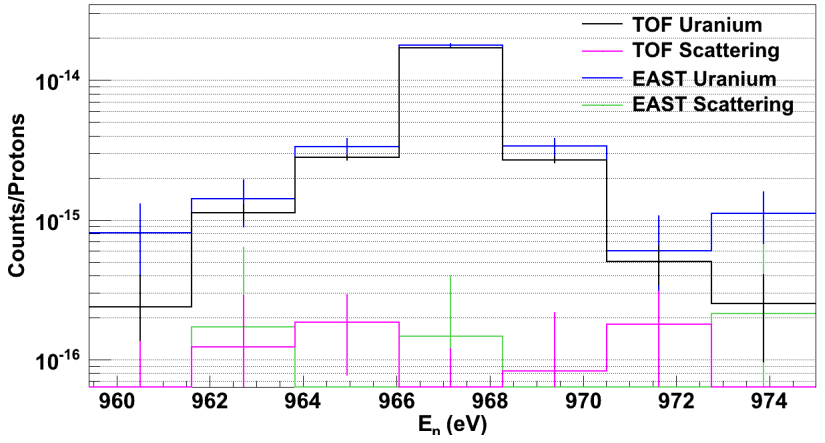

Figure 4.8: Contribution of scattering to the 967 eV resonance.

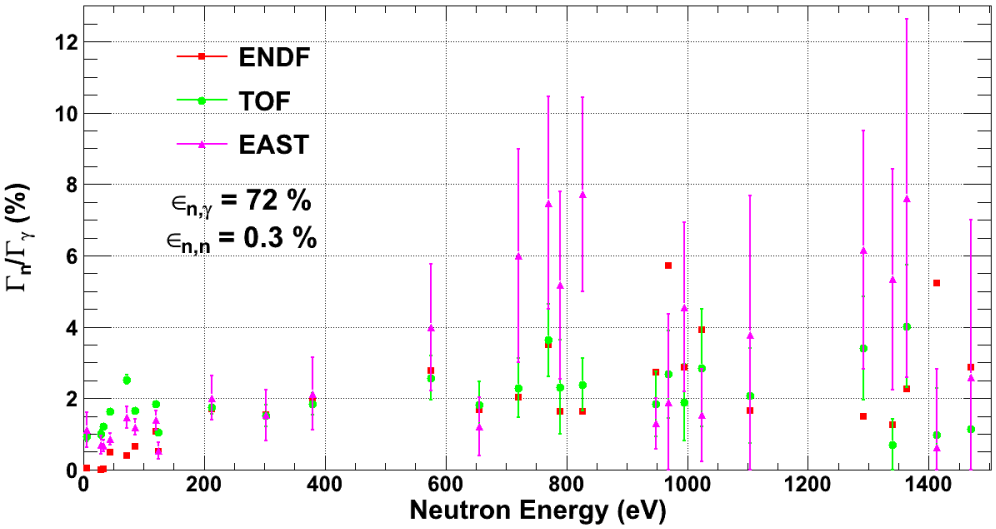

Figure 4.9: Plot of the ratio of Γ_n/Γ_γ for the ENDF and experimental TOF and EAST data.

which has large relative errors which would be propagated to the capture data, another prescription is followed. Taking the integral of the counts of a resonance from the neutron energy spectra as determined above, the scattering to capture ratio is calculated, and this is assigned as the uncertainty associated to neutron scattering in the corresponding resonance integral.

In order to check if the obtained result in terms of neutron scattering contribution to the measured resonances makes sense, we have compared this with the expected value if one assumes the scattering to capture ratios from the ENDF evaluation have a TAC efficiency to neutrons of 0.3% (from previous experiments) and of 72% for γ-rays (with the chosen analysis conditions). The neutron and capture widths of the largest resonances were taken as too were the widths of those resonances with the largest neutron widths according to ENDF. The neutron and capture widths in ENDF were then corrected by the efficiency of the TAC for the relevant particle before the ratios were taken. The experimental and evaluated ratios are shown in Figure 4.9.

Looking to the 27 scattering to capture contribution ratios shown in Figure 4.9, for the TOF data, 17 resonances have a scattering contribution of 2% or below, 7 resonances a contribution of 2-3% and 3 resonances have a contribution of $> 3\%$. The other resonances having a scattering contribution $< 1\%$. A similar situation is seen for the EAST data, with 16 resonances having a scattering contribution of 2%

or below, 1 having a contribution of 2-3% and 10 resonances having a contribution of $> 3\%$ (4 between $3 - 5\%$ and $6 > 5\%$).

4.3 Problems With The Dummy Sample

In undertaking the analysis of the ^{236}U capture cross section with the C_6D_6 detectors in [59], which used the same sample as the current work, it was noticed from the deposited energy spectra that there appeared to be a problem with the dummy canning spectra. The same was noticed in the current TAC data.

In the region above 6 MeV, where capture on ^{236}U does not play a role, and as capture on aluminium results in the release of 7.7 MeV from the de-excitation of the compound nucleus which is formed, aluminium should dominate this region. The 7.7 MeV peak is shown in Figure 4.2 where a cut on neutron energy of $1 < E_n\,(eV) < 10$ has been applied, but the dummy spectra sits below the ^{237}U spectra in the high energy region.

The dummy canning was constructed at CERN based on the dimensions of the sample as reported by the manufacturer. In light of the observed discrepancy, the total mass of the sample and its dimensions were measured at GEEL. This measurement determined that all the dimensions reported by the manufacturer were erroneous, not only the mass of the canning but also the radius and the thickness. The mass of the canning as reported by the manufacturers was 462 mg and the mass of U_3O_8 was reported as 399 mg. The total mass of the sample (U_3O_8 plus canning) was measured at GEEL to be 1140 mg - if the mass of U_3O_8 was correct, the canning should have a mass of 741 mg.

The situation was therefore that the correct mass of the dummy canning had to be determined before the correct dummy background could be subtracted from the capture data. This could be experimentally determined from the TAC data. The sample-out data was subtracted from both the 'dirty' ^{236}U capture and the dummy deposited energy spectra. The environmental background does not contribute in the high energy range as is clear from Figure 4.2 and was therefore neglected. In the range from 6.5 to 8.5 MeV, Gaussian fits were applied to the dummy and the ^{237}U peak (which retains the contribution from the canning) with a centroid at 7.7 MeV. The ratio of these peaks was then taken giving a correction factor to be applied to the dummy data for all subsequent data reduction work. This is shown in Figure 4.10.

The result of this procedure was the determination of a canning correction factor

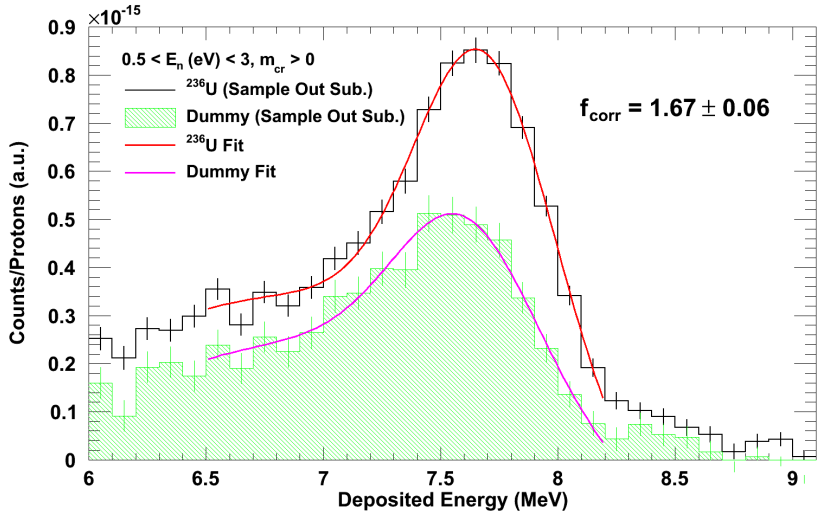

Figure 4.10: Fits to the background subtracted deposited energy dummy spectra and the the ^{236}U spectra with all but the canning background removed.

of 1.64 ± 0.08. This is within the error of the value of 1.60 determined by taking the ratio of the mass of the canning as determined by GEEL and the mass of the dummy at CERN. Applying the correction factor would mean the mass of the canning was actually 757 mg. Comparing to the GEEL measurement, the correction to the dummy mass as determined by the current work gives an actual mass which is correct to 2%. Applying this correction to the dummy deposited energy spectra resulted in a good agreement the spectra as is shown in Figure 4.11, where the spectra now include all background. As the only difference between the dummy and the ^{237}U data now is capture on ^{236}U, good agreement is seen between both spectra except in the region where there is capture on ^{236}U. It was therefore now possible to subtract the backgrounds correctly.

4.4 Time-Of-Flight To Neutron Energy calibration

In the current experiment the TOF to neutron energy calibration is related only to flight path distance L between the spallation target and the ^{236}U sample. More accurate than measuring the geometrical distance, and given that the spallation target is quite voluminous, the most accurate estimation of the flight path L is performed by making all the ^{197}Au(n, γ) resonances measured in the current work agree with the corresponding resonance energy values of the most accurate measurement to

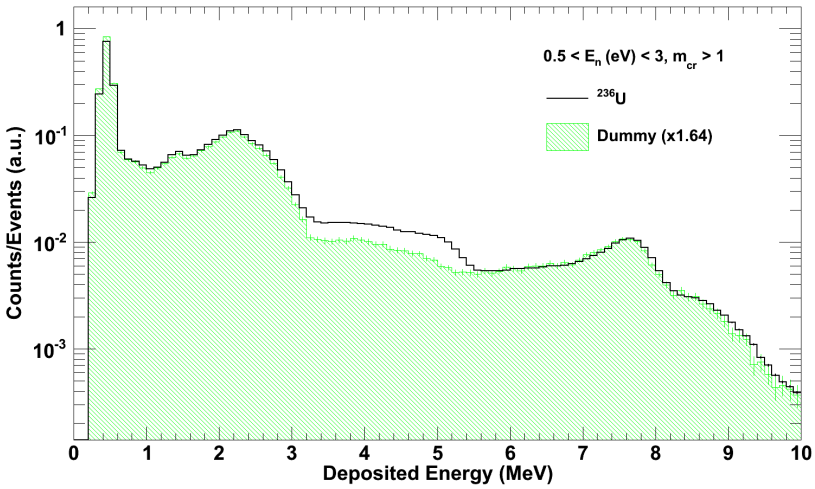

Figure 4.11: The deposited energy spectra for the dummy and ^{237}U samples with full backgrounds, after applying the dummy correction factor.

date [60].

The procedure followed here was to fit a Gaussian to the experimentally observed ^{197}Au resonances as seen in the data taken for the current work. The energies at which the peaks occurred were compared with the resonance energies in [60]. This was done for approximately 15 resonances. The resulting average value and the corresponding uncertainty is 185.67 $\pm$ 0.02 meters. Applying this to the ^{236}U(n,γ) data showed discrepancies between the resonance energies in the current work and ENDF. A preliminary comparison with the spectra obtained in [59] showed good agreement, as seen in Figure 4.12.

The experimental data for the 5.45 eV resonance shows it to be shifted to higher energy relative to ENDF. This is the only resonance where this is the case. All other resonances in ENDF are at higher energy relative to the experimental data of the TAC and C_6D_6. In fact, consideration of the energy difference shows all other resonances to be offset by a factor of 0.1%.

4.5 Dead Time And Pile Up

Dead-time and pile-up are two different, but related, effects occurring in detector arrays in counting experiments. It is necessary to account for these effects as they can introduce significant uncertainties by affecting the detected signals.

After a signal is recorded in a detector, there is a period of time following this

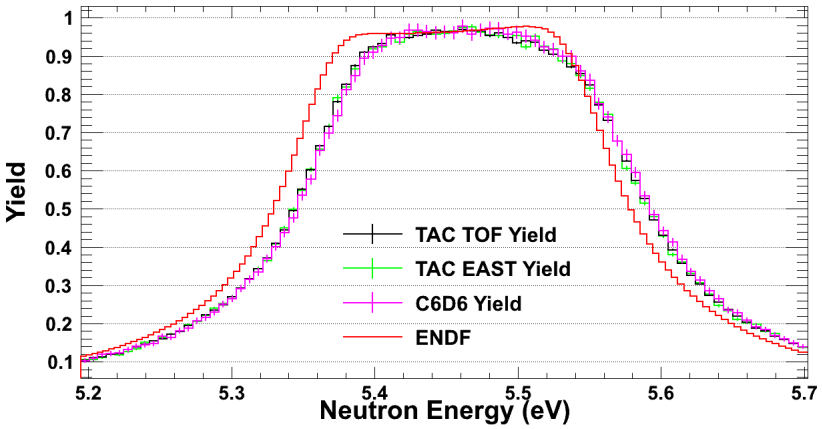

Figure 4.12: Comparison of the data from the TAC, C_6D_6 and ENDF for the 5.45 eV resonance. The data from the two detectors are in very good agreement, whilst both differing from the ENDF/B-VII.1 evaluation.

where the detector is unable to identify further signals. This period of time is referred to as the dead time. This results in a loss of counts, multiplicity and a reduction in deposited energy for every signal arriving during the dead-time.

Pile-up occurs when multiple events occur close in time, giving rise to the possibility of multiple signals in a given detector module being registered as one signal. For example, should two signals in a detector module be close in time, only one may be seen, reducing the counts, multiplicity by one, and having an energy that is equal to as much as the sum of the two signals.

Considering the 40-fold segmentation of the TAC, and the high instantaneous neutron flux capable of producing a high count-rate at the n_TOF facility, given the $\tau_{slow} = 630$ ns slow component of the scintillation light in the BaF_2, there is a very real chance that another signal could be sitting on on top of a previous signal, making its identification by the pulse shape analysis routine difficult.

Analytic solutions for dead time and pile-up corrections exist [61] for when only one or two detectors are operating in coincidence, but this is not the case with a large number of detectors operating in coincidence, as with the TAC, owing to the event reconstruction routine increasing in complexity as the array size increases, which precludes such a simple approach.

A new method was developed at n_TOF for correcting for dead-time and pile-up in a detector array for constant and rapidly varying count-rates [62], based on Monte Carlo simulations which recreate the entire process of signal detection and the subsequent event reconstruction. Given the many resonances in actinides, the

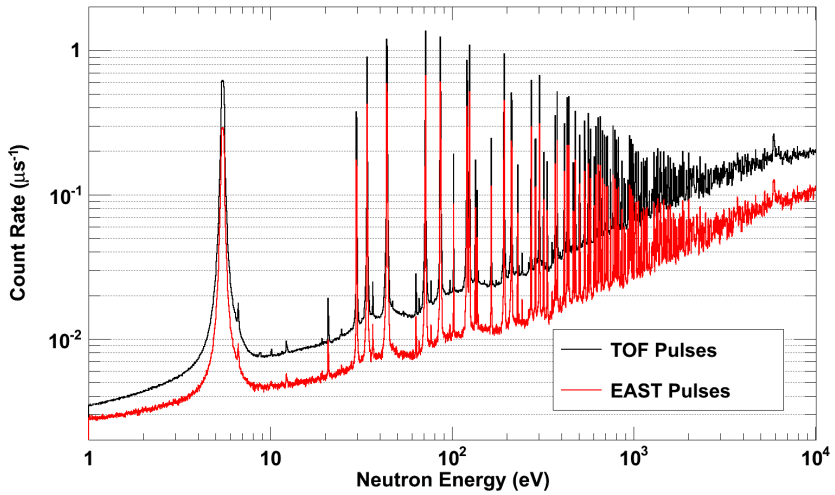

Figure 4.13: Count rates recorded in the TAC for TOF and EAST pulses for $m_{cr} > 1$ and $E_{sum} > 1MeV$.

count rate can vary rapidly over small energy ranges, as is seen for the case of ^{236}U in Figure 4.13 for both TOF and EAST pulses.

Using the time between consecutive signals with a constant counting rate, a time interval distribution was constructed based on experimentally obtained initial signal deposited energy E1, and a subsequent signal depositing energy E2. This was done from 500 keV to 6.5 MeV using energy intervals of 500 keV at a time. This is illustrated in figure 4.14 for E1 = 6-6.5 MeV and various E2 energy intervals.
For a constant count rate, the time between successive signals follows a distribution function [61]:

$$I_1 \, \mathrm{d}t = ne^{-nt} \, \mathrm{d}t \tag{4.3}$$

Where t is time and n is the rate of signal occurrence. As can be seen in Figure 4.14, for each combination of E1 and E2, there is a characteristic time interval where the distribution deviates from the expected exponential behaviour, and this is used to define the dead time at the point where the distribution differs by less than 10% from the expected theoretical distribution. The dead time for all E1 and E2 combinations is illustrated in Figure 4.15. From this, the average dead time was determined to be $1\,\mu$s, with an upper limit of $3\,\mu$s.

As the deposited energy and crystal multiplicity conditions are used to identify different reactions and to optimise the capture-to-background ratio, should any signal be lost from an event due to dead time or pile-up, then the whole event may

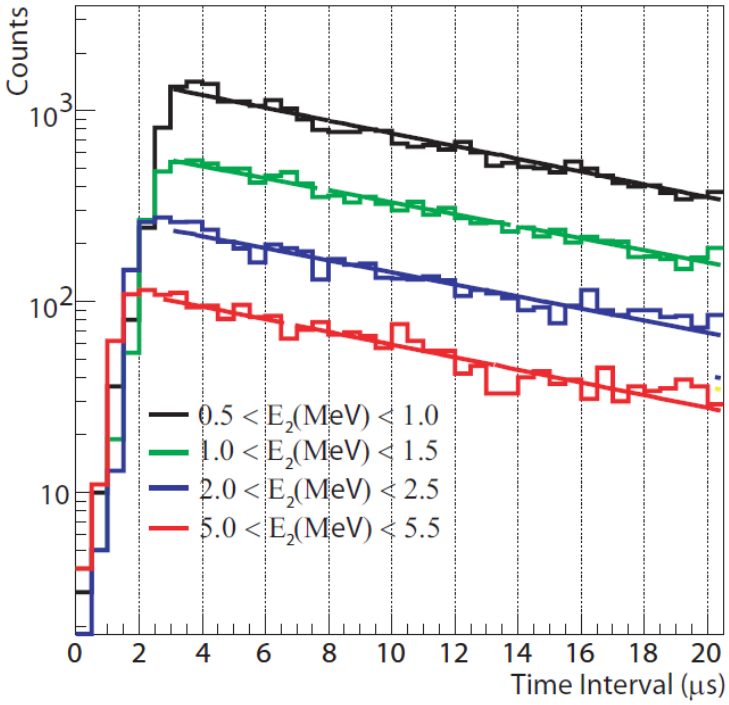

Figure 4.14: Time interval distribution for $E1 = 6 - 6.5$ MeV for four E2 intervals. Moving to smaller time intervals shows a deviation from the expected exponential form.

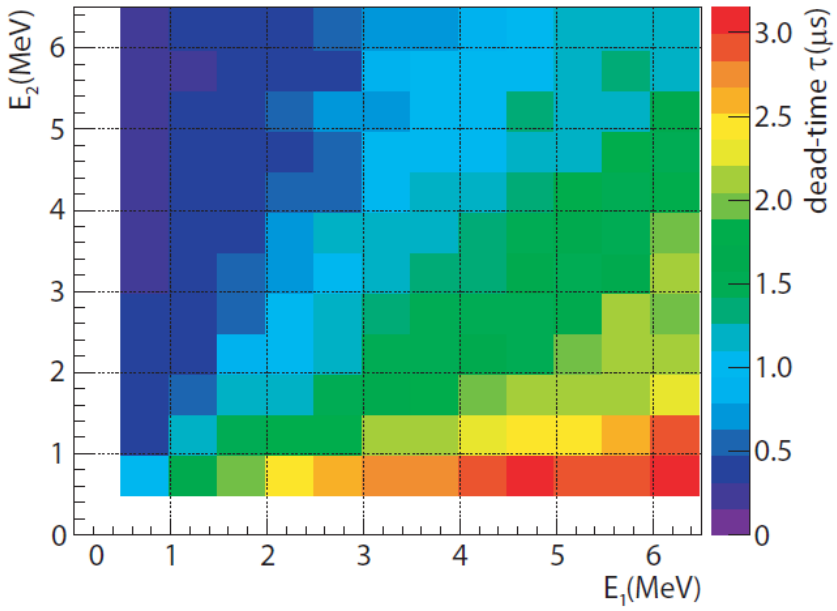

Figure 4.15: Plot of the dead time of all E1/E2 combinations. The average dead time is approximately 1 μs

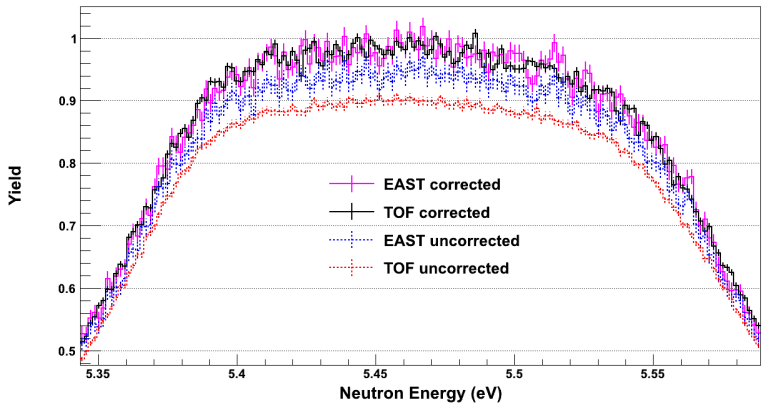

Figure 4.16: The 5.45 eV resonance data from the TAC for the TOF and EAST pulses, at 8000 bpd. Shown are the spectra both before and after dead time and pile-up corrections were applied. After corrections, the TOF and EAST spectra agree to better than 0.1%.

be rejected by the analysis conditions. Further, for two separate events occurring within the coincidence window of 20 ns can result in the individual energies being summed and the signal in this case also being rejected.

With an average dead time around 1 μs, it is the case that dead time losses will become significant a counting rate of 1 count/μs. Not only will dead time and pile-up affect the counting statistics, most importantly, they will also affects the efficiency of the TAC in detecting capture cascades.

At the n_TOF facility, having beams of different intensity, i.e. the TOF (high intensity of 7×10^{12} ppp) and EAST (low intensity with 3×10^{12} ppp) pulses for the current work, means that a direct comparison can be made of the data sets with different counting rates to study the situation before and after corrections are made. This is shown for the saturated resonance in ^{236}U at 5.45 eV in Figure 4.16.
The saturated resonance for the TOF and EAST pulses differed by 6% before corrections were applied, and after corrections were applied this difference was by within 0.1%, giving confidence that the method used is indeed accurate. These corrections were applied up to 640 eV, as at higher energies the effect is negligible.

Due to the good agreement between the TOF and EAST pulses after the corrections, as the EAST pulse account for just 10% of the total statistics, it was decided to only use the TOF data, rather than combine them, due to the higher statistical uncertainty associated with the lower count rate of the EAST data, at least in the 1-1500 eV range.

4.6 Yields And The Saturated Resonance Technique

With the backgrounds subtracted and dead time and pile-up corrections applied to the data, it is now possible to determine the experimental yield. As stated in Section 2.2.2, the experimental yield is determined by:

$$Y_{n,\gamma}(E_n) = \frac{C(E_n) - B(E_n)}{\varepsilon \cdot N_{BIF} \cdot \phi(E_n)} \tag{4.4}$$

Where the counts, the background and the flux have all been measured, the normalisation factor $\varepsilon \cdot N_{BIF}$ still needs to be determined. For resonances that saturate, it is convenient to make use of the saturated resonance technique [63]. A saturated resonance is one that demonstrates a plateau instead of peak because all the incident neutrons interact with the sample, meaning that the yields saturates, with a value close to unity. Earlier it was stated that capture and elastic scattering are often the only probably reactions with low energy neutrons, and that the theoretical yield is given by:

$$Y_{n,\gamma}(E_n) = \left(1 - e^{-n\cdot\sigma_t(E_n)}\right) \cdot \frac{\sigma_{n,\gamma}(E_n)}{\sigma_t(E_n)} \tag{4.5}$$

And for a capture reaction where $n\sigma_t \gg 1$ gives the approximation:

$$Y_{n,\gamma}(E_n) = \frac{\sigma_{n,\gamma}(E_n)}{\sigma_t(E_n)} \tag{4.6}$$

If, for a given energy range this ratio is 1, then essentially all of the neutrons in the beam at this energy impinging on the target will undergo radiative capture, and the yield will saturate at unity. The plateau value of a saturated resonance does not depend much on the values of the resonance parameters and thus it can be very accurately determined analytically. Then the comparison between the measured yield and the expected one provides the scaling factor ($\varepsilon \cdot N_{bif}$) needed so that both yields agree. The experimentally determined value of $\varepsilon \cdot N_{bif}$ at the saturated peak for both TOF and EAST data sets was 0.136. From previous experiments, the beam interception factor for a 1 cm sample was 0.19 (i.e. sample covers 19% of the beam). Thus the efficiency was determined to be $\approx$ 72% for the chosen multiplicity and deposited energy conditions.

In order to calculate the shape of the expected yield for the ^{236}U saturated resonance at 5.45 eV as accurately as possible the SAMMY code was used which

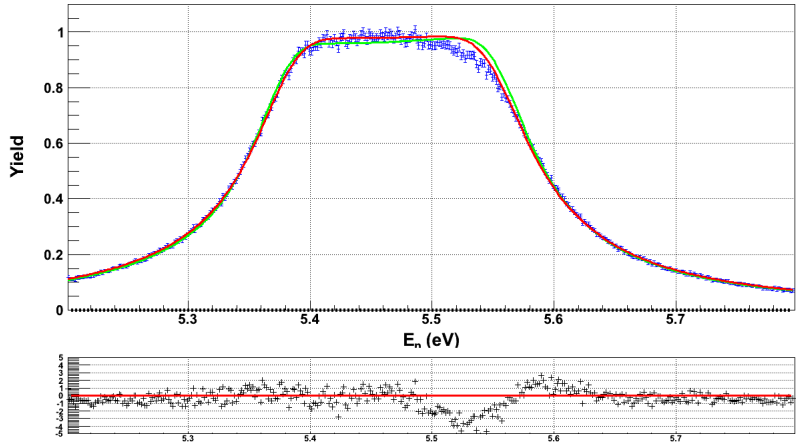

Figure 4.17: Normalisation of the saturated resonance at 5.45 eV, showing the experimental data (blue) initial fit from ENDF resonance parameters (green) and the SAMMY fits with Γ_γ and Γ_n left free (red).

includes all the experimental effects such as sample geometry, Doppler broadening, resolution function, etc, using as initial parameters the ENDF/B-VII.1 values, for a variety of parameters left free or fixed. It was found that the best fit to the data was when Γ_γ and Γ_n were left free to vary. No combination of parameters free or fixed resulted in a good fit to the right shoulder of the resonance, and thus this was the best that could be achieved. The fit is show in Figure 4.17 where the green is the fit using the initial parameters with just energy left free, and the red fit is with energy and Γ_γ and Γ_n free.

A clear problem affecting the accuracy of the normalisation in the current work is that of the shape of the evaluated and experimental resonance at 5.45 eV. The ENDF data shows a clear 'bump' on the right hand side of the peak due to multiple scattering, a bump that is not there in the experimental data. The reason for this inconsistency is not known, but is possibly due to the treatment of multiple scattering in SAMMY. Five different fits were performed with all possible combinations of resonance parameters and they have all yielded consistent values within 1.5%, which is what is considered the uncertainty in normalization or the current work.

The capture and neutron widths determined from the SAMMY fit gave values of $\Gamma_\gamma = 35.5\,\text{meV}$ and $\Gamma_\text{n} = 1.60\,\text{meV}$ giving a radiative kernel of $RK = 1.53$. The resonances parameters from ENDF give $\Gamma_\gamma = 24.5\,\text{meV}$ and $\Gamma_\text{n} = 1.60\,\text{meV}$ leading to $RK = 2.05$. Although the parameters of the individual widths of the current work can not be deemed accurate (as transmission data would be needed for this), the kernel can. The SAMMY fits show that the the RK of the current work to be

25% lower than ENDF.

With the normalisation determined, it could now be fixed in SAMMY. Resonance parameters can now be extracted for all resonances by leaving free permutations of energy, neutron and capture widths. The results of these fits are reported in the next chapter.

4.6.1 Residual Background

After normalisation, but before fitting the resonances proper to extract the resonance kernels, the residual background was accounted for. After subtracting the background, as discussed in section 4.2.2, it is possible that some small background contribution remains.

To determine the form of the background, groups of two or three resonances were fit over different energy ranges between 1 to 1500 eV, paying attention to the value of the yield in the valleys between resonances, where this residual background should be visible. The value of this background was calculated at different neutron energies and then its dependence with neutron energy was found, which can be described as:

$$F(E_n\ (eV)) = a + \frac{b}{\sqrt{E_n\ (eV)}} \tag{4.7}$$

The result of the fit is shown in Figure 4.18, which also shows the values obtained for the coefficients.
These coefficients are then put into the SAMMY parameter file and then fixed. With the normalization and residual background accounted for and fixed, the final fits to the resonances to extract the corresponding resonance integrals (i.e. radiative kernes) could then be performed.

4.7 Uncertainties

There are many potential sources of uncertainty to be accounted for in any experiment. Whereas the statistical error is more straightforward to deal with, the systematic errors pose more of a challenge. All the sources of uncertainty relevant to the current work are discussed below.

1. Sample mass: uncertainty given by the manufacturer as 1.5%

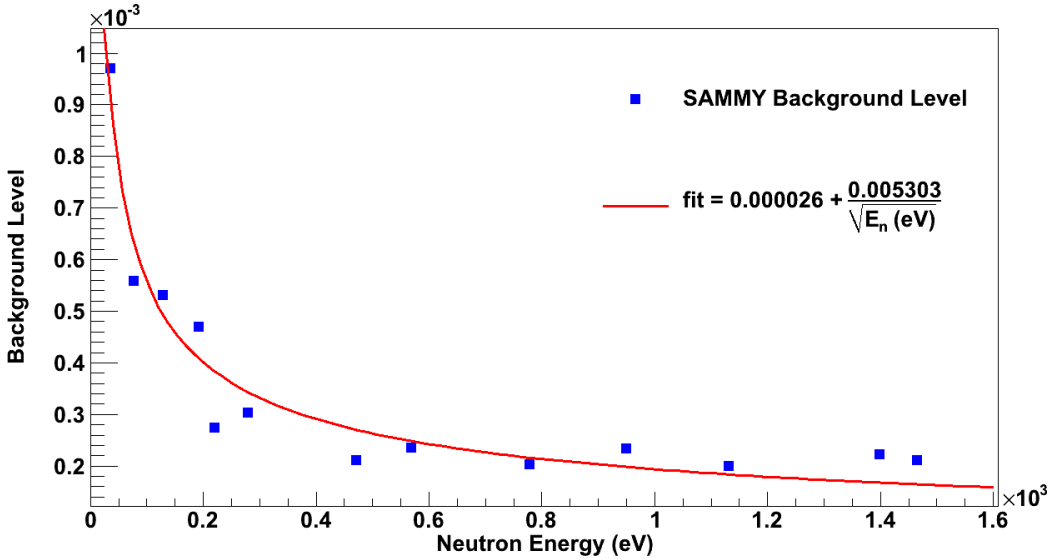

Figure 4.18: Residual background fit, as determined by SAMMY, showing clearly the $\frac{1}{\sqrt{E_n}}$ *behaviour.*

2. Neutron flux: The error in the neutron flux ranged from 1-2% in the RRR from 1 to 1500 eV. Details of this are found in [50], and can be seen in Figure 3.6.

3. Normalisation: The error on the normalisation factor was discussed in Section 4.6, where by fitting the 5.45 eV saturated resonance with different conditions and taking the standard deviation, the normalisation factor was determined to be 0.983 ± 0.015, giving a 1.5% error.

4. Dead time and pile up corrections: For many resonances the dead time and pile-up correction is zero, and this is taken as the lower limit. For the three resonances with the largest count rate (43.91, 71,47 and 86.51 eV), as seen in Figure 4.13, the correction factors applied to the TOF data were 1.2. Applying a conservative uncertainty to this correction of 20% gives an estimation of the uncertainty due to the dead time and pile-up of 2.5%. More accurately, the integrals of these resonances were taken after applying the corresponding dead time and pile-up correction to both the TOF and EAST data to see the agreement between them, and were found to be 1%, 1.7% and 0.6% respectively. Thus, the upper limit on the uncertainty was taken to be 2%.

5. Neutron Scattering: According to Section 4.2.2, and in particular to the results in Figure 4.9, we see that in the worst case, the effects of neutron scattering go

*Table 4.1: Summary of all the sources of uncertainty and their estimated contributions to the total. (*see text for details). The best case is for resonances where there is little pile-up and scattering contribution, and the worst case for resonances with high pile-up and scattering contribution.*

Source of Uncertainty	Best Case (%)	Worst Case (%)
Sample mass	1.5	1.5
Neutron flux	1-2	1-2
Normalisation (ϵN)	1.5	1.5
Dead time and Pile-up	0*	2
Neutron Scattering	0*	4
Background subtractions	0*	0*
Total	2.3-2.9	5.0-5.3

up to 4% for the TOF data. For many resonances, the scattering contribution is negligible, and thus the scattering contribution to the total uncertainty was determined to range from 0 to 4%.

6. Background subtractions: It was seen in Section 4.2.2 that a 5% error existed due to the problem with the size of the dummy sample. As the aluminium background is smooth, with the resonances in the RRR sitting on top of this, even if the background were not subtracted correctly at this stage, it would be accounted for in the residual background as discussed in Section 4.6.1. The background will thus have negligible effect on the area of the resonance, and therefore the background contribution to the radiative kernels is taken to be zero.

Whereas the uncertainty on the sample mass, normalisation are background are constant, and the neutron flux uncertainty varies little over the energy range of interest, the uncertainty on the dead time and pile-up and neutron scattering vary on a resonance by resonance basis. The contribution to the uncertainty in the current work are tabulated in Table 4.1, along with the total uncertainty in the best and worst cases.

From Table 4.1 it is seen that for the best case, where scattering and the counting rate is small, the uncertainty ranges from 2.3 to 3%. In the worst case, for resonances with high pile-up and/or high scattering, the uncertainty ranges from 5-5.3%. This puts the uncertainty of the yield within the requested accuracy 10%, and in fact reaching the goal of 5%.

Chapter 5

Resonance Analysis And Comparison To Previous Evaluations

This chapter will outline the resonance analysis of the experimental yield performed with the R-matrix code SAMMY. A discussion of the results will then be had which compares the results of the current work to the previous evaluations.

5.1 The SAMMY Analysis

SAMMY was used to analyse 116 resonances between 1 and 1500 eV using as a starting point the resonances energies (E_R) and partial widths (Γ_γ and Γ_n) of the ENDF/B-VII.1 library. This energy region corresponds to the limit of the RRR in both the ENDF/B-VII.1 and JEFF-3.2 libraries, while the JENDL-4.0 library's RRR extends up to 4.5 KeV. Analysis of over the range from 1.5 to 4 keV will be performed in the near future.

Having previously determined the residual background and normalisation and having fixed them in SAMMY, to achieve the resonance analysis fits were performed leaving E_R, Γ_γ and Γ_n free or fixed in various combinations that will be discussed in the following. Comparisons were made of the resonance analysis results across the whole energy range in the following situations:

1. E_R free
2. E_R, Γ_n free

3. E_R, Γ_γ free

4. E_R, Γ_n, Γ_γ free

Leaving just E_R free, in all cases, failed to reproduce the strength of the resonance and the tails adequately. Allowing just Γ_n or Γ_γ to be free similarly failed to fit the tails adequately for the large majority of cases, reproducing only in some cases the resonance peaks. The best fits in all cases were found by leaving Γ_γ and Γ_n free. One issue that needs to be discussed in detail is the analysis of resonances affected by sizeable multiple scattering effects. The multiple scattering is indeed difficult to calculate, the neutron in each interaction against a moving nucleus loses part if its energy and takes some time, taking this time delay into account and the influence of Doppler and resolution broadening is not straightforward and that is why the results from the SAMMY fits are not satisfactory. This was seen in the previous chapter when determining the normalisation factor with the 5.45 eV saturated resonance, and is evidenced by the residuals, which determine the quality of the fit, for several of the fits to the larger resonances in Figure 5.1, for example. Figure 5.2 shows the SAMMY fits, and the comparisons to ENDF, JENDL, on the 44 eV and 71 eV resonances. The effects of multiple scattering mean that the kernel of these resonances cannot be determined with such a good accuracy as all of the others.

The fits and the corresponding residuals across the 1-1500 eV energy range are shown in Figure 5.1 and Figures 5.3 to 5.16, which show in the bottom panels the residuals of the fit for each point i is determined via:

$$\frac{Fit_i - Data_i}{\Delta_i} \tag{5.1}$$

In order to illustrate how, in most cases, using the resonance parameters available in the different evaluations fail to reproduce the data in the current work, Figure 5.17 displays a few examples the data of the current work and fit with the evaluations. In all cases the evaluations have been shifted in neutron energy to agree with the current work so the comparisons show only the difference in resonance strength and shape. Various situations are shown corresponding to resonances where an evaluation has a fit similar to the current work and where an evaluation shows considerable difference to the current work.

Once all the resonances below 1500 eV had been fitted in SAMMY, they were checked individually to ascertain the quality of the fit, and the SAMMY output files checked to be sure the Γ_γ and Γ_n values of the fit had not taken on non-

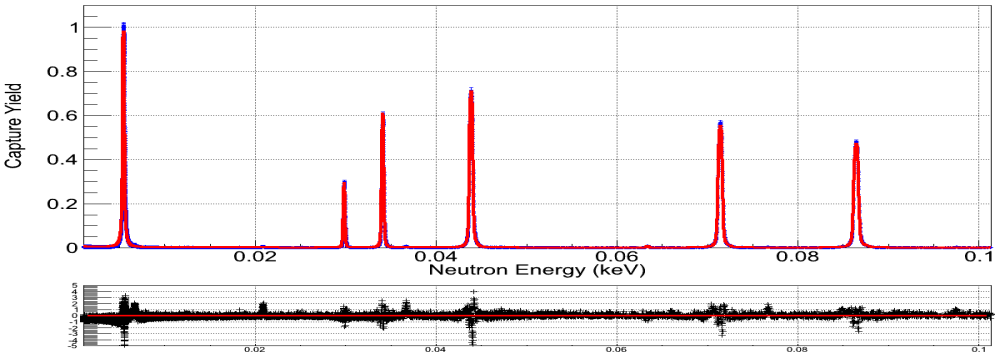

Figure 5.1: Experimental capture yield (blue) and SAMMY fits (red) for the energy range 1 to 100 eV, and the associated residuals.

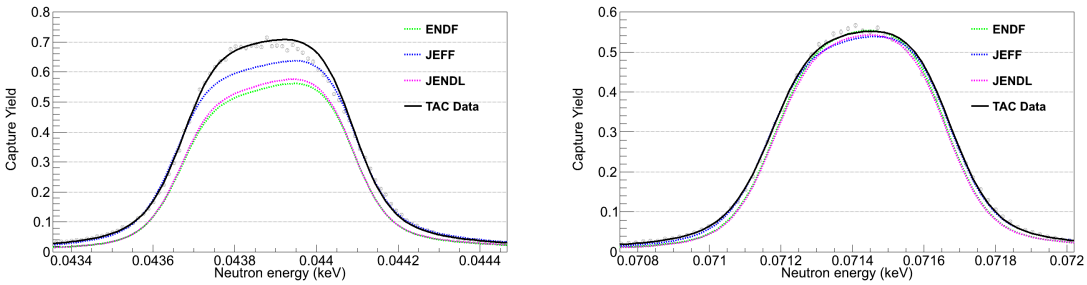

(a) 44 eV resonance. *(b) 71 eV resonance.*

Figure 5.2: Plots showing the experimental data (grey points) and the SAMMY fit to the data (black), for two resonances, 44 and 71 eV, suffering from the effects of multiple scattering. The experimental fits are compared against the ENDF/B-VII.1 (green), JEFF-3.2 (blue) and JENDL-4.0 (magenta) data bases.

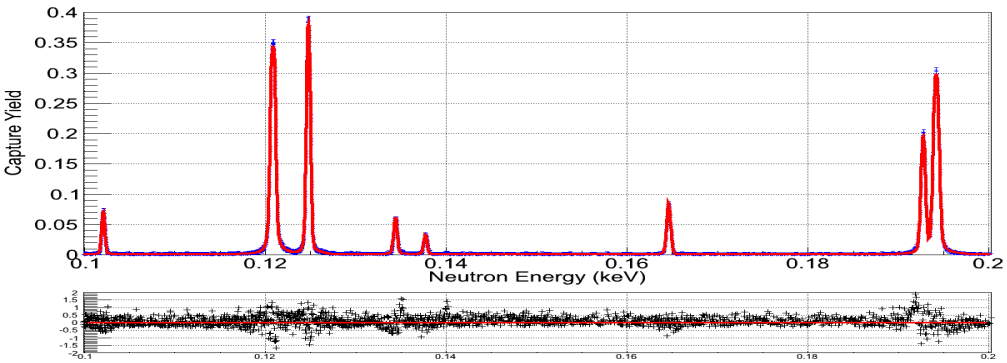

Figure 5.3: Experimental capture yield (blue) and SAMMY fits (red) for the energy range 100 to 200 eV, and the associated residuals.

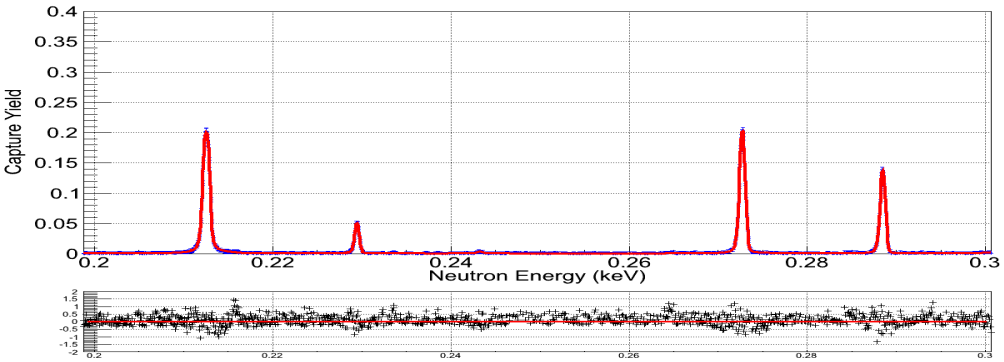

Figure 5.4: Experimental capture yield (blue) and SAMMY fits (red) for the energy range 200 to 300 eV, and the associated residuals.

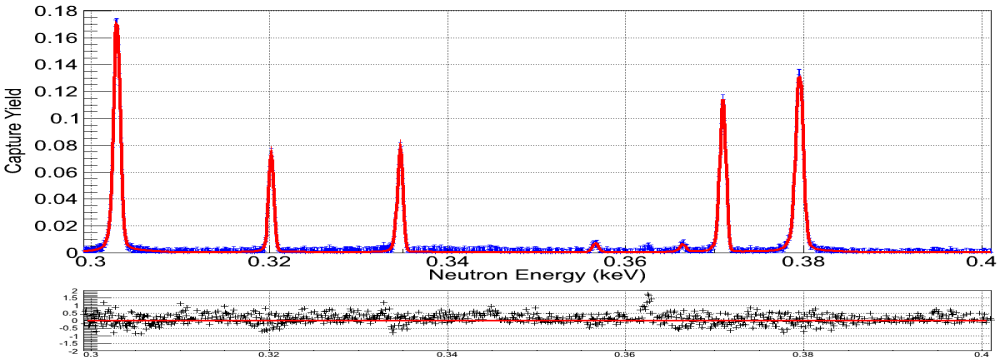

Figure 5.5: Experimental capture yield (blue) and SAMMY fits (red) for the energy range 300 to 400 eV, and the associated residuals.

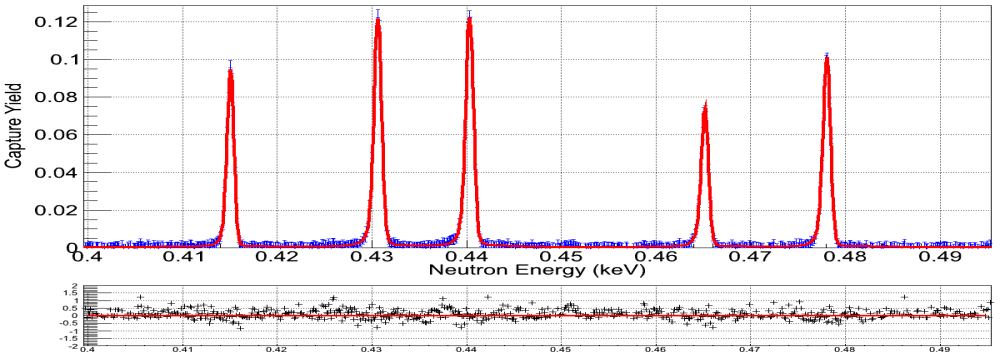

Figure 5.6: Experimental capture yield (blue) and SAMMY fits (red) for the energy range 400 to 495 eV, and the associated residuals.

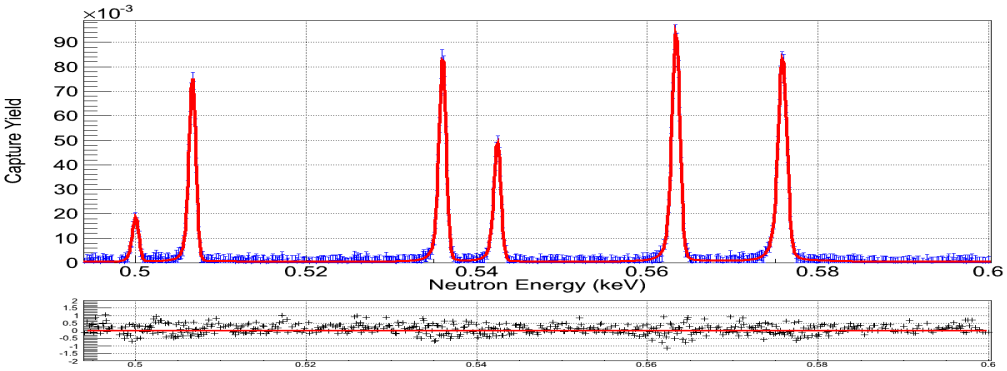

Figure 5.7: Experimental capture yield (blue) and SAMMY fits (red) for the energy range 495 to 600 eV, and the associated residuals.

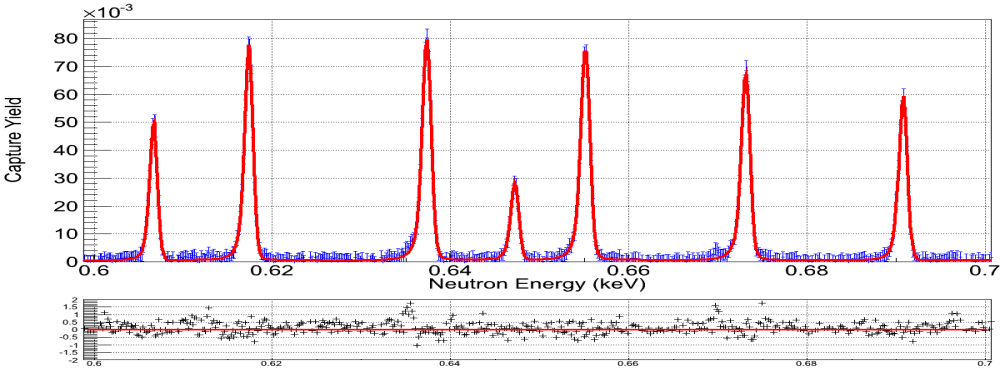

Figure 5.8: Experimental capture yield (blue) and SAMMY fits (red) for the energy range 600 to 700 eV, and the associated residuals.

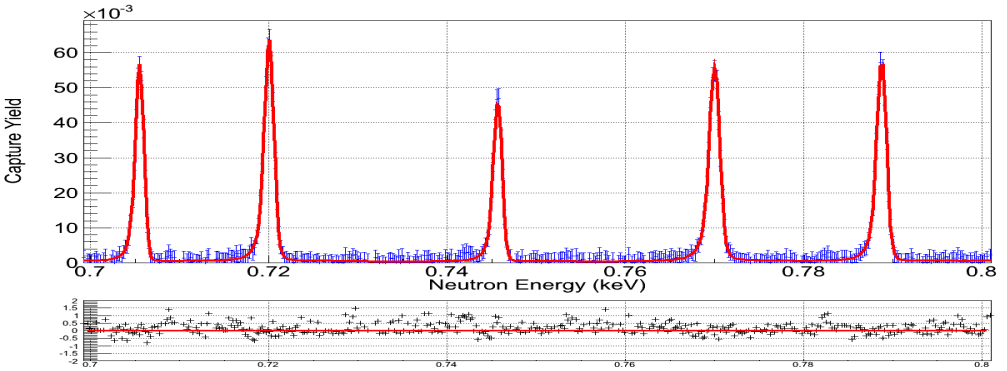

Figure 5.9: Experimental capture yield (blue) and SAMMY fits (red) for the energy range 700 to 800 eV, and the associated residuals.

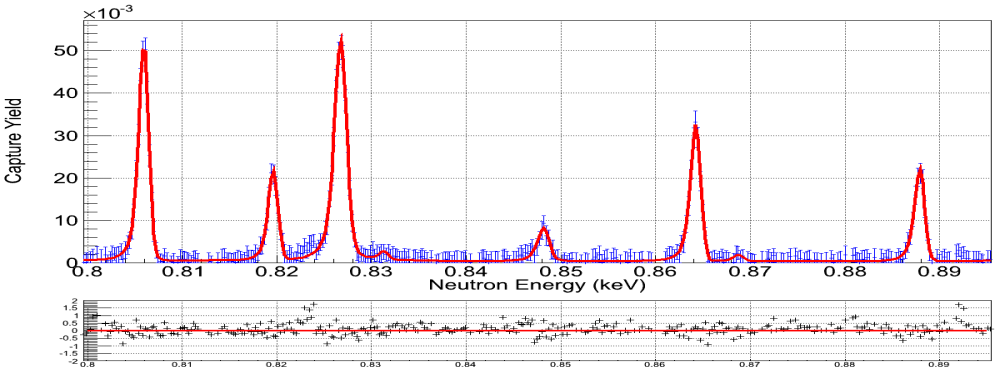

Figure 5.10: Experimental capture yield (blue) and SAMMY fits (red) for the energy range 800 to 895 eV, and the associated residuals.

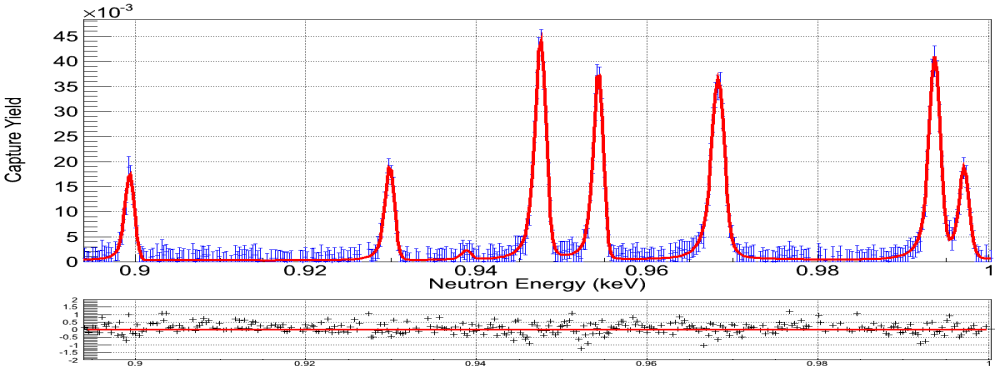

Figure 5.11: Experimental capture yield (blue) and SAMMY fits (red) for the energy range 895 to 1000 eV, and the associated residuals.

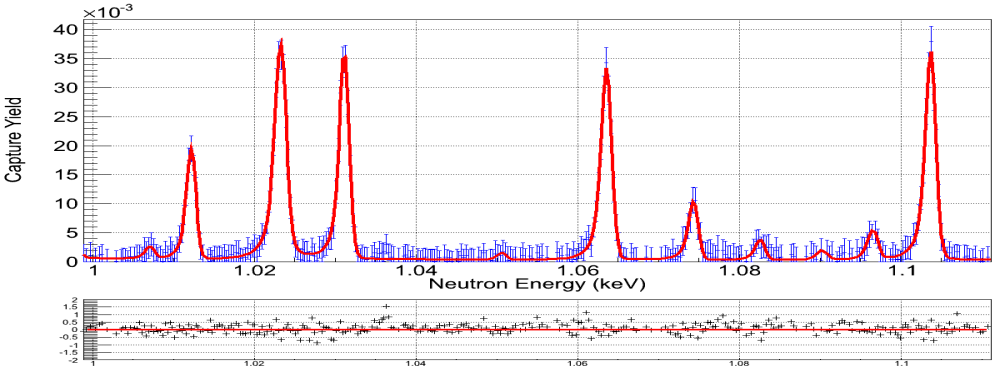

Figure 5.12: Experimental capture yield (blue) and SAMMY fits (red) for the energy range 1000 to 1110 eV, and the associated residuals.

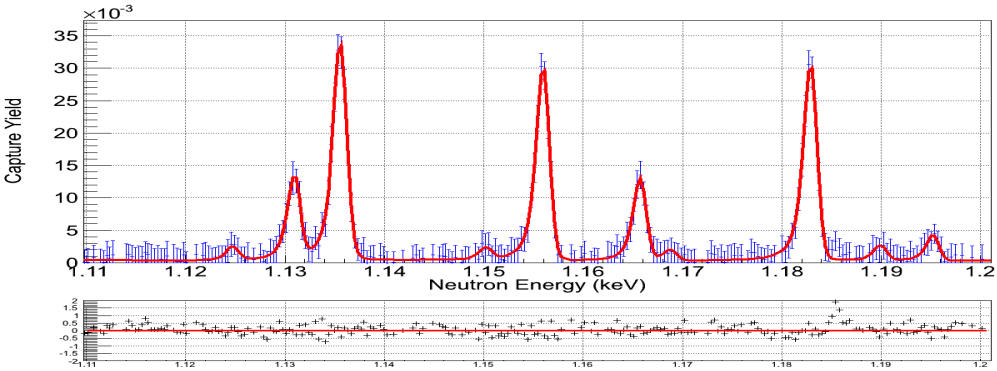

Figure 5.13: Experimental capture yield (blue) and SAMMY fits (red) for the energy range 1110 to 1200 eV, and the associated residuals.

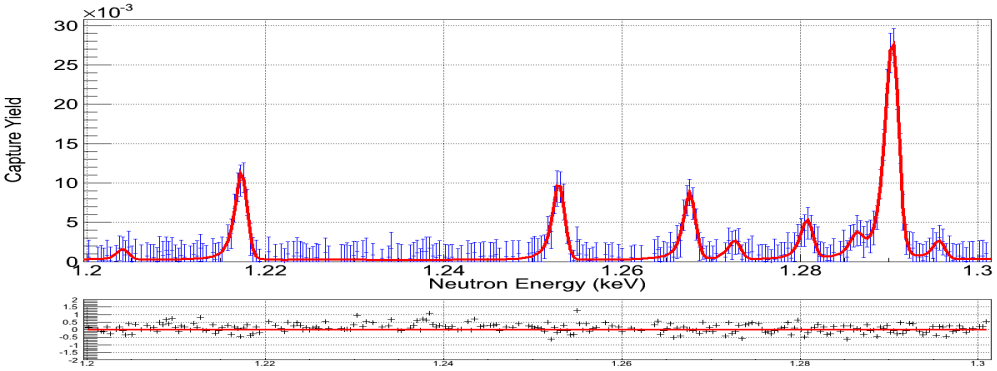

Figure 5.14: Experimental capture yield (blue) and SAMMY fits (red) for the energy range 1200 to 1300 eV, and the associated residuals.

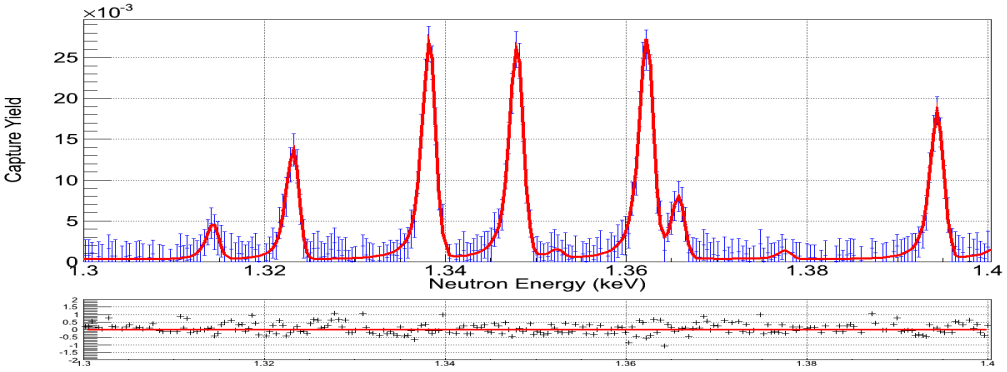

Figure 5.15: Experimental capture yield (blue) and SAMMY fits (red) for the energy range 1300 to 1400 eV, and the associated residuals.

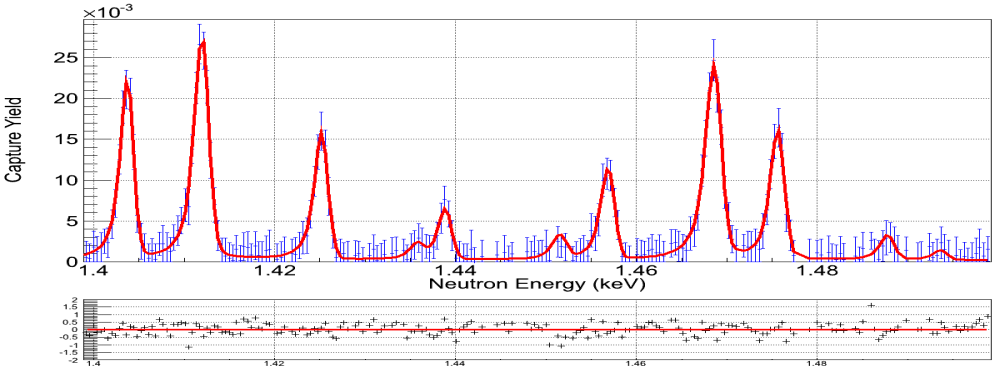

Figure 5.16: Experimental capture yield (blue) and SAMMY fits (red) for the energy range 1400 to 1500 eV, and the associated residuals.

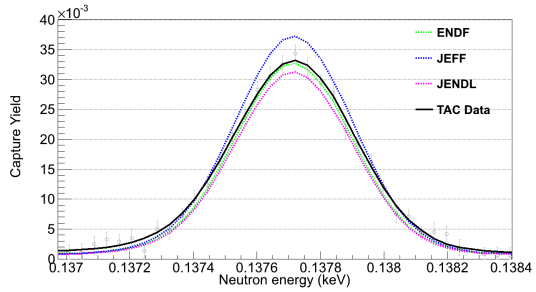

(a) 138 eV resonance.

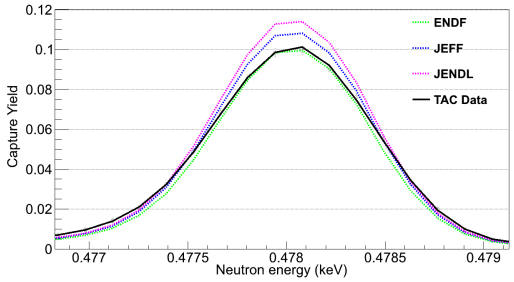

(b) 478 eV resonance.

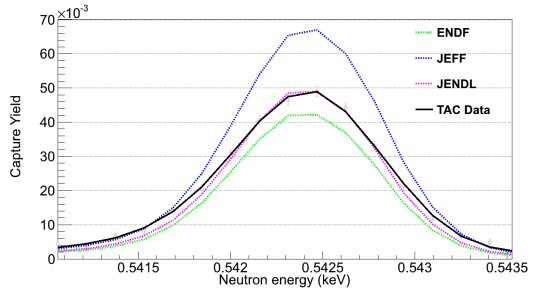

(c) 542 eV resonance.

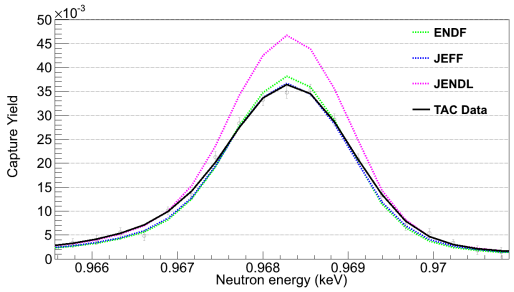

(d) 968 eV resonance.

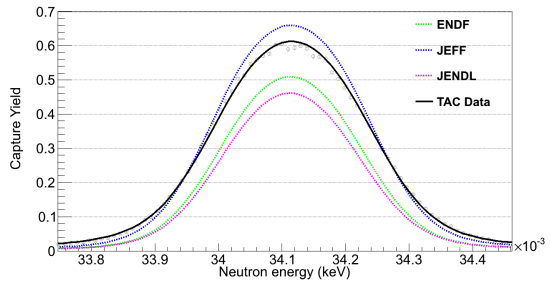

(e) 34.1 eV resonance.

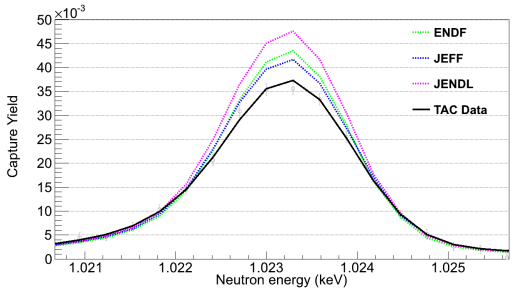

(f) 1023 eV resonance.

Figure 5.17: Plots showing the experimental data (grey points) and the SAMMY fit to the data (black). The experimental fits are compared against the ENDF/B-VII.1 (green), JEFF-3.2 (blue) and JENDL-4.0 (magenta) data bases.

physical negative values. The current work includes only one set of capture yield data, and considering that the capture and scattering widths are comparable for most resonances, the actual values of Γ_γ and Γ_n can not be stated with confidence, only the kernels can be determined accurately. However, the partial widths resulting from the current analysis are also provided, see Appendix A, and for comparison, the partial widths from ENDF, JEFF and JENDL.

Having fitted the resonances and obtained the partial widths, the radiative kernels could be calculated, and are listed in Table 5.1 for the 116 resonances fitted in the current work. The kernels for the three latest evaluations are also listed, as are the ratios of the current work to the three evaluations. Where ENDF/B-VII.1 lists parameters for 116 resonances, JENDL-4.0 lists 115 and JEFF-3.2 lists 94. Missing resonances are denoted with a dash.

Table 5.1: List of the ^{236}U *radiative capture kernels and the statistical errors for each resonance for the current work (TAC), and for the ENDF/B-VII.1, JEFF-3.2 and JENDL-4.0 evaluations. Also listed are the kernel ratios of the current work to the different libraries. Listed energies are those of the ENDF/B-VII.1 evaluation. The spin factor* $g_s = 1$ *for all resonances. Superscript 'p' denotes p-waves as designated in the ENDF/B-VII.1 evaluation.*

Energy (eV)	Radiative Kernels (meV)					Kernel Ratios		
	This Work	$\frac{\Delta RK}{RK}$ (%)	ENDF	JEFF	JENDL	$\frac{\text{This Work}}{\text{ENDF}}$	$\frac{\text{This Work}}{\text{JEFF}}$	$\frac{\text{This Work}}{\text{JENDL}}$
5.45	1.53	0.1	2.05	1.98	2.10	0.75	0.77	0.73
29.80	0.58	0.3	0.39	0.57	0.35	1.50	1.00	1.60
34.10	2.01	0.1	1.35	2.15	1.16	1.50	0.94	1.70
43.91	8.78	0.1	7.05	9.16	6.99	1.20	1.00	1.30
64.29^p	0.03	7.7	0.03	0.04	0.02	1.00	0.91	2.00
71.47	11.6	0.2	10.1	11.5	9.80	1.10	1.00	1.20
86.51	13.5	0.2	10.9	12.9	11.7	1.20	1.00	1.20
102.30	0.78	1.2	0.58	0.85	0.56	1.30	0.92	1.40
120.95	16.8	0.2	13.6	14.8	15.5	1.20	1.10	1.10
124.88	10.0	0.2	7.81	8.97	8.78	1.30	1.10	1.10
134.57	1.02	1.4	0.87	1.14	0.70	1.20	0.89	1.50
137.76	0.52	2.4	0.48	0.56	0.46	1.10	0.94	1.10

continued ...

... continued

Energy	This Work	$\frac{\Delta RK}{RK}$ (%)	ENDF	JEFF	JENDL	$\frac{\text{This Work}}{\text{ENDF}}$	$\frac{\text{This Work}}{\text{JEFF}}$	$\frac{\text{This Work}}{\text{JENDL}}$
164.72	1.84	1.2	1.61	1.92	1.42	1.10	1.00	1.30
192.89	7.14	0.4	3.05	6.67	5.21	2.30	1.10	1.40
194.35	17.9	0.3	13.1	14.9	15.7	1.40	1.20	1.10
212.75	19.8	0.4	17.0	18.5	19.3	1.20	1.10	1.00
229.63	1.88	1.8	1.58	1.84	1.47	1.20	1.00	1.30
243.00^p	0.18	13	0.12	-	0.11	1.60	-	1.60
272.93	14.9	0.6	12.7	14.5	13.4	1.20	1.00	1.10
288.68	8.54	0.8	5.83	9.10	6.88	1.50	0.94	1.20
303.15	19.4	0.6	16.8	17.3	20.0	1.20	1.10	1.00
320.50	4.47	1.7	3.76	4.44	3.65	1.20	1.00	1.20
334.96	5.02	2.1	3.96	5.01	3.86	1.30	1.00	1.30
357.05^p	0.51	11	0.42	0.68	0.38	1.20	0.75	1.40
366.95^p	0.51	8.5	0.34	0.39	0.34	1.50	1.30	1.50
371.18	10.1	0.8	7.16	9.53	8.20	1.40	1.10	1.20
379.80	20.6	0.8	16.5	18.5	19.5	1.30	1.10	1.10
415.39	9.98	1.0	8.04	9.81	8.99	1.20	1.00	1.10
430.95	17.1	0.9	14.9	16.4	16.6	1.20	1.00	1.00
440.63	17.8	0.8	16.2	17.7	18.1	1.10	1.00	1.00
466.50	8.59	1.5	7.70	8.30	8.55	1.10	1.00	1.00
478.39	14.0	1.1	12.4	13.8	14.3	1.10	1.00	1.00
500.40	2.17	4.0	1.94	2.50	1.90	1.10	0.87	1.10
507.10	10.4	1.3	8.45	10.5	9.74	1.20	1.00	1.10
536.40	12.3	1.1	11.0	13.2	12.8	1.10	0.93	1.00
542.80	6.98	1.8	5.48	8.87	6.30	1.30	0.80	1.10
564.40	19.0	1.1	16.6	17.3	19.6	1.10	1.10	1.00
576.20	21.9	1.1	19.8	22.3	24.1	1.10	1.00	0.91
607.10	8.57	2.0	7.09	7.88	7.84	1.20	1.10	1.10

continued ...

... continued

Energy	This Work	$\frac{\Delta RK}{RK}$ (%)	ENDF	JEFF	JENDL	$\frac{\text{This Work}}{\text{ENDF}}$	$\frac{\text{This Work}}{\text{JEFF}}$	$\frac{\text{This Work}}{\text{JENDL}}$
617.80	16.7	1.3	13.9	16.5	16.8	1.20	1.00	1.00
637.80	19.3	1.3	15.8	18.1	19.1	1.20	1.10	1.00
647.60	5.23	2.9	4.56	5.37	4.91	1.10	1.00	1.10
655.60	20.1	1.3	18.4	18.7	20.6	1.10	1.10	1.00
673.60	17.7	1.6	14.0	16.7	17.0	1.30	1.10	1.00
691.30	13.2	1.8	11.4	15.8	13.5	1.20	0.80	1.00
706.00	12.6	2.0	12.2	12.7	13.8	1.00	1.00	0.91
720.60	19.1	1.8	16.7	17.5	20.2	1.10	1.10	0.95
746.30	11.0	2.5	9.35	10.3	10.9	1.20	1.10	1.00
770.70	21.5	1.9	19.7	19.7	24.2	1.10	1.10	0.89
789.40	18.5	1.9	16.5	18.2	19.9	1.10	1.00	0.93
806.60	14.4	2.2	13.0	15.3	15.0	1.10	0.94	1.00
820.30	5.77	4.0	4.61	6.15	5.56	1.30	0.94	1.00
827.40	22.9	1.6	22.3	25.3	24.2	1.00	0.91	0.95
832.0^p	0.55	14	0.50	-	0.47	1.10	-	1.20
849.0^p	2.89	8.5	2.39	1.84	2.46	1.20	1.60	1.20
864.90	9.89	3.3	8.41	9.24	-	1.20	1.10	-
869.7^p	0.47	36	0.50	-	0.47	0.94	-	1.00
888.80	6.84	4.2	5.75	6.97	6.29	1.20	1.00	1.10
900.40	5.54	5.1	4.78	6.47	5.27	1.20	0.86	1.10
930.70	6.41	4.9	4.99	7.44	5.66	1.30	0.86	1.10
940.4^p	0.64	23	0.70	-	0.67	0.91	-	1.00
948.50	21.3	1.9	20.8	21.0	22.9	1.00	1.00	0.93
955.20	13.7	2.4	12.4	14.6	14.8	1.10	0.94	0.93
969.30	23.3	2.4	21.4	21.6	26.4	1.10	1.10	0.88
994.70	20.8	2.1	19.2	19.2	23.5	1.10	1.10	0.88
998.10	7.56	4.0	5.42	7.44	6.68	1.40	1.00	1.10

continued ...

... continued

Energy	This Work	$\frac{\Delta RK}{RK}$ (%)	ENDF	JEFF	JENDL	$\frac{\text{This Work}}{\text{ENDF}}$	$\frac{\text{This Work}}{\text{JEFF}}$	$\frac{\text{This Work}}{\text{JENDL}}$
1007.8^p	0.77	18	0.60	-	0.62	1.30	-	1.30
1013.1	7.51	4.3	5.17	7.44	6.81	1.50	1.00	1.10
1024.2	23.0	2.1	23.9	24.3	26.1	1.00	0.95	0.88
1032.1	15.0	2.7	12.3	17.0	15.3	1.20	0.89	1.00
1051.9^p	0.51	39	0.61	-	0.61	0.84	-	0.84
1064.6	15.9	3.0	15.9	17.3	15.6	1.00	0.92	1.00
1075.7^p	4.33	7.9	3.55	4.76	3.71	1.20	0.91	1.20
1084.2^p	1.53	16	1.21	1.84	1.18	1.30	0.83	1.30
1093.0^p	0.75	42	0.60	-	0.64	1.30	-	1.20
1098.0^p	2.24	12	1.62	2.65	1.64	1.40	0.85	1.40
1104.8	19.0	3.0	20.0	20.8	21.8	0.95	0.91	0.87
1125.7^p	0.98	21	0.90	-	0.93	1.10	-	1.10
1132.1	6.01	5.1	5.45	7.44	5.76	1.10	0.81	1.00
1136.7	19.1	2.6	16.9	18.1	20.8	1.10	1.10	0.92
1151.4^p	0.90	25	0.91	-	0.92	1.00	-	1.00
1157.1	15.2	2.7	13.8	18.1	17.5	1.10	0.84	0.87
1166.9	6.28	6.2	4.97	7.44	5.27	1.30	0.84	1.20
1170.3^p	0.85	25	1.01	-	1.02	0.84	-	0.83
1184.0	17.6	3.0	14.7	18.6	18.1	1.20	0.95	1.00
1191.2^p	1.22	20	1.10	-	1.16	1.10	-	1.10
1196.6^p	2.07	13	2.10	-	2.17	1.00	-	1.00
1206.8^p	0.73	37	0.80	-	0.76	0.92	-	1.00
1218.6	6.01	7.4	5.29	6.21	5.85	1.10	1.00	1.00
1254.3^p	5.55	8.0	4.20	5.66	4.99	1.30	1.00	1.10
1268.8^p	4.93	8.8	3.66	4.76	3.82	1.30	1.00	1.30
1273.2^p	1.39	20	0.80	-	0.83	1.70	-	1.70
1281.7^p	2.89	12	2.41	2.65	2.62	1.20	1.10	1.10

continued ...

... continued

Energy	This Work	$\frac{\Delta RK}{RK}$ (%)	ENDF	JEFF	JENDL	$\frac{\text{This Work}}{\text{ENDF}}$	$\frac{\text{This Work}}{\text{JEFF}}$	$\frac{\text{This Work}}{\text{JENDL}}$
1288.1^p	1.48	14	1.02	-	1.01	1.50	-	1.50
1291.7	20.8	2.5	23.9	25.8	23.3	0.87	0.81	0.90
1297.3^p	1.41	21	1.10	-	1.15	1.30	-	1.20
1315.9^p	2.68	13	2.63	3.41	2.64	1.00	0.79	1.00
1324.4	8.45	5.8	6.94	9.08	8.94	1.20	0.93	0.90
1339.5	18.2	3.3	15.3	18.2	18.8	1.20	1.00	1.00
1349.2	18.9	3.1	19.0	21.9	19.2	1.00	0.86	1.00
1353.5^p	0.66	28	0.91	-	0.92	0.72	-	0.72
1363.6	20.6	3.0	24.5	25.8	25.0	0.84	0.80	0.82
1367.4^p	5.02	8.0	3.59	3.41	3.75	1.40	1.50	1.30
1379.3^p	0.75	41	0.60	-	0.62	1.20	-	1.20
1395.6	12.5	4.2	10.6	11.0	13.4	1.20	1.10	0.93
1405.0	15.3	3.6	14.0	15.8	17.2	1.10	1.00	0.89
1413.4	23.6	2.9	19.5	19.5	26.3	1.20	1.20	0.89
1426.6	11.0	5.4	9.60	12.2	12.0	1.10	0.91	0.92
1437.6^p	1.25	20	1.20	-	1.17	1.00	-	1.10
1440.4^p	4.50	9.6	3.40	3.41	3.57	1.30	1.30	1.30
1450.6^p	2.10	40	1.00	-	1.04	2.10	-	2.00
1458.3	8.27	6.3	6.41	8.70	8.00	1.30	0.95	1.00
1470.0	23.3	3.1	23.6	23.9	25.3	1.00	1.00	0.92
1477.1	12.1	5.2	11.1	13.2	13.0	1.10	0.91	0.92
1489.3^p	2.24	20	1.32	-	1.34	1.70	-	1.70
1495.2^p	0.89	36	0.71	-	0.68	1.30	-	1.30

To calculate the radiative kernel, RK:

$$RK = g_J \frac{\Gamma_n \Gamma\gamma}{\Gamma_n + \Gamma_\gamma} \tag{5.2}$$

it was necessary to determine the statistical spin factor, g:

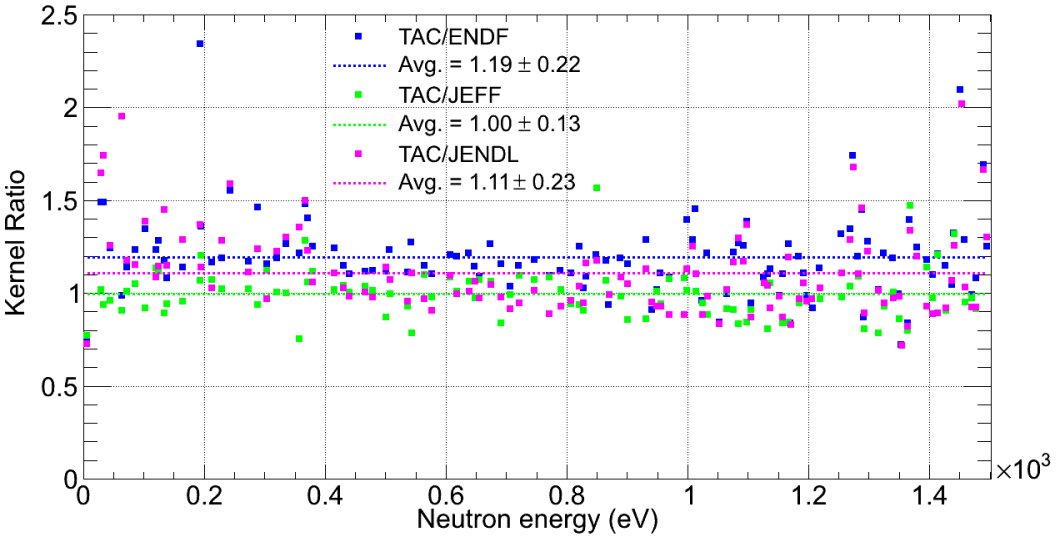

Figure 5.18: Plot of the kernel ratios of the current work with those of ENDF, JEFF and JENDL. The error in the kernels of the current work is ≈ 5%.

$$g_J = \frac{2J+1}{(2i+1)(2I+1)} \tag{5.3}$$

for each resonance. Given $i = 1/2^+$ for the neutron and for an even-even nuclei like ^{236}U $I = 0^+$ in the ground state, the g-factor is calculated for each resonance, based on the spin assignment for J provided for each resonance in a given library. These are not necessarily the same, but every resonance in the 1-1500 eV region has J = 1/2 for both s- and p-wave resonances, making the spin g_s factor 1 in every case.

5.2 Discussion Of The Results

As already discussed above and illustrated in Figure 5.17, differences were found between the resonances of current work and the evaluations in the energy, strength and kernels of individual resonances. Notably, the kernel of the 5.45 eV resonance of the current work is 25% lower than the three evaluations.

To quantify the differences between the kernels of the current work and the evaluations, the kernel ratios are illustrated as function of the resonance energy in Figure 5.18.

The average ratios show the ENDF radiative kernels to be 20% smaller than the current work, and demonstrating a large spread of values around the mean value of the ratio. The JENDL kernels are on average 10% smaller and also showing a large

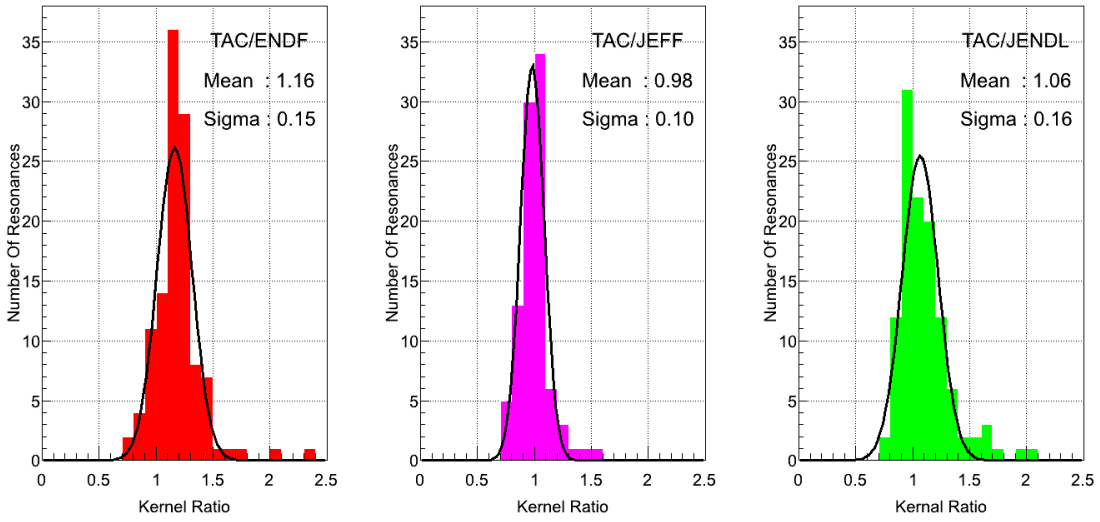

Figure 5.19: Projection of the y-axis of Figure 5.18 showing the spread of the kernel ratios of the current work to ENDF, JEFF and JENDL, about their respective mean values

spread about the mean ratio. The best agreement comes with the JEFF evaluation, which agree on average. The biggest differences with the current work come from the resonances with sizeable multiple scattering and the p-wave resonances which have more limited statistics. As the JEFF evaluation is missing many of the p-wave resonances in ENDF and JENDL, the average ratio and spread of the ratios was determined with the ENDF and JENDL evaluations by omitting the p-wave resonances, but this was not found to significantly change from the ratios and spreads including the p-wave resonances.

To quantify the differences more clearly, the projection of the y-axis of Figure 5.18 was taken and is shown in Figure 5.19. For each of the three evaluations, the projections show the spread of the ratios about the mean.
These projections show that overall the kernels of the current work are 16% larger than ENDF, 2% smaller than JEFF and 6% larger than JENDL. Within the accuracy of the current work of 5%, the current work shows good agreement with JEFF, and is reasonable agreement with JENDL. However, a large discrepancy exists with the ENDF evaluation.

It was seen in Section 4.7 that the uncertainty in the current work varies from 2.3% in the best case, for resonances with little scattering contribution or pile-up, up to 5.3% in the worst case for resonances with large pile-up and scattering contributions. As good fits to the majority of resonances were found (excluding

5 resonances at low energy where strong multiple scattering exists), reliable new determinations of the radiative capture kernels for the ^{236}U(n, γ) reaction have been made to within the requested accuracy of 10%, in fact achieving the desired 5%.

Large differences have been found with individual resonances in different libraries, often differing from the current work by 10-30%, and in a few extreme cases by a factor of 2 or more. The new accurate data obtained at the CERN n_TOF facility will result in valuable new data becoming available to the nuclear community, of importance for the thorium fuel cycle for future reactors.

The discrepancy between the different libraries originates in the data which is used as the basis for the evaluations. For the case of JEFF-3.2 (2014), the data of Carraro (1975) [25] and Mewisson (1975) [26] were used for the resonance parameters. For neutron widths $\Gamma_n > \Gamma_\gamma/10$ the parameters of Carraro were taken, and for $\Gamma_n < \Gamma_\gamma/10$ the parameters of Mewisson were taken. For capture widths, the values from Mewisson where used, and for resonances where capture widths were not given, the average value was used. The work of Mewisson was based on capture, scattering and total cross sections measurements covering 30-1800 eV. They reported 97 neutron widths and 57 capture widths, meaning 40 resonances were simply assigned the average Γ_γ. As the capture and neutron widths of the current work cannot be determined, it is not possible to see if their average values are similar, possibly giving rise to radiative kernels that agree with the JEFF-3.2 data within the difference seen in Figure 5.19. The work of Cararro was based on transmission experiments, and extended the Mewisson data covering 40-4100 eV.

For ENDF/B-VII.1 (2011) the work of Alexander (1989) [27] was used over the energy range from 20 eV to 1500 eV with an uncertainty in this range of $< 5\%$, similar to the current work. Over the range 20 eV to 1 MeV, the work of Alexander found approximately 100 more resonances than the work of Carraro, and is the reason why there are more resonances in the ENDF evaluation (116 resonances) than in JEFF (94 resonances).

JENDL-4.0 (2010) also used the work of [27], except for the p-wave resonances where the values of [25] were used. The resonances in the JENDL evaluation then had their capture widths adjusted so that the capture cross sections matched those of Adamchuk (1988) [28] and the more recent work of Muradyan (2011) [29].

Thus given the evaluations were based on different data and treated in different ways, it seems reasonable to assume that is the reason for the difference between the ratios of the current work to ENDF, JEFF and JENDL, and between the libraries them selves.

As there is little data available for the evaluators, their different choices have had a marked impact on the capture and partial widths reported in the various evaluated data libraries, which are based on work done primarily in the 1970's and 1980's, pointing to the need for more, accurate nuclear cross section data for ^{236}U.

Chapter 6

Conclusions And Outlook

This manuscript has detailed the successful measurement and subsequent analysis of the ^{236}U(n, γ) radiative capture kernels in the resonance region, of importance to the thorium fuel cycle.

With the world in the midst of an energy crisis, and the effects of global warming brought about by a dependence on fossil fuels having a detrimental effect on the worlds environment, alternative sources of energy are required. Nuclear power stations, with their zero carbon emissions, offer an attractive alternative to fossil fuels, and studies in to future nuclear reactors are under way. The Generation IV International Forum (GIF) is one such international endeavour to look at the feasibility of novel future reactor designs offering a reduced radioactive inventory when compared to the current suite of nuclear reactors, whilst at the same time offering fuel reserves that will power humanity beyond peak oil and peak coal. Research into Accelerator Driven Systems (ADS) would give the ability to burn nuclear waste from reactors, further reducing the radioactive inventory that will be left as a legacy for future generations. These are possibilities that may come to fruition in the next 20 to 30 years. New reactors would not just use ^{235}U as do conventional nuclear reactors, but could make use of alternative fuel cycles based on thorium, which offers the benefit of being three times as abundant as uranium in the Earth's crust, and, due to its lower mass number, would result in the production of less transuranic waste (TRUW) than the conventional ^{235}U fuel cycle.

At the current time, nuclear cross section data on isotopes of relevance to the thorium fuel cycle is lacking, and what data do exist, in libraries such as ENDF, JEFF and JENDL, show discrepancies between resonance strengths and energies. In particular, one such reaction, ^{236}U(n, γ), which is of importance as being the

site of the build up of transuranic elements (TRU) in the thorium fuel cycle, shows disagreements in resonance strengths of up to 40% in the different libraries, on average differing from one another by 8 to 20%, according to figure 5.17.

To this end, an experiment to determine the ^{236}U(n, γ) capture kernels was performed at the CERN n_TOF facility, with an aim to measure it within the requested accuracy of 10%, and with a goal to measure them to 5%, using the time-of-flight technique.

Making use of the convenient features of the fully digital DAQ, the high instantaneous neutron flux available at n_TOF, and the powerful background rejection capabilities offered by the BaF_2 Total Absorption Calorimeter (TAC) owing to its near 4π solid angle coverage and high segmentation, and with a high purity (99.85%) ^{236}U sample, the goal of determining the kernels to 5% has been achieved.

The C++ based ROOT programming language was used extensively by the author in order to extract the capture yield from the raw data taken with the TAC. This manuscript has detailed all the steps in this analysis in going from raw data to capture yield. From how the data was quality checked and how, via dedicated measurements, the different sources of background were accounted for and subtracted. Further, the neutron sensitivity (or scattering) background was quantified so that the systematic uncertainty of this source, which changes from resonance to resonance, could be determined. It was seen that for the majority of resonances, the uncertainty due to scattered neutrons was negligible, rising to a maximum of 4%. The other sources of systematic uncertainty in the current work due to sample mass (1.5%), background subtractions (0%), and flux (1-2%), have also been determined and discussed.

Due to the high counting rates seen in the detector leading to dead-time and pile-up losses, the application of a novel technique developed within the n_TOF collaboration was applied to the data. Having two different pulse intensities available, namely the TOF and EAST pulses (average pulse intensities of 7×10^{12} and 3×10^{12}), allowed the agreement between these different data sets to be compared after pile-up corrections had been applied. This allowed the determination of the uncertainty associated with these corrections, which was found to be between zero and 2%, depending on the resonance.

Having extracted the capture yield, the R-matrix code SAMMY, developed at the Oak Ridge National Laboratory, was used by the author to analyse the capture yield and obtain the resonance parameters from which the radiative kernels, the goal of the current work, have been obtained. SAMMY was first used in order to

normalise the yield at the 5.45 eV saturated resonance making use of the saturated resonance technique. The uncertainty in the normalisation was studied and was shown to be 1.5%. SAMMY allows all experimental effects to be accounted for, such as the sample dimensions, Doppler broadening model to be used, and the effect of the resolution function specific to the n_TOF facility. Over the range of the resolved resonance region (RRR) from 1 to 1500 eV, 116 resonances were fitted with SAMMY, and their resonances parameters extracted, enabling the determination of the radiative kernels which are a necessary ingredient to determine the cross section. To determine the capture and neutron widths accurately requires the combination of data from capture and transmission experiments. This was not performed, and thus this work lists the measured radiative kernels.

Having successfully extracted the radiative kernels up to 1500 eV and accounted for all sources of uncertainty, is was possible to quantify the total uncertainty in the current work. The radiative kernels were determined to have uncertainties ranging from 2.3% for resonances with little scattering and pile-up to 5.3% for resonances with more significant scattering and pile-up effects, and thus achieving the requested accuracy of 10% and even reaching the desired 5%.

Looking to the future, given the good statistics obtained in the current work, it would be possible to extend the analysis of the RRR beyond 1.5 keV, which is the limit of the RRR in the ENDF and JEFF evaluations. The JENDL evaluation goes to 4 keV and it may be possible to reach this, and possibly extend past it. A full comparison with the work of Barbagallo et al. [59], also performed at the n_TOF facility, and possibly a combination of the two data sets could be performed, with the hope of improving the quality of the data further. By combining the current results with transmission data, this may allow for the accurate determination of the resonance parameters, Γ_γ and Γ_n. Finally, the ^{235}U and ^{238}U impurities present in the sample were not included. Given the high purity of the sample, they would not significantly impact the current results. However, if included, would allow to determine if some of the features in the yield which were not fitted are indeed impurities, or if they are undiscovered ^{236}U resonances.

Given the limited data available for this reaction, it is of value to be able to contribute the results of the current work to the nuclear data community to bolster the information currently available for the ^{236}U neutron capture cross section. Our cross section is in overall agreement with JEFF-3.2 (TAC/JEFF ratio of 0.98 ± 0.10), 6% larger than JENDL-4.0 (ratio of 1.06 ± 0.16) and quite larger than ENDF/B-VII.1 (ratio of 1.16 ± 0.15). These are sizeable differences considering our accuracy

of just 2-5%, suggesting that some revision of the libraries may be in order.

APPENDIX

Appendix A

^{236}U Resonance Parameters

Table A.1: List of the neutron and capture widths determined with SAMMY and used for the calculation of the radiative kernels for the current work. The neutron and capture widths from the ENDF/B-VII.1, JEFF-3.2 and JENDL-4.0 libraries are listed for comparison.

Energy	Partial Widths (meV)							
	This Work		ENDF/B-VII.1		JEFF-3.2		JENDL-4.0	
(eV)	Γ_γ	Γ_n	Γ_γ	Γ_n	Γ_γ	Γ_n	Γ_γ	Γ_n
5.45	35.5	1.60	24.5	2.24	24.5	2.16	24.5	2.30
29.80	33.3	0.59	19.5	0.40	23.0	0.59	22.2	0.36
34.10	39.6	2.12	19.5	1.45	20.9	2.40	22.2	1.22
43.91	24.1	13.8	13.0	15.4	19.2	17.5	13.0	15.1
64.29	16.3	0.03	19.5	0.03	23.0	0.04	22.2	0.02
71.47	23.6	22.7	21.0	19.6	22.0	24.0	19.6	19.7
86.51	23.6	31.4	17.8	28.3	20.0	36.0	20.0	28.1
102.30	56.9	0.79	19.5	0.60	23.0	0.88	22.2	0.58
120.95	24.4	53.9	18.9	48.3	20.0	57.0	23.3	46.3
124.88	18.7	21.6	14.3	17.2	19.0	17.0	17.4	17.7
134.57	76.9	1.03	19.5	0.91	23.0	1.20	22.2	0.73
137.76	37.9	0.53	19.5	0.50	23.0	0.57	22.2	0.47
164.72	39.0	1.93	19.5	1.75	23.0	2.10	22.2	1.52
192.89	11.1	20.0	19.0	3.63	23.0	9.40	22.2	6.81

continued ...

... continued

Energy	This Work		ENDF/B-VII.1		JEFF-3.2		JENDL-4.0	
(eV)	Γ_γ	Γ_n	Γ_γ	Γ_n	Γ_γ	Γ_n	Γ_γ	Γ_n
194.35	25.1	62.3	18.4	46.0	20.0	58.0	23.3	48.5
212.75	24.7	101	21.1	86.6	22.8	98.0	24.8	86.2
229.63	73.2	1.93	19.5	1.72	23.0	2.00	22.2	1.57
243.00	269	0.18	19.5	0.12	-	-	22.2	0.12
272.93	22.1	45.7	21.7	30.7	23.5	38.0	24.3	29.7
288.68	13.6	22.9	12.7	10.8	25.0	14.3	22.2	10.0
303.15	24.6	91.2	21.3	78.5	22.0	81.0	26.7	79.7
320.50	43.7	4.98	19.5	4.66	23.0	5.50	22.2	4.37
334.96	24.1	6.34	19.5	4.97	23.0	6.40	22.2	4.67
357.05	113	0.51	19.5	0.43	23.0	0.70	22.2	0.38
366.95	229	0.51	19.5	0.35	23.0	0.40	22.2	0.34
371.18	16.1	27.0	16.5	12.7	24.0	15.8	22.2	13.0
379.80	24.9	120	20.0	93.1	22.0	115	24.6	94.3
415.39	14.9	30.2	16.7	15.5	22.0	17.7	22.2	15.1
430.95	22.3	73.4	20.1	57.2	22.0	65.0	24.3	52.5
440.63	23.3	76.0	22.1	60.1	24.0	68.0	26.8	56.3
466.50	81.3	9.60	17.0	14.1	18.0	15.4	22.2	13.9
478.39	20.5	44.0	18.9	36.4	21.0	40.0	23.0	37.9
500.40	28.4	2.35	19.5	2.16	23.0	2.80	22.2	2.08
507.10	15.7	31.4	16.2	17.7	22.0	20.0	19.9	19.1
536.40	70.5	14.9	17.6	29.4	22.0	33.0	21.6	31.5
542.80	58.8	7.92	13.6	9.17	30.0	12.6	22.2	8.79
564.40	24.3	87.2	21.1	77.4	22.0	81.0	26.7	74.4
576.20	25.4	158	22.8	152	26.0	158	28.5	156
607.10	19.0	15.6	15.4	13.1	20.0	13.0	22.2	12.1
617.80	22.1	67.8	20.7	42.5	24.0	53.0	24.7	52.3
637.80	24.2	94.1	20.9	65.2	24.0	74.0	25.5	76.0

continued ...

... continued

Energy	This Work		ENDF/B-VII.1		JEFF-3.2		JENDL-4.0	
(eV)	Γ_γ	Γ_n	Γ_γ	Γ_n	Γ_γ	Γ_n	Γ_γ	Γ_n
647.60	58.9	5.74	18.7	6.03	23.0	7.00	22.2	6.30
655.60	24.4	116	23.0	93.1	23.0	101	26.1	98.0
673.60	21.6	98.3	19.6	48.6	24.0	54.5	24.3	56.0
691.30	22.1	32.9	18.8	29.1	27.0	38.0	23.1	32.4
706.00	38.7	18.6	21.0	28.8	21.0	32.0	26.3	28.9
720.60	22.9	116	20.1	97.4	21.0	105	25.5	97.7
746.30	36.6	15.8	17.5	20.1	18.0	24.0	22.9	20.8
770.70	24.2	189	22.0	184	22.0	192	27.8	185
789.40	23.0	95.0	20.7	81.2	23.0	87.0	26.0	85.5
806.60	78.1	17.7	20.0	37.1	24.0	42.0	24.6	38.8
820.30	27.1	7.33	12.3	7.38	23.0	8.40	22.2	7.41
827.40	25.2	247	28.0	109	28.0	259	26.9	240
832.02	25.3	0.6	19.5	0.51	-	-	22.2	0.5
849.00	388	2.91	19.5	2.72	23.0	2.00	22.2	2.8
864.90	28.7	15.1	17.1	16.5	19.0	18.0	-	-
869.74	21.6	0.48	19.5	0.51	-	-	22.2	0.48
888.80	32.9	8.63	19.5	8.16	23.0	10.0	22.2	8.77
900.40	31.0	6.75	19.5	6.33	23.0	9.00	22.2	6.91
930.70	46.6	7.44	15.7	7.31	23.0	11.0	22.2	7.60
940.41	26.7	0.66	24.0	0.73	-	-	22.2	0.70
948.50	24.1	177	24.0	157	24.0	170	26.7	163
955.20	34.5	22.8	18.8	36.4	23.0	40.0	24.4	37.5
969.30	24.9	365	23.0	316	23.0	359	28.7	319
994.70	23.6	173	22.0	152	22.0	153	27.8	152
998.10	164	7.93	13.7	8.97	23.0	11.0	22.2	9.55
1007.80	19.2	0.81	19.5	0.62	-	-	22.2	0.63
1013.10	18.2	12.8	10.6	10.08	23.0	11.0	22.2	9.82

continued ...

... continued

Energy	This Work		ENDF/B-VII.1		JEFF-3.2		JENDL-4.0	
(eV)	Γ_γ	Γ_n	Γ_γ	Γ_n	Γ_γ	Γ_n	Γ_γ	Γ_n
1024.20	25.0	288	26.5	249	26.5	298	29.1	249
1032.10	28.9	31.3	20.4	31.3	28.0	43.0	25.9	37.5
1051.90	30.6	0.52	29.0	0.62	-	-	22.2	0.63
1064.60	20.2	73.8	29.0	35.2	29.0	43.0	26.7	37.5
1075.70	22.2	5.38	19.5	4.33	23.0	6.00	22.2	4.46
1084.20	26.9	1.63	19.5	1.29	23.0	2.00	22.2	1.25
1093.00	20.8	0.78	19.5	0.62	-	-	22.2	0.66
1098.00	48.0	2.35	19.5	1.76	23.0	3.00	22.2	1.77
1104.80	23.6	96.0	25.0	100	25.0	124	26.5	123
1125.70	20.5	1.03	19.5	0.94	-	-	22.2	0.97
1132.10	33.5	7.32	19.5	7.57	23.0	11.0	22.2	7.78
1136.70	22.7	122	19.8	115	21.5	116	25.2	118
1151.40	24.4	0.94	26.0	0.94	-	-	22.2	0.96
1157.10	35.3	26.8	20.2	43.4	26.0	60.0	24.6	61.0
1166.90	32.4	7.79	19.5	6.66	23.0	11.0	22.2	6.91
1170.30	30.4	0.87	25.0	1.05	-	-	22.2	1.07
1184.00	22.0	87.6	20.6	50.9	25.0	72.0	25.5	63.0
1191.20	50.0	1.25	19.5	1.17	-	-	22.2	1.22
1196.60	16.2	2.37	19.5	2.35	-	-	22.2	2.40
1206.80	19.5	0.76	19.5	0.83	-	-	22.2	0.79
1218.60	36.0	7.21	19.5	7.26	23.0	8.50	22.2	7.94
1254.30	16.4	8.39	12.6	6.31	23.0	7.50	22.2	6.44
1268.80	25.7	6.09	19.5	4.50	23.0	6.00	22.2	4.61
1273.20	23.6	1.48	19.5	0.83	-	-	22.2	0.86
1281.70	18.8	3.42	15.0	2.87	23.0	3.00	22.2	2.97
1288.10	31.2	1.55	30.5	1.05	-	-	22.2	1.06
1291.70	23.5	184	30.5	110	30.5	168	27.2	165

continued ...

. . . continued

Energy	This Work		ENDF/B-VII.1		JEFF-3.2		JENDL-4.0	
(eV)	Γ_γ	Γ_n	Γ_γ	Γ_n	Γ_γ	Γ_n	Γ_γ	Γ_n
1297.30	18.7	1.52	19.5	1.17	-	-	22.2	1.21
1315.90	26.1	2.99	19.5	3.04	23.0	4.00	22.2	3.00
1324.40	24.0	13.0	14.4	13.4	23.0	15.0	18.9	17.0
1339.50	25.4	64.6	20.4	61.6	24.0	75.0	25.6	70.0
1349.20	22.3	123	32.0	46.6	32.0	69.0	29.3	56.0
1353.50	20.9	0.68	29.0	0.94	-	-	22.2	0.96
1363.60	23.8	151	29.0	157	29.0	230	28.2	221
1367.40	23.8	6.36	19.5	4.40	23.0	4.00	22.2	4.51
1379.30	21.7	0.78	19.5	0.62	-	-	22.2	0.64
1395.60	30.6	21.1	19.5	23.1	23.0	21.0	22.2	33.9
1405.00	38.1	25.6	19.5	49.1	23.0	50.0	29.1	42.0
1413.40	26.4	221	21.0	264	21.0	275	29.3	264
1426.60	27.4	18.5	16.7	22.7	23.0	26.0	21.7	27.0
1437.60	18.3	1.34	19.5	1.28	-	-	22.2	1.24
1440.40	18.0	6.00	19.5	4.11	23.0	4.00	22.2	4.26
1450.60	40.9	2.21	19.5	1.05	-	-	22.2	1.09
1458.30	21.1	13.6	13.8	12.0	23.0	14.0	22.2	12.5
1470.00	25.4	289	27.0	185	27.0	212	28.7	212
1477.10	29.6	20.3	18.9	27.2	23.0	31.0	24.4	28.0
1489.30	50.4	2.34	26.0	1.39	-	-	22.2	1.43
1495.20	27.4	0.92	26.0	0.73	-	-	22.2	0.70

Bibliography

[1] World Energy Council. World energy perspective: Cost of energy technologies, 2013.

[2] IPCC. *Summary for Policymakers*, book section SPM, page 1–30. Cambridge University Press, Cambridge, United Kingdom and New York, NY, USA, 2013.

[3] House Of Commons Environmental Audit Committee. *Keeping the lights on: Nuclear, Renewables and Climate Change*, volume 2. London: The Stationery Office Limited, April 2006.

[4] G. Maggio and G. Cacciola. When will oil, natural gas, and coal peak? *Fuel*, 98:112–113, 2012.

[5] World Nuclear Association (WNA). `http://www.world-nuclear.org`, 2001. [Online; accessed November-2014].

[6] OECD NEA/IAEA. Uranium 2011: Resources, production and demand, 2012.

[7] Bernard L. Cohen. Breeder reactors: A renewable energy source. *Am. J. Phys.*, 51:1, 1983.

[8] Atomic Archive. `www.atomicarchive.com`. [Online; accessed Nov-2014].

[9] ITER. `http://www.iter.org/`. [Online; accessed Oct-2014].

[10] Strategic Energy Technologies Information System. `https://setis.ec.europa.eu/`. [Online; accessed Nov-2014].

[11] International Atomic Energy Agency (IAEA). `https://www.iaea.org`. [Online; accessed Feb-2015].

[12] Generation IV International Forum (GIF). `https://www.gen-4.org/gif/jcms/c_9260/public`. [Online; accessed Nov-2014].

[13] Thor Energy. `http://www.thorenergy.no/`. [Online; accessed Nov-2014].

[14] Nuclear Regulatory Commission (NRC). `http://www.nrc.gov/`. [Online; accessed Nov-2014].

[15] National Physics Laboratory (NPL). `http://www.kayelaby.npl.co.uk/`. [Online; accessed Nov-2014].

[16] Nuclear Energy Agency (NEA). JANIS 4.0. `http://www.oecd-nea.org/janis/`, 2008. [Online; accessed November-2014].

[17] Department of Climate Change and Energy. Implementing geological disposal, 2014.

[18] National Nuclear Data Center (NNDC). ENDF. `http://www.nndc.bnl.gov/exfor/endf00.jsp`. Evaluated Nuclear Data File.

[19] Nuclear Energy Agency (NEA). JEFF. `http://www.oecd-nea.org/dbdata/`. Joint European Fission and Fusion File.

[20] Japan Atomic Energy Agency (JAEA). JENDL. `http://wwwndc.jaea.go.jp/jendl/j40/j40.html`. Japanese Evaluated Nuclear Data File.

[21] Russian Nuclear data Centre (Centr Jadernykh Dannykh-CJD). BROND. `www.ippe.obninsk.ru/podr/cjd/`.

[22] Z. G. Ge *et al.* The updated version of chinese evaluated nuclear data library (CENDL-3.1). *J. Korean Phys. Soc.*, 59:1052–1056, 2011.

[23] IAEA Nuclear Data Services (NDS). `https://www-nds.iaea.org`. [Online; accessed Nov-2014].

[24] Carlson *et al.* The u-236 neutron capture capture cross section. *Nuclear Physics A*, 141:577–594, 1970.

[25] G. Carraro and A. Brusegan. Total neutron cross-section measurements of ^{236}Uin the energy range 40 ev to 4.1 kev. *Nucl. Sci. And Eng.*, 104:258–270, 1975.

[26] L. Mewissen and F. Poortmans *et al.* Neutron cross-section measurement on ^{236}U. *Proc. Conf. Nuclear Cross Sections and Technology*, 4:729, 1975.

[27] C. W. Alexander R. L. Macklin. Neutron absorption cross section of ^{236}U. *Nucl. Sci. And Eng.*, 104:258–270, 1989.

[28] Yu.V.Adamchuk *et al.* ^{236}Uand ^{238}Uradiative-capture cross sections for neutron energies from 10 ev to 50 kev. *Sov. At. Energy*, 65:930, 1988.

[29] G.V. Muradyan, M.A. Voskanyan, and L.P. Yastrebova. Measurement of neutron capture and fission cross sections of 236u. *Atomic Energy*, 110(2):115–122, 2011.

[30] Kenneth S. Krane. *Introductory Nuclear Physics.* John Wiley & Sons, NJ, USA, 1988.

[31] Frank Gunsing. *Neutron Resonance Spectroscopy.* CEA/Saclay, DSM/DAPNI-A/SPhN, 2005.

[32] N. Bohr and J. A. Wheeler. The mechanism of nuclear fission. *Phy. Rev.*, 56:426–450, 1939.

[33] L. Eisenbud E. P. Wigner. Higher angular momenta and long range interactions in resonance reactions. *Phy. Rev.*, 72:29–41, 1947.

[34] R. G. Thomas A. M. Lane. R-matrix theory of nuclear reactions. *Rev. Mod. Phys.*, 30:257–353, 1958.

[35] F. H. Frohner. *Evaluation and Analysis of Nuclear Resonance Data*, JEFF Report 18 edition, 2000.

[36] G. Breit and E. Wigner. Capture of slow neutrons. *Phys. Rev.*, 49:519–531, 1936.

[37] J.E. Lynn and E.R. Rae. The analysis of neutron spectrometer resonance data. *J. Nuclear Energy*, 4:418–444, 1957.

[38] Oak Ridge National Laboratory (ORNL). `http://www.ornl.gov/`. [Online; accessed Feb-2015].

[39] N. M. Larson. *UPDATED USERS' GUIDE FOR SAMMY: MULTILEVEL R-MATRIX FITS TO NEUTRON DATA USING BAYES' EQUATIONS.* ORNL, 2008.

[40] C. Rubbia *et al.* A high resolution spallation driven facility at the CERN-PS to measure neutron cross sections in the interval from 1 eV to 250 MeV: A relative performance assessment. Tech. Rep. CERN/LHC/98-02, CERN, 1998.

[41] CERN. CERN Hadron LINACS. `http://linac2.home.cern.ch/linac2/sources/source.htm`, 2008. [Online; accessed 02-06-2014].

[42] C. Guerrero *et al.* Performance of the neutron time-of-flight facility n_TOF at CERN. *Eur. Phys. J A*, 49:27, 2013.

[43] S. Marrone *et al.* A low background neutron flux monitor for the n_TOF facility at CERN. *Nucl. Instr. Meth. A*, 517:389–398, 2004.

[44] IAEA. Neutron cross-section standards, 2006. `https://www-nds.iaea.org/standards/`. [Online; accessed Feb-2015].

[45] C. Paradela *et al.* Neutron-induced fission cross section of ^{234}u and ^{237}np measured at the cern neutron time-of-flight (n_tof) facility. *Phys. Rev. C*, 82:034601, 2010.

[46] J.P. Robert Y. Giomataris, Ph. Rebourgeard and G. Charpak. Micromegas: a high-granularity position-sensitive gaseous detector for high particle-flux environments. *Nucl. Instr. Meth. A*, 376:29–35, 1996.

[47] S. Andriamonje. A transparent detector for n_tof neutron beam monitoring. *J. Korean Phys. Soc.*, 59:1597, 2011.

[48] F. Belloni *et al.* Neutron beam imaging with an XY-micromegas detector at n_TOF at CERN. *Phys. Scr.*, 2012:014004, 2012.

[49] FLUKA. Monte carlo simulation code. `http://www.fluka.org/fluka.php`. [Online; accessed Dec-2014].

[50] M Barbagallo *et al.* High-accuracy determination of the neutron flux at n_TOF. *Eur. Phy. J A*, 49:156, 2013.

[51] G. Lorusso *et al.* Time–energy relation of the n_TOF neutron beam: energy standards revisited. *Nucl. Instr. and Meth. A*, 532:622–630, 2004.

[52] C. Guerrero *et al.* The n_TOF Total Absorption Calorimeter for neutron capture measurements at CERN. *Nucl. Instr. and Meth. A*, 608:424–423, 2009.

[53] A. Borella *et al.* The use of C_6D_6 detectors for neutron induced capture cross-section measurements in the resonance region. *Nucl. Instr. and Meth. A*, 577:626–640, 2007.

[54] E. Mendoza *et al.* Improved neutron capture cross section measurements with the n_tof total absorption calorimeter. *J. Korean Phys. Soc.*, 59:1813–1816, 2011.

[55] U Abbondanno *et al.* The data acquisition system of the neutron time-of-flight facility n_TOF at CERN. *Nucl. Instr. and Meth. A*, 538:692–702, 2005.

[56] CASTOR. CERN Advanced STORage manager. `http://castor.web.cern.ch/`. [Online; accessed Dec-2014].

[57] CERN. ROOT Data Analysis Framework. `https://root.cern.ch/drupal/`. [Online; accessed Oct-2014].

[58] IRMM. Gelina. `https://ec.europa.eu/jrc/en/institutes/irmm`, 2015. [Online; accessed 17-02-2015].

[59] Massimo Barbagallo. *MEASUREMENT OF THE NEUTRON FLUX AND OF THE CAPTURE CROSS SECTION OF ^{236}U AT N_TOF.* PhD thesis, UNIVERSITA DEGLI STUDI DI BARI, 2013.

[60] C. Massimi *et al.* ^{197}Au(n,γ) cross section in the resonance region. *Phys. Rev. C*, 81:1–22, 2010.

[61] Glenn F. Knoll. *Radiation Detection and Measurement.* John Wiley & Sons, NJ, USA, 2000.

[62] C. Guerrero *et al.* Correction of dead-time and pile-up in a detector array for constant and rapidly varying counting rates. *Nucl. Instr. and Meth. A*, 777:63–69, 2015.

[63] J. Halperin R. L. Macklin and R. R. Winters. Absolute neutron capture yield calibration. *Nucl. Instr. and Meth. A*, 164:213–214, 1979.